

# POLITECNICO DI TORINO

Dipartimento di Ingegneria Meccanica e Aerospaziale  
Corso di Laurea Magistrale in Ingegneria Meccanica



Master's Thesis

## Evaluation of Fluid Motion in an Engine Cylinder during the Intake Stroke

**Supervisor:**

Prof. Antonio Mittica

**Candidate:**

Gabriele Scapini

October 2018



*“Dipinte in queste rive / Son dell’umana gente / Le magnifiche sorti e  
progressive.”*

*(“These are excellent slopes / For viewing the human soul / With its grand  
destinies and progressive hopes.”)*

*G. Leopardi, La ginestra, vv. 49-51, 1836*



## **Evaluation of Fluid Motion in an Engine Cylinder during the Intake Stroke**

Gabriele Scapini  
S241664

Politecnico di Torino  
Dipartimento di Ingegneria Meccanica e Aerospaziale  
Turin, Italy

### **Abstract:**

The performances of a new Scania swirl-generating inlet port geometry have been evaluated by means of Time-Resolved Stereo PIV in a water-analogue engine setup mimicking the intake stroke. Two configurations have been inspected: a fixed valve lift case and a more realistic situation where the valves move according to a typical lift profile. A three-dimensional reconstruction of the mean flow has been made from a number of different measured vertical planes intersecting in the cylinder axis. A coherent swirling pattern develops in the three-dimensional flow, where the azimuthal component is predominant over the vertical and radial one. The organization of such large-scale flow structure increases with time during the stroke and with the distance from the cylinder deck. The influence of the valve motion on the swirling magnitude has been found to be negligible, whereas it affects significantly turbulence levels and the tumbling pattern. Phase Invariant POD has been used to detect major cyclic variations in planar data: unusual cyclic variability has been found in some of the planes. Finally, PIV data have been compared with RANS CFD results. A good agreement has been found in planar (radial and vertical) data, whereas RANS simulations seem to underestimate significantly the magnitude of the azimuthal component and therefore the swirl intensity.

### **Descriptors:**

In-cylinder flow, Intake stroke, Water-analogue engine, RANS, Swirl, Phase-invariant POD



# Preface

The current Master thesis work was performed as the final project of a Master Degree in Mechanical Engineering at Politecnico di Torino during an exchange period at KTH Royal Institute of Technology in Stockholm, Sweden. This work was carried out between February and July 2018 as a result of the cooperation of KTH Mechanics and the Department of Engine Development, Gas Exchange Performance (NMGP) at Scania CV AB in Södertälje, Sweden.

October 2018, Turin  
*Gabriele Scapini*



## Acknowledgments

First, I would like to express my gratitude to the supervisors of this project, Henrik Alfredsson at KTH Mechanics and Björn Lindgren of the NMGP group at Scania. Thank you for supporting me with precious advice and helping me out whenever I had some doubts. I have learned a lot thanks to them and this thesis work.

I would also like to thank Athanasia Kalpakli Vester from KTH Mechanics for having introduced me to the experimental setup and database. Thank you for being available and patient to answer to all the questions I had.

I am also thankful to Martin Söder from Scania for the simulations he carried out and the RANS data he provided. I would like to express my gratitude to Antonio Segalini from KTH Mechanics for the useful discussions we had, and Antonio Mittica from Politecnico di Torino, my thesis supervisor at the home university.

Finally, I would like to say thank you to all the people at KTH Mechanics and Scania NMGP for the friendly work environment. It has been a pleasure to work with you!



# Contents

<b>Abstract</b>	iv
<b>Preface</b>	vi
<b>Acknowledgments</b>	viii
<b>Nomenclature</b>	xiv
<b>Chapter 1. Introduction</b>	1
1.1. An insight into heavy-duty Diesel engines development	1
1.2. Towards the understanding of in-cylinder flows	3
1.3. Thesis objectives and layout	5
<b>Chapter 2. Theoretical background</b>	8
2.1. The four-stroke Diesel engine	8
2.1.1. Strokes	9
2.1.2. The ideal Diesel thermodynamic cycle	10
2.1.3. Real operating conditions	12
2.1.4. Combustion and emissions	13
2.2. In-cylinder flows	14
2.2.1. Navier-Stokes equations	15
2.2.2. Incompressible flows	16
2.2.3. Turbulence	17
2.2.4. Reynolds decomposition and RANS	19
2.2.5. Large-scale flow structures	20
<b>Chapter 3. Experimental and numerical methods for the inspection of in-cylinder flows</b>	24
3.1. Particle Image Velocimetry	24
3.1.1. PIV Working principle	25
3.1.2. Seeding particles	25

3.1.3.	Pulsed light source and optics	26
3.1.4.	Camera and calibration	27
3.1.5.	Correlation algorithms	28
3.1.6.	Stereoscopic Particle Image Velocimetry	30
3.1.7.	Recently developed PIV techniques	32
3.2.	Other experimental techniques	33
3.2.1.	Laser Doppler Velocimetry	33
3.2.2.	Particle Tracking Velocimetry	34
3.2.3.	Magnetic Resonance Velocimetry	34
3.3.	Numerical methods	35
3.3.1.	Direct Numerical Simulation (DNS)	36
3.3.2.	Large Eddy Simulation (LES)	37
3.3.3.	Reynolds Averaged Navier-Stokes (RANS)	38
<b>Chapter 4.</b>	<b>Previous studies</b>	<b>42</b>
4.1.	Introduction	42
4.2.	Planar PIV studies	43
4.3.	Recent PIV implementations	44
4.4.	The water-analogue engine	46
4.5.	POD applications	47
4.6.	Numerical studies	48
4.7.	Other experimental studies	49
4.8.	Conclusion	51
<b>Chapter 5.</b>	<b>Experimental setup and data processing</b>	<b>53</b>
5.1.	Experimental setup	53
5.1.1.	The water-analogue engine setup	54
5.1.2.	PIV system and measurements plan	56
5.2.	PIV post-processing	58
5.2.1.	Images processing	58
5.2.2.	Data format and frames of reference	59
5.3.	Evaluation techniques	60
5.3.1.	Proper Orthogonal Decomposition (POD)	61
5.3.2.	Three-dimensional reconstruction	64
5.3.3.	Vortex Tracking	66
<b>Chapter 6.</b>	<b>Results and discussion</b>	<b>69</b>
6.1.	Intake flow overview: planar data	69

6.1.1. Averaged velocity fields	69
6.1.2. Instantaneous velocity fields	75
6.2. Cycle-to-cycle variations: a POD analysis	77
6.2.1. Cyclic variability in the $0^\circ$ plane	77
6.2.2. Cyclic variability in the $135^\circ$ plane	81
6.2.3. Common features and remarks	84
6.3. Intake flow overview: three-dimensional data	85
6.3.1. Averaged velocity fields	85
6.3.2. Turbulent kinetic energy	87
6.3.3. Kinetic energy	90
6.4. A detailed evaluation of the swirling motion	92
6.4.1. Swirl and Tumble numbers	92
6.4.2. Planar swirl analysis	95
6.5. Comparison of PIV measurements with RANS results	97
6.5.1. Planar velocity fields	98
6.5.2. Three-dimensional velocity fields	101
6.5.3. Swirl and tumble parameters	103
<b>Chapter 7. Conclusion and future work</b>	<b>108</b>
7.1. Summary	108
7.2. Outlook on future work	108
<b>Appendix A. SPIV validation using the continuity equation</b>	<b>111</b>
<b>References</b>	<b>114</b>



# Nomenclature

## Tensor and vector notation

Einstein notation for tensors is generally used throughout this report. However, normal vector and matrix notation is utilized in subsections 5.3.1 and 5.3.3.

## Abbreviations

2D	Two-Dimensional
2D2C	Two-Dimensional Two-Component
2D3C	Two-Dimensional Three-Component
3D	Three-Dimensional
3D3C	Three-Dimensional Three-Component
BDC	Bottom Dead Center
CCD	Charged-Coupled Device
CFD	Computational Fluid Dynamics
CI	Compression Ignition
CMOS	Complementary Metal-Oxide Semiconductor
CUDA	Compute Unified Device Architecture
DI	Direct Injection
DISI	Direct Injection Spark Ignition
DNS	Direct Numerical Simulation
DOC	Diesel Oxidation Catalyst
DPF	Diesel Particulate Filter
EGR	Exhaust Gas Recirculation
EPA	U.S. Environmental Protection Agency
FAME	Fatty Acid Methyl Ester
HPIV	Holographic Particle Image Velocimetry
IBVP	Initial Boundary Value Problem
KE	Kinetic Energy
LDV	Laser Doppler Velocimetry
LES	Large Eddy Simulation
MPFI	Multi-Point Fuel Injection
MRV	Magnetic Resonance Velocimetry
Nd:YAG	Neodymium-doped Yttrium Aluminum Garnet
Nd:YLF	Neodymium-doped Yttrium Lithium Fluoride
NO <sub>x</sub>	Oxides of Nitrogen

PIV	Particle Image Velocimetry
PM	Particulate Matter
POD	Proper Orthogonal Decomposition
PTV	Particle Tracking Velocimetry
RANS	Reynolds Averaged Navier-Stokes
RF	Radio Frequency
SCR	Selective Catalyst Reduction
SGS	Sub-Grid Scales
SI	Spark Ignition
SPIV	Stereoscopic Particle Image Velocimetry
TDC	Top Dead Center
TKE	Turbulent Kinetic Energy
TPIV	Tomographic Particle Image Velocimetry
TRPIV	Time-Resolved Particle Image Velocimetry



## CHAPTER 1

# Introduction

### 1.1. An insight into heavy-duty Diesel engines development

Since the introduction of the first tight emission standards during 1990s, developments in the automotive field have been driven by the necessity of reducing pollutants production while maintaining the fuel consumption as low as possible. Among all the categories of vehicles involved, heavy-duty trucks have been targeted with the strictest limitations. In fact, heavy-duty Diesel engines are designed to work in a quasi steady-state regime due to their transport applications, making it easier to keep both emissions and efficiency under control. Nevertheless, with the emissions standards getting stricter throughout the years (Fig. 1.1), truck manufacturers have had to come up with technical solutions of increased complexity to stay within the imposed limits, setting new standards for the development of modern low emissions, high efficiency Diesel engines.

According to both the U.S. Environmental Protection Agency (EPA) standards and the European Euro-x norms, these emissions limits regard mostly the production of Particulate Matter (PM) and oxides of nitrogen (nitric oxide, NO, and nitrogen dioxide, NO<sub>2</sub>, collectively known as NO<sub>x</sub>). While an increased generation of particulate matter is caused by an incomplete combustion of the hydrocarbon fuel, the reduction of this pollutant is achieved by a complete combustion and by high-temperature oxidation. NO<sub>x</sub>, instead, are produced in the high-temperature zones inside the combustion chamber. These differences in the production mechanism make it hard to reduce simultaneously both PM and oxides of nitrogen, resulting in the so-called soot-NO<sub>x</sub> trade-off. Moreover, the overall engine efficiency as well as the economic aspect are limiting constraints to take into account when evaluating new strategies to decrease pollutants production.

In this sense, several solutions and approaches have been pursued over the last 20 years for application to heavy-duty Diesel engines. Different gas-exhaust after-treatment systems have been implemented, such as the Exhaust Gas Recirculation (EGR) system, which allows the recirculation of exhaust gases in the intake duct in order to reduce combustion peak temperatures and thus NO<sub>x</sub> production, or the Diesel Oxidation Catalyst (DOC) system, which employs a catalyst to promote the oxidation of unburnt hydrocarbons into harmless products. Similarly, the Selective Catalyst Reduction (SCR) system

uses a catalyst and a reductant to convert oxides of nitrogen into molecular nitrogen. The Diesel Particulate Filter (DPF), instead, is employed to remove particulate matter from exhaust gases.

While the implementation of these technical solutions often turned out to have a negative effect on engine efficiency (National Research Council 2008), another approach has been followed by heavy-duty truck manufacturers to improve the performances of their Diesel power plants. The purpose of this approach is to optimize the combustion process in order to control and reduce emissions and to increase the overall efficiency. This aim of optimization led to the need for achieving a deeper understanding of the combustion itself and a better comprehension of the phenomena that affect the combustion as well as the way they influence such process.

The study of combustion phenomena from a chemical and physical point of view resulted, among other things, in the introduction of new alternative fuels. As a consequence, over the last decades heavy-duty Diesel engine powered by biodiesel fuels such as Fatty Acid Methyl Ester (FAME), or ethanol-based fuels like ED95 have been developed by truck manufacturers. On the other hand, the industry-oriented research in fluid dynamics has focused on the study of the flow in the cylinder of internal combustion engines before ignition and combustion. In fact, the development and the features of coherent, large-scale structures in the flow velocity field are known to affect the combustion process, and thus the overall efficiency (Heywood 1987). Although full understanding of such effects and the underlying mechanisms has not been achieved yet, the results obtained in this field have led to the development and the design of cylinder and intake port geometries optimized from a flow-based point of view.

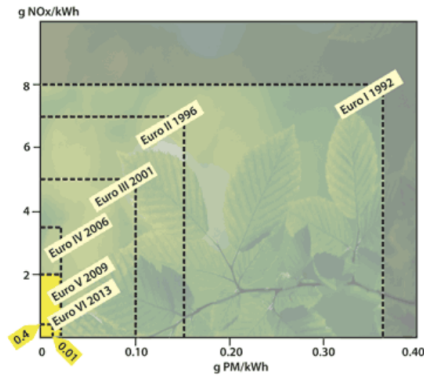


FIGURE 1.1. Evolution of European emission standards, one of the main driving factors for heavy-duty Diesel engines development. Reproduced from Ågren (2009).

## 1.2. Towards the understanding of in-cylinder flows

As mentioned in the previous paragraph, the features of the in-cylinder air flow during intake and compression are acknowledged to strongly affect the combustion quality since the early studies in this research field. In particular, “*The combustion process in Diesel engines depends mainly on the spray atomisation and its interaction with the air flow inside the cylinder. The knowledge of the bulk motion and turbulence inside cylinder is of great importance for the improvement of combustion in DI Diesel engines, and the subsequent reduction of pollutant emissions.*” (Payri *et al.* 1996). This acknowledgement, as well as the industry’s interest in the reduction of pollutants production, has increased the involvement of the research community in the study of in-cylinder flows. In fact, an increasing number of studies based on different approaches, setups and objectives have been published in the last decades.

Two main approaches have been pursued by researchers to inspect in-cylinder flows: experimental measurements and numerical simulations. The former has characterized this research field since the early days, when the employment of single point measurement techniques, such as Laser Doppler Velocimetry (LDV), allowed for the study of turbulence and flow parameters. Technological development has then made it possible to inspect entire two-dimensional velocity fields with the introduction of Particle Image Velocimetry (PIV), which has become the standard for the study of in-cylinder flows. Recently, new measurement techniques able to obtain three-dimensional instantaneous velocity fields, like Tomographic Particle Image Velocimetry (TPIV), Holographic Particle Image Velocimetry (HPIV) or Magnetic Resonance Velocimetry (MRV) made their appearance, although their reliability and effectiveness are yet to be fully demonstrated.

On the other hand, the study of in-cylinder flows by means of numerical simulations is more recent. The application of Computational Fluid Dynamics (CFD) for the analysis of such three-dimensional flows had been impeded in the past by their strong turbulent nature, but the increasing available computational power has nowadays paced the development of accurate numerical methods. All CFD methods solve the governing equations for the fluid motion, *i.e.* the Navier-Stokes equations. Due to their non-linearity and the large ranges of turbulence time and length scales involved, in most of the cases a complete solution of these equations is prohibitive from a computational point of view, and therefore modeling is necessary. Simplified approaches based on turbulence modeling are the most commonly employed for the in-cylinder flow research: while Reynolds Averaged Navier-Stokes (RANS) methods are accurate only for certain types of flow, Large Eddy Simulation (LES) methods provide better results when compared to experimental data, but they also require higher computational power since they only model the smaller scales. Hybrid

RANS-LES solvers have been implemented as well. Direct Numerical Simulations (DNS), instead, aim to compute a complete solution of the Navier-Stokes equations, but their narrow range of applications and the huge computational time required have limited their use for the study of in-cylinder flows.

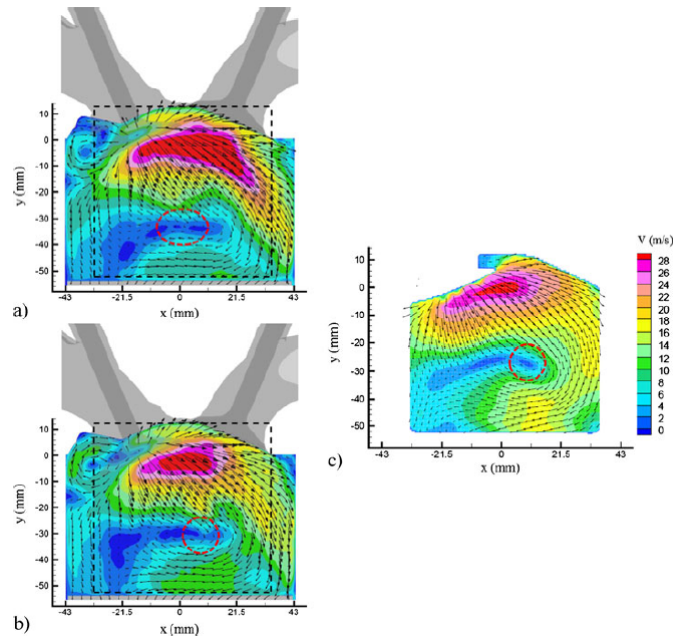


FIGURE 1.2. Comparison of the phase averaged flow field of an engine cross section at the middle of the intake stroke. While (a) and (b) are LES results obtained with a coarse and refined mesh respectively, (c) has been measured by means of PIV. Reproduced from Baumann *et al.* (2014).

Despite their common employment in the industry and in the research field, both the experimental and the numerical approach still have their limitations. Experimental studies of the flow require the implementation of special optical accessible setups as well as the use of expensive instrumentation and, in the most part of the cases, they allow only for a two-dimensional, low-frequency inspection of the flow. Numerical methods, instead, provide a full three-dimensional, time-resolved visualization of the flow, but they suffer from inaccuracies and lack of reliability in the prediction of complex cases as in-cylinder flows. To overcome such weaknesses, numerical methods of increasing

required computational power are to be employed, and this is not always possible. Moreover, numerical results should always be validated in comparison with experimental data.

However, the biggest challenge towards the full understanding of in-cylinder flows lies in the difficulty of capturing in details the turbulent phenomena occurring in the flow. In fact, turbulence is considered one of the most difficult physical phenomenon to study, explain and describe. It is famous, in this sense, the quotation from the English applied mathematician Horace Lamb, who, in 1932, addressing the British Association for the Advancement of Science, reportedly said *“I am an old man now, and when I die and go to heaven there are two matters on which I hope for enlightenment. One is quantum electrodynamics, and the other is turbulent motion of fluids. And about the former I am rather optimistic”* (Mullin 1989). The wide spectra of turbulent length and time scales to inspect, in fact, make it almost impossible to fully describe complex flows even with nowadays technology. Only big improvements in resolutions and frequencies achievable by experimental methods and a marked increase in available computational power will help obtaining a deeper understanding in this field.

### 1.3. Thesis objectives and layout

The main objective of this thesis work is the evaluation of a large experimental database of in-cylinder PIV measurements of the intake stroke. The measurement campaign, which is not an active part of the thesis, was carried out at the Department of Mechanics at KTH-Royal Institute of Technology in Stockholm, Sweden with the purpose of testing the performances of a new Scania swirl-generating intake port. The analysis is mostly focused on the features of large-scale structures generated during the intake in the three-dimensional, time-resolved flow field, with a particular attention paid to the development of an organized swirl motion, and it has been carried out using MATLAB®. Furthermore, a comparison of the PIV measurements with the results obtained from a RANS simulation performed at Scania is also part of this work.

The present report is structured as follows: after the brief introduction to the research topic presented in the current chapter 1, chapter 2 provides the theoretical background about Diesel engines, fluid mechanics and in-cylinder flows necessary for the understanding of this study. Chapter 3, instead, describes the different aspects of the PIV method employed in the measurement campaign and reviews the main features of the other experimental techniques available. Eventually a short insight into numerical methods is presented. A literature review about previous studies in the in-cylinder flow research field is contained in chapter 4, while chapter 5 goes through the experimental setup used for the PIV measurements and the procedure followed to post-process, import and evaluate PIV raw data. Finally, the results of this study are presented

and discussed in chapter 6, while chapter 7 concludes this report providing a summary and an outlook on future work.



## CHAPTER 2

### Theoretical background

In the present chapter a brief introduction to basic aspects regarding Diesel engines is given. This short summary goes through general notions of internal combustion engines, thermodynamics and fluid mechanics to provide an useful background for the comprehension of this thesis work.

#### 2.1. The four-stroke Diesel engine

Patented in 1892 by Rudolf Diesel, the Diesel engine has found broad application in different fields since its introduction. Because of their lower fuel consumption and high reliability in comparison to Otto engines, Diesel engines are nowadays widely employed in marine transport, passenger cars, power generation and heavy-duty truck propulsion. Even though Diesel power plants present different features depending on the specific application, *e.g.* different numbers, sizes and configurations of cylinders, these engines can be classified into two major categories: two-stroke and four-stroke Diesel engines. Since the heavy-duty truck market is dominated by vehicles powered by four-stroke Diesel propulsors and the engines manufactured at Scania belong to this category, from now on this report will only focus on this type of engine.



FIGURE 2.1. A modern Scania Euro 6 heavy-duty four-stroke Diesel engine.

From a technical point of view, a four-stroke Diesel engine is a reciprocating internal combustion engine, since it converts the chemical energy contained in the fuel, released by burning or oxidizing it inside the engine itself, into mechanical energy. This mechanical energy is then transferred from the reciprocating motion of the piston to the drive shaft through a connecting rod-crank mechanism (Heywood 1988). The main difference from an Otto engine is the way the combustion is ignited: in Diesel engines the ignition of the fuel is caused by the elevated temperature of the air in the cylinder due to mechanical compression, whereas in Otto engines the air-fuel mixture is ignited by a spark from a spark plug. For this reason they are also called Compression Ignition (CI) and Spark Ignition (SI) engines respectively. The process of converting chemical energy into mechanical energy is accomplished through the realization of a thermodynamic cycle, the so-called Diesel cycle, which is described in subsection 2.1.2 and subsection 2.1.3. Differently from a two-stroke engine, a four-stroke engine requires two crankshaft revolutions, or, as suggested by the name, four piston strokes to complete one thermodynamic cycle. The features and the purposes of each one of these strokes are described in the next subsection, considering a simplified two-valve engine configuration.

### 2.1.1. *Strokes*

As mentioned in the previous paragraph, in a four-stroke engine, be it a SI or a CI engine, *“each cylinder requires four strokes of its piston—two revolutions of the crankshaft—to complete the sequence of events which produces one power stroke”* (Heywood 1988).

The cycle begins with the intake (or induction) stroke. During this stroke the intake valve is open and the downward motion of the piston from its highest possible position, called Top Dead Center (TDC), to its lowest possible position, known as Bottom Dead Center (BDC), sucks air into the cylinder. In naturally aspirated engines the inducted air is at atmospheric pressure, whereas in supercharged and turbocharged engines this air is pre-compressed by a compressor. During the intake stroke the exhaust valve is closed.

The compression stroke starts with the piston at BDC: both the valves are closed, and the upwards motion of the piston to the TDC compresses the air contained in the cylinder to a small fraction (namely the inverse of the compression ratio) of its initial volume. In Diesel engines, the temperature and the pressure of the air inside the cylinder at the end of this stroke are high enough to provoke the spontaneous ignition of the fuel once the injection takes place. The rapid development of diffusive combustion leads then to a rapid rise in cylinder pressure and temperature.

With both the valves still closed, high-pressure, high-temperature in-cylinder gases push the piston downwards during the power (or expansion) stroke. As the piston approaches BDC, the exhaust valve opens to start the exhaust process, and the pressure drops to a value close to the exhaust manifold pressure. During the power stroke the work done on the piston by the expanding gases is about five times the work the piston had to do in the compression stroke.

Finally, during the exhaust stroke the burnt gases exit the cylinder due to the remaining pressure difference and the sweeping action of the piston as it moves upwards to the TDC. Towards the end of the stroke, the inlet valve opens. After the piston reaches the TDC, the exhaust valve closes and the cycle starts again.

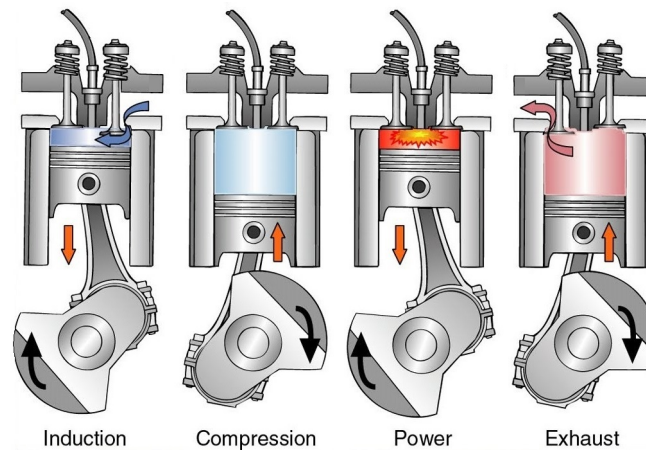


FIGURE 2.2. A schematic representation of the four-stroke Diesel engine cycle. Adapted from Kumar (2016).

### 2.1.2. *The ideal Diesel thermodynamic cycle*

During the operation of an engine the working fluid undergoes a sequence of cyclic transformations whose purpose is the conversion of thermal energy released by combustion into work. Whereas the actual Diesel engine cycle performed is complex and influenced by several different factors as treated in subsection 2.1.3, considering an idealized thermodynamic cycle is useful to comprehend the main features of the engine operation and to estimate its efficiency. The ideal Diesel cycle, as can be seen in Fig. 2.3 , follows four successive thermodynamic transformations: an isentropic compression of the fluid (1-2), a reversible constant pressure heating (2-3), an isentropic expansion (3-4) and a reversible constant volume cooling (4-1).

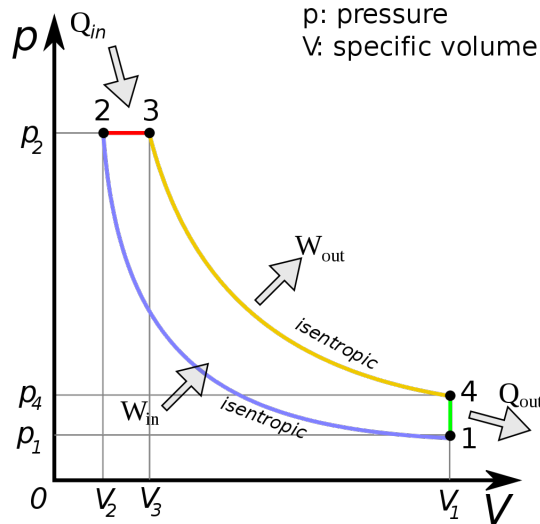


FIGURE 2.3. The ideal Diesel cycle in the p-V diagram. Reproduced from Wikimedia Commons (2015).

Being an idealized thermodynamic cycle, some major simplifications are assumed. Firstly, all the transformations are reversible, with no irreversible entropy production. Secondly, the system is closed, and consequently the mass is conserved during the whole cycle and gas exchange processes (intake and exhaust) are not taken into consideration. Thirdly, the working fluid is modeled as an ideal gas and combustion is treated as an heat absorption from an external reservoir. Nevertheless, the analysis of this ideal Diesel cycle is convenient for efficiency estimates and comparisons with different cycles, *e.g.* the ideal Otto cycle. Before deriving the cycle efficiency, it is useful to introduce three parameters: the compression ratio, the cut-off ratio and the ratio of specific heats. The compression ratio is a characteristic geometrical parameter of an engine. It represents the ratio between the cylinder volume at BDC and the cylinder volume at TDC:

$$r_c = \frac{V_1}{V_2} \quad (2.1)$$

The cut-off ratio, instead, is the ratio between the cylinder volume at the start of the combustion and the cylinder volume at the end of the combustion:

$$\alpha = \frac{V_3}{V_2} \quad (2.2)$$

Finally, the ratio of specific heats is the ratio between the specific heat at constant pressure and the specific heat at constant volume and, since in this

case air is modeled as a diatomic ideal gas, its value is 1.4:

$$\gamma = \frac{c_p}{c_v} = 1.4 \quad (2.3)$$

Given these parameters, the thermal efficiency of the ideal Diesel cycle can be written as:

$$\eta_{th,Diesel} = \frac{W_{out} - W_{in}}{Q_{in}} = 1 - \frac{1}{r_c^{\gamma-1}} \left( \frac{\alpha^\gamma - 1}{\gamma(\alpha - 1)} \right) \quad (2.4)$$

Although it represents a superior limit for the actual Diesel engine thermal efficiency due to all the irreversibilities and losses that have not been taken into consideration, the ideal thermal efficiency highlights the crucial importance of the compression ratio and its influence on the engine performances. Moreover, it is interesting to compare the ideal Diesel cycle efficiency with the ideal Otto cycle efficiency, which is:

$$\eta_{th,Otto} = \frac{W_{out} - W_{in}}{Q_{in}} = 1 - \frac{1}{r_c^{\gamma-1}} \quad (2.5)$$

Since the parenthesis term in Eq. 2.4 is always greater than one, for a given compression ratio Otto cycle efficiency is higher than Diesel efficiency. However, Diesel engines operate with higher compression ratios than Otto engines, leading to an higher efficiency, or a lower fuel consumption. In fact, while in compression ignition engines a higher compression ratio, and thus a higher pressure and temperature at the end of the compression stroke, is required to achieve self-ignition, in spark ignition engines the compression ratio is limited in order to avoid self-ignition with its damaging effect on efficiency.

### 2.1.3. *Real operating conditions*

The actual Diesel working cycle is significantly more complex than the ideal one. In fact, most of the simplifications assumed for the ideal thermodynamic cycle are too limiting to describe properly the Diesel engine operation and to predict accurately its fuel consumption and power output.

First of all, no real transformation is reversible, and thus the production of irreversible entropy decreases the work achievable. Moreover, both the specific heat ratio and the specific gas constant vary throughout the cycle. The actual system is open: the intake and exhaust processes and the work required to complete them have to be taken into account, as well as gas leakages through crevices such the region between the piston, piston rings and cylinder wall. The heat is provided to the system through combustion, which in real cases is neither complete nor instantaneous, and heat exchange from the burning mixture to the cylinder walls causes a lower pressure at the end of combustion. Also the timing of valves opening and closing affects the real cycle: for example, the advance in the opening of the exhaust valves at the end of expansion reduces the work achievable.

All these phenomena, along with mechanical losses, power absorbed by accessory components, and an incomplete filling of the cylinder, decrease the overall efficiency and reduce the power output of a real Diesel engine to a fraction of the output predicted with the ideal thermodynamic cycle.

#### 2.1.4. *Combustion and emissions*

The study of the combustion process is of vital importance for understanding the mechanism of pollutants generation. A proper optimization of this process leads to a decrease in emissions production as well as an increase in the efficiency. One way to pursue this optimization is by studying the influence of large-scale, in-cylinder flow structures developed during intake and compression on the combustion process itself.

Diesel combustion is a high-temperature exothermic chemical reaction between a hydrocarbon-based fuel and the atmospheric oxygen contained in air, which acts as an oxidant. The products of this reaction are water, diatomic nitrogen and carbon dioxide, and heat is released in the process. Depending on the ratio between the mass of air and the mass of fuel present in the cylinder, combustion can be lean, if there is an excess of air compared to the quantity required by reaction stoichiometry, rich, if the fuel exceeds the stoichiometric amount, or stoichiometric. As already mentioned, combustion in Diesel engines is self-ignited by the high temperature reached in the cylinder at the end of compression. In this sense, Diesel fuels should have good autoignition properties to achieve a good ignition timing: the Cetane number is a parameter used to quantify such properties.

Once the fuel injection starts and ignition takes place, a diffusive combustion takes over in Diesel engines, and it is controlled by the high-pressure injection of the remaining fuel and by the mixing process of fuel and air. This mixing process can be improved and the combustion rate can be increased to avoid an incomplete combustion due to the short time interval available before the start of the power stroke. To do so, the swirling air motion around the cylinder axis induced by the intake port, the squish motion caused by the piston bowl and turbulence are often taken into consideration. Although Diesel combustion is always globally lean, locally the mixture can be rich due to an uneven mixing.

Regarding the production of pollutants caused by the combustion process, the two main targets of emission standards for Diesel engines are particulate matter and nitrogen oxides. Particulate matter is generated in the incomplete combustion caused by fuel excess where the mixture is locally rich.  $\text{NO}_x$ , instead, are produced by the oxidation of nitrogen occurring at higher temperatures in zones with a locally stoichiometric combustion. In the same zones, PM oxidation occurs, leading to a reduction of the emissions of this pollutant. This coexistence of opposite mechanism at the same conditions makes it hard

to reduce both these pollutants, forcing a trade-off in the optimization process. Carbon dioxide emissions are also a problem for Diesel engines, since this pollutant is a product of the combustion reaction and thus its production can not be avoided. Strategies to reduce  $\text{CO}_2$  emissions from heavy-duty trucks are then focused mostly on the operation of the vehicle, targeting the type of fuel used, the driving style, vehicle dimensions and infrastructure management and maintenance. The pursuit of such strategies will soon become a standard for truck manufacturers, due to the introduction of the first European  $\text{CO}_2$  standards for heavy-duty engine in May 2018 (ACEA 2018). Minor issues for Diesel engines are the production of carbon monoxide ( $\text{CO}$ ), caused by rich combustion and high-temperature dissociation of  $\text{CO}_2$ , and the presence of unburnt hydrocarbons. These two pollutants are typically oxidized by the excess of air before the exhaust valve opens.

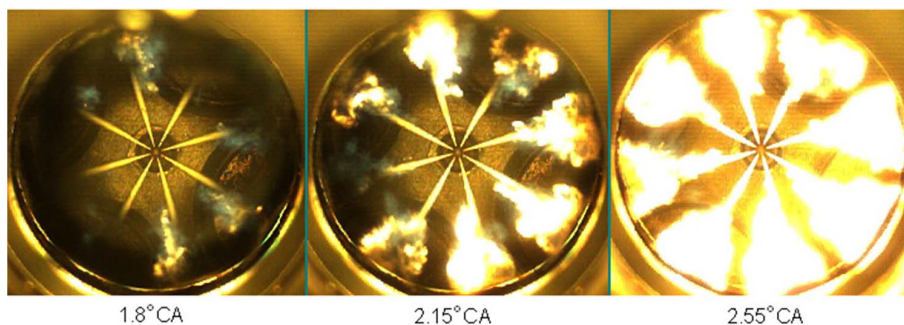


FIGURE 2.4. Combustion in an optically accessible Diesel engine. The fuel jet spray and the development of a diffusion flame can be seen. Reproduced from Cronhjort (2017).

## 2.2. In-cylinder flows

Fluid flow inside the cylinder is a rather complex case of an unsteady and turbulent flow. As any other fluid flow, it is described by the Navier-Stokes equations, which are balance equations derived from applying conservation laws to fluid motion. The strong turbulent nature of in-cylinder flows, along with their unsteadiness, makes it hard to numerically solve these equation and predict the behaviour of the flow. Nevertheless, these flows have common features such as the development of large-scale, coherent structures that can be used to create a simplified model of the fluid motion. In fact, these flow structures are easy to describe and their characteristics are important to influence the combustion process efficiency and emissions. A brief review of the Navier-Stokes equations theory, along with an introduction to turbulence and large-scale flow structures, is given within the next subsections.

### 2.2.1. Navier-Stokes equations

The Navier-Stokes equations, together with the continuity and the energy equations, are the governing equations for fluid motion. These governing equations represent respectively the mathematical formulation of momentum, mass and energy conservation laws applied to fluids. A fluid is intended as a continuous substance which deforms when subjected to a shear stress. The complete set of equations for a compressible flow consists of five scalar partial differential equations: one for mass, three for momentum and one for energy conservation. It can be written as:

$$\frac{\partial \rho}{\partial t} + \frac{\partial(\rho u_i)}{\partial x_i} = 0 \quad (2.6)$$

$$\frac{\partial(\rho u_i)}{\partial t} + \frac{\partial(\rho u_i u_j)}{\partial x_j} = -\frac{\partial p}{\partial x_i} + \frac{\partial \tau_{ij}}{\partial x_j} + \rho f_i \quad (2.7)$$

$$\frac{\partial(\rho e_0)}{\partial t} + \frac{\partial(\rho e_0 u_i)}{\partial x_i} + \frac{\partial(\rho u_i)}{\partial x_i} = \frac{\partial(\tau_{ij} u_j)}{\partial x_i} + \rho f_i u_i + \frac{\partial q_i}{\partial x_i} \quad (2.8)$$

where  $\rho$  is the density,  $u_i$  is the velocity vector,  $p$  is the static pressure,  $\tau_{ij}$  is the viscous stress tensor,  $f_i$  represents body accelerations acting on the fluid (*e.g.* gravity or inertial accelerations),  $e_0$  is the total energy defined as  $e_0 = e_I + \frac{1}{2}u^2$ ,  $e_I$  is the internal energy and  $q_i$  is the heat flux.

The number of unknowns in this general set of equations is larger than the number of equations themselves. Therefore, for the closure of the problem it is necessary to define fluid properties, constitutive laws and external acceleration/force fields. The modeling of these properties and relations depends on the fluid taken into consideration, and leads to the derivation of a more specific, closed set of equations.

For the in-cylinder flow case, the fluid can be considered as Newtonian, and thus viscous stresses are proportional to the dynamic viscosity  $\mu$  according to the following relation:

$$\tau_{ij} = \mu \left( \frac{\partial u_i}{\partial x_j} + \frac{\partial u_j}{\partial x_i} - \frac{2}{3} \delta_{ij} \frac{\partial u_k}{\partial x_k} \right) \quad (2.9)$$

In most of the cases, viscosity can not be assumed as constant, and its dependence on the fluid temperature  $T$  is often modeled with Sutherland's law:

$$\mu = \mu_{ref} \left( \frac{T}{T_{ref}} \right)^{3/2} \frac{T_{ref} + T_s}{T + T_s} \quad (2.10)$$

where  $\mu_{ref}$  is the viscosity at the reference temperature  $T_{ref}$  and  $S$  is the Sutherland temperature. Reference values for this parameters can be found, for different gases, in the literature.

Moreover, air can be considered as an ideal gas in a first approximation, and therefore the perfect gas law can be employed as the equation of state to relate its thermodynamic properties as follows:

$$p = \rho RT \quad (2.11)$$

where  $R$  is the specific gas constant.

The Fourier law is then used to describe the heat flux by conduction:

$$q_i = -k \frac{\partial T}{\partial x_i} \quad (2.12)$$

where  $k$  is the thermal conductivity of the continuum.

Finally, an equation for the internal energy of the fluid needs to be added. Assuming a constant heat capacity  $c_v$ , the internal energy of the in-cylinder air can be modeled as:

$$e_I = e_{I,ref} + c_v(T - T_{ref}) \quad (2.13)$$

where  $e_{I,ref}$  is the internal energy of the fluid at the temperature  $T_{ref}$ .

Since in the vast majority of the in-cylinder flows the action of external forces like gravity can be neglected, these specific relations introduced allow for the closure of the problem. The general set of equations, in fact, is now reduced to a set of five equations and five unknowns. By introducing a set of initial and boundary conditions for the unknowns, an Initial Boundary Value Problem (IBVP) is obtained. Different kind of boundary and initial conditions can be defined depending on the case of study. For in-cylinder flows, the no-slip, adiabatic condition is usually applied for cylinder walls, whereas the value of either the pressure or the mass flow is commonly set to define inlet and outlet conditions. The inlet temperature has to be fixed as well. Initial conditions, instead, depend on the initial time instant selected and therefore on the stroke considered.

Despite the closure of the problem and the definition of the IBVP, the analytic solution of this system of equations is possible only in a small range of simplified case, whereas the existence of analytic solutions for the general case has not been proven yet. The only way to solve these equations in the wide range of practical uses of engineering interest is by a numerical approach.

### 2.2.2. Incompressible flows

Although the numerical approach is almost always the only way to deal with Navier-Stokes equations, the numerical solution often turns out to be prohibitive from a computational point of view. In this sense, some simplifications are often assumed to reduce the complexity of such system of equations. For the study of the intake stroke of internal combustion engines, a reasonable simplification is to consider the flow as incompressible ( $\rho = const.$ ) and isothermal ( $T = const.$ ). In this case, taking into consideration the relations introduced

in the previous subsection, the set of governing equations can be written as follows:

$$\frac{\partial u_i}{\partial x_i} = 0 \quad (2.14)$$

$$\frac{\partial u_i}{\partial t} + u_j \frac{\partial u_i}{\partial x_j} = -\frac{1}{\rho} \frac{\partial p}{\partial x_i} + \nu \frac{\partial^2 u_i}{\partial x_j \partial x_j} \quad (2.15)$$

where  $\nu = \frac{\mu}{\rho}$  is the kinematic viscosity.

Even though these simplifications allow for the reduction of the number of equations and unknowns, the main source of computational and physical complexity is not affected by the assumptions made. In fact, the Navier-Stokes equation are non-linear equations in the general case and so remain in almost every real situation. The non-linearity of these equations, expressed in the second term on the left-hand side of Eq. 2.15, is the basis for turbulence and the richness of phenomena in fluid mechanics (Johansson & Wallin 2017).

### 2.2.3. *Turbulence*

Turbulence can be described as a flow regime characterized by chaotic fluctuations of fluid velocity and pressure in time and space. Differently from a laminar flow, in which the fluid moves regularly and smoothly along parallel layers with no disruptions, a turbulent flow features irregular, strongly three-dimensional motion paths and the presence of vortical structures (eddies) along a wide spectrum of length scales. The development of a turbulent flow is often sought in different engineering applications where mixing plays an important role, such as combustion in Diesel engines, due to the high diffusivity typical of this flow regime. Among its other application of engineering interest, turbulence is important since it influences drag. Whereas the friction drag caused by a turbulent boundary layer is higher compared to the laminar case, turbulence is favorable for reducing flow separation and this sometimes results in an overall reduction of the total drag.

A turbulent flow is characterized by the dissipation of kinetic energy (KE) into heat through the so-called energy cascade, where eddies transfer energy to smaller scales for which viscous stresses become increasingly important, and finally viscous dissipation occurs. Therefore, energy must be fed into the large scales from the mean flow or external sources, like heating, to sustain turbulence. Moreover, after a certain number of vortex interactions turbulence forgets its initial conditions and the flow tends towards a self-similar state independent of how turbulence was initiated. While the size of the bigger eddies is limited by the geometry considered, *e.g.* the diameter of a pipe, the smaller length scales are assumed to be independent on geometrical boundaries and to be influenced only by the viscosity  $\nu$  and the viscous dissipation  $\epsilon$ .



FIGURE 2.5. Illustration of eddies of different length scales in a turbulent flow by Leonardo Da Vinci, one of the first scientists to observe and study turbulence.

The aforementioned hypothesis, along with the description of the energy cascade process, was the starting point for the development of the first formal turbulent phenomenology theory, the “K41 theory”. Presented in Kolmogorov (1941), it is based on a statistical approach and manages to describe energy spectra over the different length scales of the flow through dimensional analysis. An important result of this theory is the determination of the smallest scales, called Kolmogorov scales, where viscous dissipation occurs:

$$\eta = (\nu^3/\epsilon)^{1/4} \quad (2.16)$$

$$t_\eta = (\nu/\epsilon)^{1/2} \quad (2.17)$$

$$v_\eta = (\nu\epsilon)^{1/4} \quad (2.18)$$

where  $\eta$  is the length scale, and  $t_\eta$  and  $v_\eta$  are the corresponding time and velocity scale respectively.

Although all these chaotic fluctuations seem to be random and disorganized, turbulent flows are still governed by Navier-Stokes equations. The insurgence of a turbulent flow, in fact, occurs when the quadratic term in the momentum equation takes over. From a physical point of view, this means that the inertial forces become predominant and can not be damped by viscous stresses, leading to the chaotic fluctuations typical of turbulence. Thus, the difference between turbulent and laminar flow can be expressed with a non-dimensional parameter that represents the ratio between inertial forces and viscous forces, known as Reynolds number:

$$Re = \frac{\rho u D}{\mu} = \frac{u D}{\nu} \quad (2.19)$$

where  $u$  and  $D$  are the flow characteristic velocity and length scale respectively. For in-cylinder flows, the diameter of the cylinder and the piston mean

velocity are commonly considered. Indeed, turbulent flows have large Reynolds numbers. Since viscous stresses become important at smaller length scales and dominate the Kolmogorov scales, at this level the Reynolds number is unity:

$$Re = \frac{v_\eta \eta}{\nu} = 1 \quad (2.20)$$

#### 2.2.4. Reynolds decomposition and RANS

Due to the wide range of length and time scales involved and the complexity of the instantaneous fluid motion, the numerical solution of the complete set of governing equations is often prohibitive and useless from an engineering point of view (whereas it finds applications in the research field for the study of turbulence features). A statistical approach, aiming to analyse the development of statistical quantities, such as the mean flow, is preferred for the study of turbulence and the solution of Navier-Stokes equations in most of the engineering applications. This statistical approach is based on the Reynolds decomposition, which splits the pressure and velocity fields into a mean component, denoted by capital letters, and a fluctuating part, denoted with a prime:

$$u_i = U_i + u'_i \quad (2.21)$$

$$p = P + p' \quad (2.22)$$

Two type of averages can be introduced to define the mean component of a field: the ensemble average, *i.e.* the average over a large number of realizations of a flow, and a time average, obtained by integrating the quantity over a certain time range. In the case of unsteady flows with many realizations, such as the unsteady realizations of the in-cylinder flow over a large number of engine cycles, the former is preferred. The ensemble averaged value of a quantity  $q$  over  $N$  realizations of the flow is denoted with  $\langle q \rangle$  and defined as follows:

$$\langle q \rangle = \frac{1}{N} \sum_{n=1}^N q^{(n)} \quad (2.23)$$

By introducing the Reynolds decomposition in the incompressible Navier-Stokes and continuity equations and averaging them, we obtain a set of equations for the mean flow, the Reynolds Averaged Navier-Stokes (RANS) equations:

$$\frac{\partial U_i}{\partial x_i} = 0 \quad (2.24)$$

$$\frac{\partial U_i}{\partial t} + U_j \frac{\partial U_i}{\partial x_j} = -\frac{1}{\rho} \frac{\partial P}{\partial x_i} + \frac{\partial}{\partial x_j} \left( \nu \frac{\partial U_i}{\partial x_j} - \langle u'_i u'_j \rangle \right) \quad (2.25)$$

Eq. 2.25 is referred to as the Reynolds equation, and describe the balance of momentum of the mean field. Nevertheless, due to the nonlinear nature of the original equations, it contains a term derived from instantaneous fields

in the right-hand side,  $\langle u'_i u'_j \rangle$ . This turbulent interaction term plays a role analogous to the viscous stress tensor, and hence is rewritten in order to define the turbulent stress, or Reynolds stress tensor as:

$$R_{ij} = -\rho \langle u'_i u'_j \rangle \quad (2.26)$$

The presence of this symmetric tensor introduces a term which does not depend on mean quantities, and the unknowns outnumber the equations in the RANS system. To obtain equations which contain only the mean velocity and pressure and close the RANS system, the Reynolds stress tensor must be modeled as a function of the mean flow, removing any reference to the fluctuating part. This modeling problem is known as the turbulence closure problem, and different solutions have been presented throughout the years to describe the Reynolds stress tensor, with different results depending on the cases studied.

Also kinetic energy can be split according to the Reynolds decomposition. Due to its non linear definition, the mean kinetic energy of the flow is made up of the sum of the kinetic energy of the mean velocity field  $K^{(M)} = \frac{1}{2} U_i U_i$  and the turbulent kinetic energy (TKE), *i.e.* the mean kinetic energy of the velocity fluctuations  $K = \frac{1}{2} \langle u_i u_i \rangle$ , such that:

$$K^{(tot)} = K^{(M)} + K = \frac{1}{2} U_i U_i + \frac{1}{2} \langle u_i u_i \rangle \quad (2.27)$$

### 2.2.5. Large-scale flow structures

Along with turbulence, the presence of large-scale flow structures within the cylinder walls influences the mixing processes in the diffusive combustion typical of Diesel engines, and therefore affects the burning rates. These structures, known as swirl and tumble, consist in two overall coherent rotation of the flow around the cylinder axis and an horizontal axis respectively, as can be seen in Fig. 2.6. Swirl and tumble motions dissipate slower than turbulence, and hence retain their kinetic energy for a longer time.

In particular, the intensity of the swirling motion around the cylinder axis plays a major role in the development of an efficient combustion process in Diesel engines (whereas in Otto engines tumble is given a greater importance). To achieve a strong swirl in the cylinder, a geometrical optimization of components as the intake port and the cylinder bowl is to be pursued. In fact, swirl is induced during the intake stroke by the fluid flowing through the intake port into the cylinder. Tumble, instead, is created when the strong intake jet flow gets deflected by cylinder walls and the piston during the intake stroke, and it is affected by valves and port configuration. During the following compression strokes, swirl is conserved, while tumble breakdown occurs: the main tumble vortex is transformed in smaller-scales eddies, increasing the level of in-cylinder turbulence and taking part in the energy cascade process.

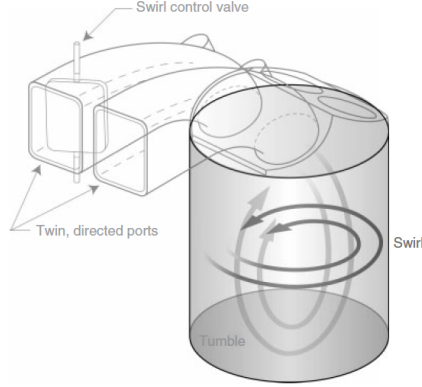


FIGURE 2.6. Visualization of swirl and tumble. Reproduced from Borée & Miles (2014).

The use of relevant parameters to describe these motion patterns is necessary to compare the influence of intake ports on the swirl motion and to evaluate the effect of these large-scale structures on combustion. The simplest way to define such parameters is considering the momentum contained within the cylinder walls and simplify swirl and tumble as solid body-like rotations. In this way, a rotational speed for swirl and tumble can be defined and compared to the rotational speed of the engine, in order to define the Swirl Number  $SN$  and the Tumble Number  $TN$  as:

$$SN = \frac{\Omega_{Swirl}}{\Omega_E} \quad (2.28)$$

$$TN = \frac{\Omega_{Tumble}}{\Omega_E} \quad (2.29)$$

where  $\Omega_E$  is the rotational speed of the engine and, given the stroke  $S$  and the piston mean velocity  $U_p$ , it is computed as:

$$\Omega_E = \frac{2\pi U_p}{S} \quad (2.30)$$

$\Omega_{Swirl}$  and  $\Omega_{Tumble}$ , instead, are the components along the cylinder axis and in the orthogonal plane respectively of  $\Omega_i$ , the characteristic angular velocity of the flow:

$$\Omega_i = I_{ij}^{-1} L_j \quad (2.31)$$

where  $L_i$  is the angular momentum of the flow around the center of gravity, evaluated as:

$$L_i = \iiint_V \epsilon_{ijk} r_j u_k \rho dV \quad (2.32)$$

where  $\epsilon_{ijk}$  is the Levi-Civita symbol,  $r_i$  is the displacement vector and  $u_i$  is the velocity vector.  $I_{ij}^{-1}$  is the inverse of the inertia tensor  $I_{ij}$ , which is defined in

the following way:

$$I_{ij} = \iiint_V (-r_i r_j + \delta_{ij} r_k r_k) \rho dV \quad (2.33)$$

where  $\delta_{ij}$  is the Kronecker delta.

The Swirl Number can intuitively be interpreted as the number of revolutions around the cylinder axis accomplished by a solid body-like rotation with the same momentum and inertia of the flow, per engine revolution. A similar meaning can be given to the Tumble Number, which instead quantifies the number of revolutions around an axis lying in the horizontal plane. However, it has to be noticed how, to compute such parameters, the whole three-dimensional velocity field must be known. This represents the main drawback of the evaluation method presented, since it makes it unemployable with the common two-dimensional experimental techniques. On the other hand, when the three-dimensional velocity fields can be obtained, Swirl and Tumble numbers are useful parameters to quantify the intensity of large-scale flow structures and to compare experimental data with three-dimensional numerical results.



## CHAPTER 3

# Experimental and numerical methods for the inspection of in-cylinder flows

In this chapter, an overview of the available methods to inspect in-cylinder flows is presented. The main focus is on Particle Image Velocimetry, being the technique employed for this study and the most common one for flow visualization. Eventually, other traditional or developing experimental techniques are treated, and a brief insight into numerical methods is provided.

### 3.1. Particle Image Velocimetry

Over the past three decades, Particle Image Velocimetry has gained an increasing interest within the fluid mechanics research community and has become the most common experimental technique to study complex turbulent flows. The key feature for such a spread in both the academic and the industrial research field is its ability to measure instantaneous velocity fields simultaneously at multiple points, with a resolution high enough to compute differential properties of the flow, like strain rate or vorticity. While the first PIV systems developed allowed only for the measurement of two-dimensional, two-component (2D2C) velocity fields, technological development has made it possible to inspect, or at least reconstruct, three-dimensional, three-component (3D3C) velocity fields. Moreover, the recent introduction of Time-Resolved Particle Image Velocimetry (TRPIV) systems has permitted a complete description of the time evolution of entire velocity fields of rapidly-evolving flows.

Although the wide variety of techniques available and their complexity, all the PIV systems are based on a simple idea: the addition of particles or objects to a fluid in order to observe its flow. The way this simple idea is realized, as well as the main PIV features, limitations and variations, is dealt with in the next subsections. However, this section does not mean to be exhaustive and cover all the topics regarding PIV systems: for a detailed review of classical PIV aspects and implementation, the reader is referred to Raffael *et al.* (1998) and Dabiri (2006), whereas an overview of recently developed PIV methods can be found in Westerweel *et al.* (2012) and van Overbrüggen *et al.* (2015).

### 3.1.1. PIV Working principle

PIV is a non-invasive, multi-point optical measurement method for the experimental inspection of complex flows. It is based on a simple, yet effective, working principle: the observation of particles positions at two relatively close time instants. The flow to inspect is seeded with tracer particles, which are assumed to faithfully follow the flow dynamics without influencing it, and illuminated by a pulsed light source (usually a laser) in order to make these particles visible. By the comparison of two pictures taken by a high-speed camera in a small time interval, the displacement of each particle can be determined, and the instantaneous velocity field can thus be computed.

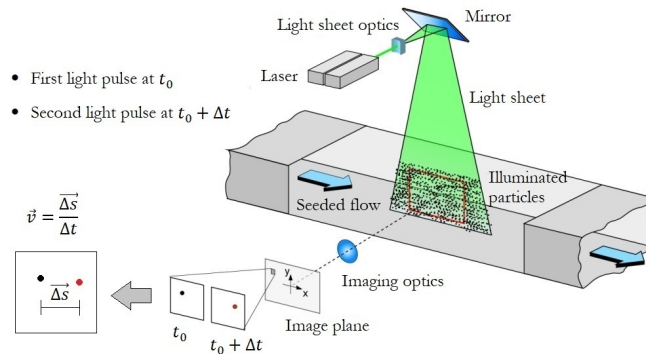


FIGURE 3.1. Scheme of a typical wind-tunnel PIV setup to illustrate the working principle.

The main components of a PIV setup are then the camera, whose sampling speed is a crucial factor for obtaining a pair of images close enough to estimate accurately the flow velocity, the laser sheet, which must provide a proper illumination and contrast at the right frequency, the seeding particles and a post-processing software which employs a correlation algorithm to extract the instantaneous velocity fields from the frames taken.

### 3.1.2. Seeding particles

The tracer particles used for the seeding of the flow are a critical component for any PIV system. Firstly, when possible they should match the fluid properties reasonably well in order to follow the flow as accurately as possible. Secondly, they must reflect and scatter towards the camera enough light to ensure a good visualization within the laser sheet plane. An appropriate choice of these particles is therefore necessary for obtaining reliable velocity measurements, and it should be made accordingly to the characteristics of the PIV setup employed and the flow inspected.

The size (namely the diameter) of the particles plays a central role in both the mentioned mechanisms, and thus it becomes the main parameter to take into consideration when selecting the seeding particles. For tracing purposes, particles density should match the fluid density in order to avoid systematic errors caused by buoyancy. However this is not possible when the fluid to inspect is a gas. Particles size, instead, should be as small as possible to faithfully follow the flow in their motion driven by viscosity and density. In fact, as a first estimation of the particle motion in relation to the fluid motion, it can be derived that the step response of the particle velocity  $U_p$  follows an exponential law:

$$U_p = U(1 - e^{t/\tau}) \quad (3.1)$$

where  $U$  is the step and  $\tau$  is the time constant, called relaxation time. For a spherical particle at low Reynolds number:

$$\tau = d_p^2 \frac{\rho_p}{18\mu} \quad (3.2)$$

where  $d_p$  is the particle diameter,  $\rho_p$  is the particle density and  $\mu$  is the dynamic viscosity of the fluid. By selecting a particle diameter small enough, one can minimize the time delay between the particle and the fluid motion and make it negligible in comparison with the smallest flow time scales of interest. This consequently ensures accurate and reliable velocity measurements.

On the other hand, the particles must be big enough to scatter sufficient light for imaging. The physical phenomenon of laser light scattering by a spherical particle can be described by the Mie solution to Maxwell's equations, also known as Mie scattering. By using this simplified approach, one can predict the right particle size to achieve a good scattering as well as the shape of the scattered light wave to optimize the position of the camera.

Moreover, the concentration and the distribution of tracer particles should be controlled in order to achieve a homogeneous seeding and a sufficient number of particles per interrogation window. Good seeding particles, finally, should also be non-toxic, non-corrosive and chemically inert for ease of use. Typical examples of particles used for this purpose are theatrical smoke, atomized oils and glass micro-balloons for gas applications, while silver-coated hollow glass spheres, polymers and titanium and aluminum oxides are employed for the seeding of liquid flows. The typical size of these particles, instead, is of the order of  $10 \mu\text{m}$ .

### 3.1.3. Pulsed light source and optics

Nowadays, double-frame single-exposure PIV is the most common PIV approach. Differently from single-frame double-exposure systems which record a single frame exposed by two laser pulses at two different time instants, double-frame systems take two different frames, one for each laser pulse. Either way short light pulses separated by a small time interval are required to provide a

bright illumination to the seeded flow. Pulsed lasers are therefore the natural choice to accomplish this task. In particular, Neodymium-doped Yttrium Aluminium Garnet (Nd:YAG) lasers represent the most commonly adopted solution. They emit primarily infrared radiation at a wavelength of 1064 nm, but for PIV applications their signal is bandpass filtered and the 532 nm harmonic (green light) is isolated to allow for particle illumination and reflection in the visible spectrum. Modern Nd:YAG lasers can provide power from 12 mJ to 1000 mJ. Due to the short time interval required between the two pulses, a PIV laser is constituted of two laser cavities, emitting two different pulses. These dual lasers systems permit to electronically adjust the two light sources with respect to each other, in order to achieve a wide range of pulse separations and to allow an external synchronizer to match the pulses timing with the PIV camera.

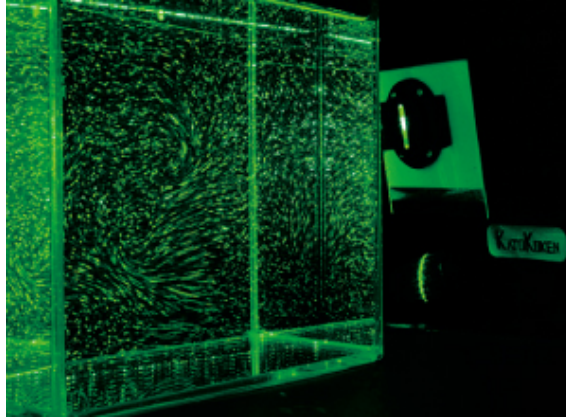


FIGURE 3.2. Green light sheet produced by a PIV Nd:YAG laser system and scattered by the seeding particles.

Usually a combination of cylindrical and spherical lenses are employed to turn the laser beam into a light sheet and to control its spread angle, thickness and direction. Mirrors can be used to deflect the sheet when it is not convenient to point the laser directly towards the inspection window.

#### 3.1.4. *Camera and calibration*

While in the past cameras were not fast enough and the only solution was to capture two exposures on a single frame, nowadays digital cameras are able to capture two different frames within a time interval of the order of 100 ns, allowing for the more reliable double-frame single-exposure approach. To do so, most of these cameras use Charge-Coupled Device (CCD) chips with available resolutions up to  $2672 \times 4008$  pixels. Depending on the resolution, these chips include the same amount of light sensitive pixels and storage cells. As soon as the first laser pulse exposes the first frame, this is transferred from the pixels

to the storage cells. The second frame, instead, is exposed by the second pulse and contained in the light sensitive pixels. Using a frame-grabber, these two frames are then transferred to the computer's RAM or to its hard drive for the processing. However, this fast capturing speed is restricted to a pair of frames, since each pair of shots must be transferred to the computer before another pair can be taken. This limits the actual framing rates of most of the cameras to a value of the order of 10 Hz. High speed cameras up to 1000 Hz are available for TRPIV (see subsection 3.1.7), but are significantly more expensive.

A proper calibration of PIV cameras is then required. This procedure is needed to establish a mapping relation between the frames image plane and the actual measurement plane, taking into consideration possible distortions introduced, for example, by the geometry of the flow-isolating glass. Such a relation is necessary to transfer the image plane displacements computed in pixels by means of correlation algorithms (see subsection 3.1.5) to the real measurement plane, and consequently obtain the real velocity fields. Usually this is accomplished by recording images of a calibration target, which contains calibration markers in known positions. Comparing known marker positions with corresponding marker positions on the images recorded, a mapping function is computed to relate coordinates on the image with positions in the real plane. Most of the times the mapping function is obtained by fitting a third order polynomial function such that:

$$x_1 = a_1 + a_2s + a_3t + a_4st + a_5s^2 + a_6t^2 + a_7s^2t + a_8st^2 + a_9s^3 + a_{10}t^3 \quad (3.3)$$

$$x_2 = b_1 + b_2s + b_3t + b_4st + b_5s^2 + b_6t^2 + b_7s^2t + b_8st^2 + b_9s^3 + b_{10}t^3 \quad (3.4)$$

where  $(x_1, x_2)$  is the position of a given point in the real measurement plane and  $(s, t)$  is the position of the same point in the image plane.

### 3.1.5. *Correlation algorithms*

Once the frames have been transferred from the camera to the computer, a post-processing software is needed for computing the velocity fields. For modern double-frame single-exposure PIV, these programs employ a cross-correlation algorithm to evaluate with a local statistical approach the displacements from each pair of high speed frames.

First, the image plane of the two frames is divided in several interrogation windows, whose size should be optimized considering the flow to inspect and the particles dimension. A typical size for an interrogation window is  $32 \times 32$  pixels. Usually a multi-pass iteration procedure with a decreasing sized, adaptive window and overlapping is employed to take into consideration particles entering and leaving the interrogation window between the two frames, improving the accuracy of cross-correlation outcomes. The algorithm itself is then based on the optimization of a cross-correlation estimator for each interrogation window. Such estimator is based on the classical cross-correlation of two signals, and,

in its integral form, can be written as:

$$R(\Delta x, \Delta y) = \iint_W I_1(x, y) I_2(x - \Delta x, y - \Delta y) dx dy \quad (3.5)$$

where  $I_1$  and  $I_2$  represent the light intensity field in the first and second frame respectively,  $(\Delta x, \Delta y)$  is the displacement for which the function is computed and  $W$  is the interrogation window area. For PIV evaluation, positions and displacements in the  $M \times N$  pixels interrogation window are described by a discrete coordinate system, and therefore the algorithm implemented computes the cross-correlation estimator in the following discrete form:

$$R(k, l) = \sum_{m=1}^M \sum_{n=1}^N I_1(m, n) I_2(m - k, n - l) \quad (3.6)$$

where  $(m, n)$  is the position in pixels and  $(k, l)$  is the displacement in pixels. Usually the Fourier transform is employed to reduce the computational power needed to evaluate the cross-correlation estimator, making the algorithm faster and stable.

The maximum value of this function, called correlation peak, is obtained for a displacement which superpose the light intensity peaks of the first and the second frame in the best possible way. Since light intensity peaks represent the tracing particles, the same optimal displacement can be assumed to be the most probable displacement of the particles between the two frames. Once this displacement value is known for each interrogation window, it is transferred to the real plane using the calibration function and finally the entire velocity field is computed. Filtering techniques might then be used to remove and replace via interpolation spurious vectors generated by failures in the cross-correlation computations.

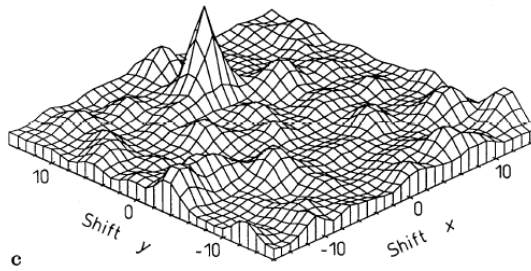


FIGURE 3.3. Plot of a typical cross-correlation function. The main correlation peak corresponds to particles displacement in the interrogation window. Reproduced from Dabiri (2006).

For single-frame double-exposed PIV, instead, an auto-correlation algorithm is implemented. This approach consists in cross-correlating the double-exposed frame with itself such that:

$$R(k, l) = \sum_{m=1}^M \sum_{n=1}^N I(m, n)I(m - k, n - l) \quad (3.7)$$

where  $I$  is the light intensity field of the single frame. Obviously, this auto-correlation function has its correlation peak corresponding to the zero displacement, and two smaller symmetric peaks which indicate the actual displacement. Due to the double exposure, no information about the time evolution of the motion is contained in the single frame, and thus the major issue with this approach is determining the direction of the displacement.

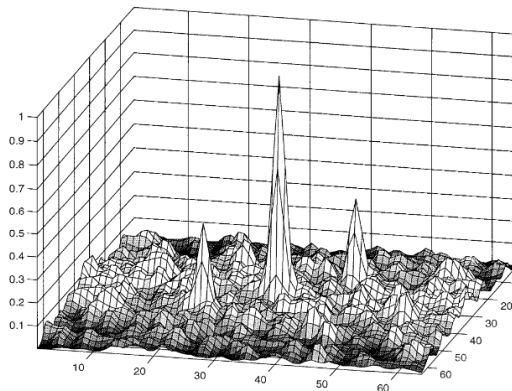


FIGURE 3.4. Plot of a typical auto-correlation function. The central peak represents the zero displacement, whereas the two symmetrical peaks correspond to particles displacement in the interrogation window. Reproduced from Marzouk & Hart (1998).

### 3.1.6. *Stereoscopic Particle Image Velocimetry*

Differently from classical PIV, Stereoscopic Particle Image Velocimetry (SPIV or 2D3C PIV) allows for the evaluation of all the three velocity field components in the measurement plane. Whereas in normal PIV the thickness of the laser sheet may introduce measurement errors due to a possible particles displacement in the normal direction, SPIV takes advantage of this to measure the third velocity component. Similarly to human three-dimensional vision, SPIV systems utilize two cameras with separate viewing angles to reconstruct a three-dimensional view of the flow in the measurement plane.

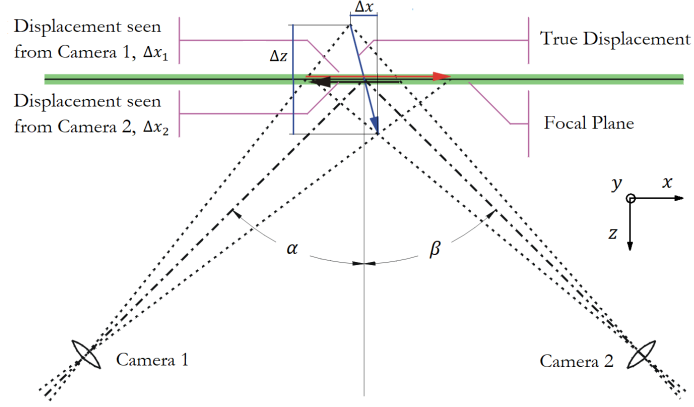


FIGURE 3.5. Stereoscopic principle. The cameras are considered aligned with the  $xz$ -plane, and thus the  $y$ -components are not taken into account.

Referring to Fig. 3.5, if the angles between the cameras views and the  $xz$ -plane are equal to zero, the true displacement can be obtained from the displacements measured by the two cameras as follows:

$$\Delta x = \frac{\Delta x_2 \tan \alpha - \Delta x_1 \tan \beta}{\tan \alpha - \tan \beta} \quad (3.8)$$

$$\Delta y = \frac{\Delta y_1 + \Delta y_2}{2} \quad (3.9)$$

$$\Delta z = \frac{\Delta x_1 - \Delta x_2}{\tan \alpha - \tan \beta} \quad (3.10)$$

where  $(\Delta x_1, \Delta y_1)$  and  $(\Delta x_2, \Delta y_2)$  are the displacements measured by the two cameras in their respective image plane,  $(\Delta x, \Delta y, \Delta z)$  is the real three-dimensional displacement and  $\alpha$  and  $\beta$  are the angles between the cameras views and the direction normal to the light sheet.

However, with standard camera configurations, the angular viewing required for SPIV leads to the problem that the light sheet plane is not completely contained in the camera focal plane. This causes blurring of the regions away from the focal plane during the recording. To avoid such focus problem, the camera configuration should fulfill the Scheimpflug principle. According to this criterion, the image plane, the lens plane and the object plane have either to be parallel or to intersect in a single point. While in normal 2D2C PIV the first condition is fulfilled, in SPIV an imaging arrangement, like tilting the lens with respect to the camera, is necessary to satisfy the second condition.

Furthermore, SPIV introduces a few difficulties in the calibration process of the two cameras. First of all, the calibration procedure has to account also for the viewing angle of each camera, and to determine how the images from the two cameras should be superposed. Secondly, a new procedure, called self-calibration, is required for Stereo PIV setups. This consists in a correction of the computed mapping function in order to take into consideration the misalignment between calibration plate and light sheet.

On the other hand, the advantages given by the use of this technique make up for the increased setup complexity. SPIV, in fact, makes it possible to measure all the components of the velocity in the plane inspected, and, when performed in multiple planes, it allows for the reconstruction of the entire averaged three-dimensional velocity field by means of interpolation, providing a complete visualization of the flow.

### **3.1.7. Recently developed PIV techniques**

In the last ten years, new PIV techniques have been tested and utilized for a deeper inspection of in-cylinder flows. This ongoing development has been following two major trends. On the one hand, the need for achieving fully three-dimensional measurements of instantaneous velocity fields has led the way to the introduction of PIV systems able to perform volume measurements such as Holographic PIV and Tomographic PIV. On the other hand, the interest in inspecting the time evolution of the flow and the introduction of high-frame rate cameras have promoted the development of Time-Resolved PIV systems.

Holographic PIV relies on the imaging technique called holography to record three-dimensional velocity fields in a volume. Whereas to acquire two-dimensional data only the intensity of the scattered light is to be measured, for three-dimensional information also the phase of the light wave has to be taken into consideration. To do so, the measurement volume is illuminated by a laser beam, which hits the tracer particles and gets scattered. Once the light has passed through the volume, it interferes either with the portion of the light that has not hit any particle (inline holography), or with another reference light beam expanded and used to illuminate the whole recording material (off-axis holography). Either way, an interfering pattern is created and recorded by a photo-sensitive emulsion on a film, creating an absorption grating. By illuminating the grating with a light wave at the same frequency of the original one, the original flow pattern can be reconstructed. Eventually, the three-dimensional patterns are post-processed using statistical cross-correlation algorithms or single particle identification.

For Tomographic PIV, the seeding particles in the flow are illuminated within a measurement volume, and the light scattered is recorded from several viewing directions simultaneously. Four to six digital cameras are typically employed for the recording. Three-dimensional light intensity fields discretized

in voxels (volumetric equivalent of pixels) are then reconstructed from the two-dimensional views using iterative tomographic algorithms. The complexity of this reconstruction problem is due to the large number of three-dimensional volumes that can result in the same two-dimensional views. The mapping function between the measurement volume and the image space is generated with a calibration procedure, similarly to what is done with normal PIV. Finally, particles displacements and thus velocity fields are obtained by applying three-dimensional cross-correlation.

Time-Resolved PIV, instead, has been made possible by the development of high-speed Complementary Metal-Oxide Semiconductor (CMOS) camera. In fact, the basic idea of TRPIV is rather straightforward: measuring the temporal evolution of turbulent and complex velocity fields using double pulsed PIV images in rapid succession. Nevertheless, the definition of time-resolved is not as clear as its purpose, and strongly depends on the flow to inspect. It can be said that PIV data are time-resolved when it is possible to track the flow structures throughout multiple consecutive velocity fields. This clearly depends on the mean velocity and the type of flow considered. The CMOS cameras used can record  $1024 \times 1024$  pixels-images with framing rates up to 5000 frames per second, and are coupled with Neodymium-doped Yttrium Lithium Fluoride (Nd:YLF) lasers capable of generating 20 mJ per pulse up to 10000 times per second. TRPIV has been implemented for both two-dimensional and Stereoscopic PIV.

### 3.2. Other experimental techniques

Although it is the most common one, Particle Image Velocimetry is not the only experimental technique for the inspection of in-cylinder flows. Both in the past and in recent times, different methods have been used for single and multi-point measurements of velocity fields within the cylinder walls of internal combustion engines. In the following subsections, the main features of these techniques are highlighted and their working principles are briefly explained.

#### 3.2.1. *Laser Doppler Velocimetry*

Laser Doppler Velocimetry was mainly employed in the early times, when the study of in-cylinder flows began to gain attention within the fluid dynamics research community. It is a single-point, non invasive measurement technique, capable of providing time-resolved data in a specific location within the flow field. Therefore it is adapt for the analysis of local turbulent fluctuations in flow velocity. The LDV working principle relies on the Doppler effect. Two laser beams, obtained by splitting a single beam, are crossed in the flow to measure. They interfere at their focal points, creating a set of straight fringes. The light reflected by particles added to the fluid when they pass trough these fringes is collected by a receiving optics. The frequency of the light intensity fluctuations is equivalent to the Doppler shift between the incident and scattered light and

thus depends on the particle velocity in the beams plane. By measuring the frequency of light intensity fluctuations generated by three different couple of beams, one can estimate all the velocity components in the selected location.

### 3.2.2. Particle Tracking Velocimetry

Particle Tracking Velocimetry (PTV), instead, represents one of the first experimental methods employed to obtain multi-point measurements of entire velocity fields. This approach is quite similar to PIV, since it is based on the visualization of the flow pattern by illumination and tracking of seeding particles. For illumination purposes, a laser light sheet is used in two-dimensional PTV, whereas in three-dimensional PTV volume illumination has to be provided. The major difference between PIV and PTV is the way the particles are tracked. In the former method, an Eulerian approach is used: PIV, in fact, statistically measures the velocity field of a fluid at a grid. Particle Tracking Velocimetry, instead, is a Lagrangian method, since it follows and tracks the motion of single particles throughout several consecutive frames. Compared to PIV, a lower density of tracer particles is added to the flow in order to allow for the individual tracking of each one of them.

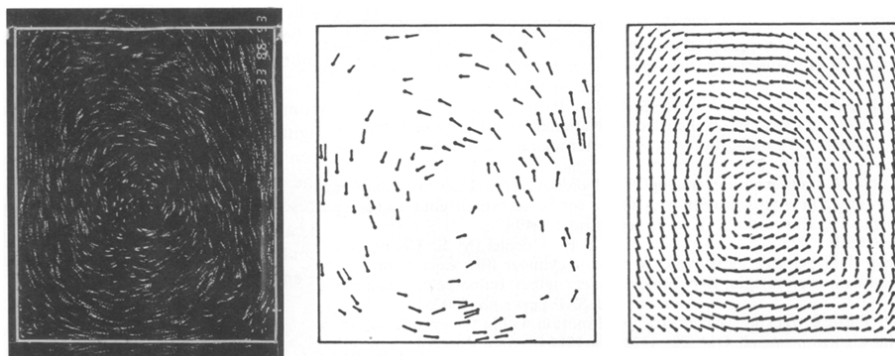


FIGURE 3.6. Original image, measured velocities and interpolated velocity field in a tumble plane using Particle Tracking Velocimetry. Adapted from Khalighi (1991).

### 3.2.3. Magnetic Resonance Velocimetry

Magnetic Resonance Velocimetry has recently been proposed as an alternative to PIV for three-dimensional measurements of in-cylinder flows. It is a non-invasive technique capable to measure entire three-component mean velocity fields in complex three-dimensional geometries. Furthermore, it does not need any optical access to the flow to be performed. It is based on the physical phenomenon of nuclear magnetic resonance of hydrogen atoms, and thus can

be used only for water flows. When atoms with an odd number of neutrons or protons are placed in a strong magnetic field, their randomly aligned angular spin momentum tends to align with the axis of the external field, causing a net magnetization. These spins normally precess about this axis at a frequency proportional to the field, but, when excited by a Radio Frequency (RF), they change their axis of precession. Moreover, the phase shift of a spin depends on the atom velocity. Therefore, by observing such spins using receiver coils, their phase can be determined and the local velocity of the flow can be derived.

### 3.3. Numerical methods

Since the 1980s, with the advancement of large-scale computers, Computational Fluid Dynamics has become a powerful tool for the inspection of complex and turbulent flows. Numerical simulations have found a wide range of applications both in the academic and in the industrial field for the study of different problems of engineering interest. However, the adoption of CFD for the study of in-cylinder flows is more recent, and it has only been made possible by developments in the methods used. Such flows, in fact, feature a marked turbulent and unsteady behaviour which makes them harder to predict with numerical tools.

Although several approaches with different numerical complexity are nowadays employed, the principle is the same: all the CFD codes solve the Navier-Stokes equations (subsections 2.2.1 and 2.2.2) in a three-dimensional domain by means of numerical methods. The difference among these approaches usually lies in the form of the governing equations they deal with. Whereas the most demanding simulations aim to solve the complete set of Navier-Stokes equations in the whole domain, less-requiring methods rely on modeling to solve an averaged, and thus simplified, set of equations.

As mentioned in chapter 1, the study of turbulence and turbulent flows with a numerical approach is complex and time consuming from a computational point of view. This is due to the nonlinear structure of the governing equations and to the wide range of time and length scales that play an important role in turbulent phenomena (see subsection 2.2.3). Since the ratio between the largest scales of turbulence  $\Lambda$  and the smallest ones  $\eta$  can be estimated as:

$$\frac{\Lambda}{\eta} = Re_{\Lambda}^{3/4} \quad (3.11)$$

if one were to numerically solve the complete three-dimensional Navier-Stokes equations set taking into consideration all the relevant length scales of the flow, the number of grid points to use would grow with  $Re_{\Lambda}^{9/4}$ . Considering then that also the range of significant time scales can be assumed to grow with  $Re_{\Lambda}^{3/4}$ , the number of computational steps required for the complete solution would be of the order of  $Re_{\Lambda}^3$ . It is clear how such an approach is only feasible for low

Reynolds number flows, whereas for in-cylinder flows, which are usually characterized by a Reynolds number of the order of  $10^5$ , other simplified methods are preferred.

In the next subsections, a short overview of the main categories of numerical methods and their features in relation to their applications in in-cylinder flow research is provided. These three approaches are treated in order of decreasing complexity, starting from the most complete and computational power requiring. For any reference to numerical studies present in the literature, see section 4.6.

### 3.3.1. *Direct Numerical Simulation (DNS)*

In Direct Numerical Simulations, the complete set of three-dimensional unsteady Navier-Stokes equations is solved numerically in its entirety. No turbulence modeling is applied and all the significant flow scales are taken into consideration when the geometrical and time domains are discretized. Different numerical methods can be employed to solve the governing equations: spectral methods, finite differences and finite volumes methods are the most commonly used. It is the most straightforward, complete and accurate CFD approach, and provides a high quantity and quality of output information, impossible to acquire with other methods.

However, the huge computational power required to completely solve the Navier-Stokes equations, especially for strongly turbulent flows, limits its usage to a small range of applications. DNS is nowadays employed only for the inspection of transitional or low-Reynolds number turbulent flows in simple geometries. It hardly ever finds applications in the industry, where less time consuming methods are largely preferred, not to mention that a DNS of most of the flows of interest would exceed the capacity of the most powerful computers available. Instead, it is often used in the research field for numerical experiments since it allows to simulate turbulence and collect data and information difficult to obtain in the laboratory. Moreover, it can also be an useful instrument for the development and the verification of turbulence models used in simplified CFD approaches.

Nowadays, a Direct Numerical Simulation of the flow within the cylinder walls of an internal combustion engine is barely feasible for simplified geometries at low Reynolds numbers, far away from real operating conditions. Only a continuous improvement of CPUs and the consequent increase in computational power available can widen the range of DNS applications to in-cylinder and other industrial flows in the future. Anyway, such developments are not realistically achievable within the next twenty years (Johansson & Wallin 2017), and thus DNS will remain mostly a research tool.

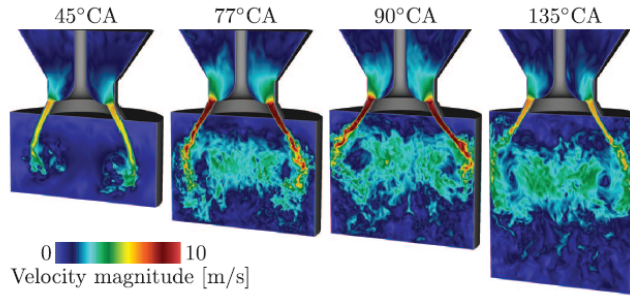


FIGURE 3.7. Result of a Direct Numerical Simulation at different crank angles during the intake stroke of an engine with a simplified geometry at low Reynolds number. Reproduced from Schmitt *et al.* (2014).

### 3.3.2. Large Eddy Simulation (LES)

Large Eddies Simulations represent an intermediate method for the inspection of flows behaviour. In fact, turbulence is neither completely solved nor totally modeled in the LES approach. In this sense, such simulations can be located halfway between DNS and RANS methods (the latter, as explained in the next subsection, reckon on the complete modeling of turbulence). LES methods, as highlighted by the name, capture the unsteady dynamics of large turbulent eddies by numerically solving Navier-Stokes equations for the larger turbulent scales, whereas smaller scales are not directly considered in the numerical solution. Instead, turbulent modeling is implemented to take into account this smaller, Sub-Grid Scales (SGS). This approach is justified by the features and the energetic content of the different scales: while larger eddies contain the most part of the energy and are strongly dependent on the geometry of the problem, smaller scales contain a small energy fraction, and are normally considered as isotropic and independent from the specific problem.

This separation between large scales to solve and small scale to model is achieved using a filter, which can be spatial, temporal or both. Different kind of filter can be used to divide the velocity scales in these two groups. In particular, every filter features a characteristic cut-off length and/or time scale. By applying the filter to the Navier-Stokes equations, a set of equations similar to the Reynolds Averaged Navier-Stokes equations is obtained. Differently from the RANS equations, the unknowns are instantaneous filtered fields. However, a term depending on the filtered out components appears in this new set of equations, and thus turbulence modeling of SGS is necessary as it is for the Reynolds stress tensor in RANS equations.

When it comes to advantages and disadvantages, LES can be considered as a trade-off between DNS and the RANS approach. The computational

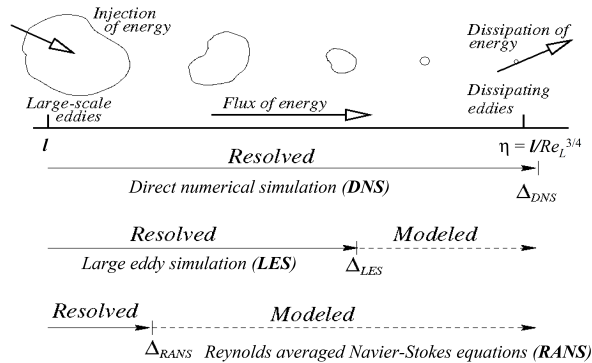


FIGURE 3.8. Turbulence modeling in DNS, LES and RANS approaches. Reproduced from Bakker (2006).

power required is lower than for DNS, and thus engineering-related turbulent flows with relatively high Reynolds numbers can be simulated. Nevertheless, LES still manages to predict complex unsteady phenomena, which can not be predicted by RANS simulations. Furthermore, SGS modeling is easier and its influence is smaller compared to turbulence modeling in RANS methods. However, the time required for a LES is longer than for a RANS simulation and filtering and defining a cut-off frequency are not trivial operations. Due to their accuracy and their reasonable CPUs requirements, LES methods have recently made their way in the in-cylinder flows research field. In fact, different LES studies have been published in the last years proving good agreements with experimental data and prediction ability. Although these studies have demonstrated LES methods to be suitable for in-cylinder flows inspection, the computational time required for a simulation is still quite prohibitive, and therefore the use of LES codes in the industry is nowadays rather limited.

### 3.3.3. Reynolds Averaged Navier-Stokes (RANS)

RANS simulations represent the industry standard for the prediction of complex flows. Turbulence is completely modeled in RANS methods, and this allows for a critical reduction of the computational time required for simulating turbulent flows. This approach aims to predict the averaged properties of the flow by solving the Reynolds Averaged Navier-Stokes equations, presented in subsection 2.2.4 in their incompressible form. In fact, for most of the flows of industrial interest, the understanding of mean quantities behaviour is more relevant than the comprehension of instantaneous fields and turbulent fluctuations.

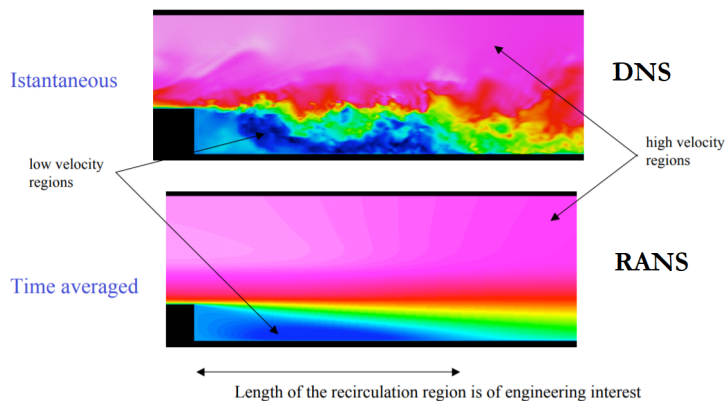


FIGURE 3.9. A comparison between RANS and DNS outcomes for the simulation of the flow over a backstep. Adapted from CTR Stanford (2004).

To solve the already mentioned turbulence closure problem, different turbulence models for the Reynolds stresses have been presented and tested throughout the years. In particular, the vast majority of turbulence models used for RANS CFD is based on the eddy viscosity approximation proposed by Boussinesq in 1877. According to this hypothesis, turbulent mixing acts in a similar way as molecular mixing, and thus can be modeled with a turbulent (or eddy) viscosity. Analogously to the Newtonian fluid stress description (Eq. 2.9), the Reynolds turbulent stresses is then expressed as follows:

$$-\rho \langle u'_i u'_j \rangle = \rho \nu_T \left( \frac{\partial U_i}{\partial x_j} + \frac{\partial U_j}{\partial x_i} \right) - \frac{2}{3} \rho K \delta_{ij} \quad (3.12)$$

where  $\nu_T$  is the eddy viscosity. Differently from  $\nu$ , which is a property of the fluid itself, turbulent viscosity is a property of the flow. The eddy viscosity is assumed to be governed by the length and velocity scale of the large energetic eddies.

The most common approach to compute such viscosity in RANS simulations is by applying the  $K - \varepsilon$  eddy viscosity model. This model assumes the turbulent kinetic energy  $K$  and its dissipation rate  $\varepsilon$  to be related to the length and velocity scales of the larger eddies, and thus estimates  $\nu_T$  as:

$$\nu_T = C_\mu \frac{K^2}{\varepsilon} \quad (3.13)$$

where  $C_\mu$  is a model coefficient. By solving two model transport equation for  $K$  and  $\varepsilon$  along with the RANS equations for the averaged flow, this common approach allows for the prediction of the mean flow behaviour.

The main advantage in the use of RANS simulations is obviously the short computational time required in comparison with other methods, and the good prediction ability for certain type of flows. However, the marked influence of the turbulence model applied and its parameters limits its applications to the specific suitable flow cases the simulation was set up for. Along with this lack of generality, the poor performances of RANS methods with some unconfined, rotating or large strains flows represents the main drawback of this approach. Although the flow swirling motion in Diesel engines belongs to such cases, RANS simulations have been proven useful tools to support the engine design process. Consequently, several in-cylinder flow studies employing RANS methods are present in the literature.



## CHAPTER 4

### Previous studies

This chapter presents a summarizing review of the literature regarding in-cylinder flow research. Due to the nature of this thesis work, this review is mostly focused on experimental studies performed by means of PIV. Nonetheless, some numerical studies, as well as experimental studies using different techniques, are dealt with in the respective sections.

#### 4.1. Introduction

Gas motion during the intake and compression strokes plays a vital role in controlling the combustion process in spark ignition engines, as well as the fuel-air mixing and combustion in Diesel engines. Therefore, emissions and fuel consumption are strongly affected by the features of the in-cylinder flow. Due to the increasing strictness of international emissions standards and the competitiveness of nowadays automotive market, the study and the optimization of gas flow in the cylinder have become necessary to improve engine efficiency while keeping emissions under the imposed limits.

Early experimental studies aiming to achieve a better understanding of the in-cylinder flow features were mostly based on single point measurements, using techniques such as Laser Doppler Velocimetry to study flow turbulence (Morse *et al.* 1979; Kang & Reitz 1999). However, in the last decades the experimental inspection of the entire velocity field within the cylinder walls has emerged as necessary for understanding the complex, three-dimensional flow field and its coherent structures, such as tumble and swirl. A complete inspection of the velocity field is also crucial for improving the optimization process. In fact, parameter-based optimization is no longer sufficient and has given way to a new approach based on the study of the flow in its entirety.

Because of its features that allow for the inspection of whole velocity fields, Particle Image Velocimetry has gained popularity through the years. While in some early work also Particle Tracking Velocimetry was used to describe the development of coherent structures during the intake stroke (Khalighi 1991), from the late 1990s PIV has become the dominant experimental technique for velocity measurements in turbulent and complex flows (Westerweel *et al.* 2012).

## 4.2. Planar PIV studies

Most of the studies performed in the last decades have used classical two-component planar PIV for the measurements in horizontal and vertical planes. For example, Reuss (2000) utilized 2D2C PIV in a Spark Ignition engine to inspect horizontal planes at end-compression and to study the cyclic variability of the flow at different length scales using different resolutions. Both a high-swirl and a low-swirl flow were inspected, demonstrating the possibility to create an in-cylinder flow where every cycle appears as the ensemble mean (high-swirl, directed flow) and an in-cylinder flow with high cyclic variability (low-swirl, undirected flow). Moreover, a schematic explanation of the mechanism generating cycle to cycle variations was given.

In a follow-up work (Funk *et al.* 2002), the kinetic energy and the turbulence parameters as defined by the Reynolds decomposition were studied in the two aforementioned cases. An increased resolution was used to look into a wider turbulence spectrum. It was proved that the high-swirl flow was less turbulent than the low-swirl one, while the mean kinetic energy was higher in the first case. Another study focusing on turbulent spectra performed by means of 2D2C PIV in a horizontal plane was carried out by Sick & Fajardo (2009): a Direct Injection Spark Ignition (DISI) engine was used and, as expected, the maximum total kinetic energy was found to decrease with decreasing length scales. Moreover, increasing swirl and engine speed were shown to lead to an increase in both kinetic energy and dissipation rate.

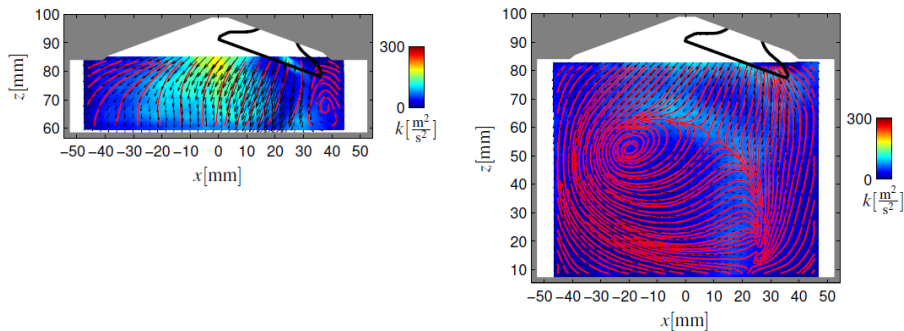


FIGURE 4.1. Average velocity vectors, streamlines and color-coded turbulent kinetic energy during the intake stroke at  $60^\circ$  ATDC and  $140^\circ$  ATDC respectively. Adapted from Danne-mann *et al.* (2009).

While the analysis of turbulence is important from a theoretical point of view, most of industry-driven experimental studies focus on the observation of generation and breakdown of coherent structures, such as swirl and tumble, during the first two strokes. Following this trend, Alger *et al.* (2004) compared

two different SI engines at several operating conditions (namely varying engine speed and intake pressure), and studied velocity mean values as well as swirl ratios. Swirl development in horizontal planes was inspected to detect the configuration that generates the strongest swirling motion. In Zha *et al.* (2015), the focus is on the study of variations in the position of the swirl center with height in an optical Diesel engine with swirl-controlling ports. To do this, a vortex tracking algorithm was used, and different crank angles and swirl ratios were inspected during the compression stroke.

In Murali Krishna & Mallikarjuna (2011) and Dannemann *et al.* (2009), instead, PIV measurements were performed in vertical planes to describe the evolution of the tumbling pattern during intake and compression in SI engines. In the first study, the evolution of the averaged flow was analysed at different engine speeds, proving that the general flow pattern and the tumble ratio are affected more by the crank angle than by the engine speed. In the second one, an analysis of the turbulent kinetic energy and an evaluation of vortical structures were carried out.

### 4.3. Recent PIV implementations

With the development of new cameras and imaging systems, new PIV methods have been employed in the study of in-cylinder flows over the last ten years, allowing for both a three-dimensional and time resolved analysis of the velocity fields. In this sense, one of the most used PIV techniques is nowadays Stereo PIV, which enables the measurements of all the three velocity components in a plane. Thanks to the measurements of three-component velocity fields in different planes, the averaged three-dimensional velocity field can be reconstructed via interpolation. This approach was pursued by Bückner *et al.* (2012) for studying the evolution and the breakdown of the tumble vortex in a DISI engine during intake and compression, taking advantage of the volumetric visualization of the flow. Rabault *et al.* (2016) performed a three-dimensional reconstruction of the velocity field during intake to evaluate the features of the swirling pattern in several horizontal planes and compare the swirl ratio obtained from PIV data with the one measured with a honeycomb straightener. Differently from the vast majority of the studies mentioned, they did not use any piston in their steady-state setup, assuming a negligible influence of the moving surface on swirl motion features.

However, most of the times Stereo PIV is coupled with a time-resolved approach in order to obtain a complete description of the flow in the domain of time: this was made possible by the introduction of new high-speed cameras able to go up to frequencies of the order of 1 kHz. Voisine *et al.* (2011), for example, employed a Time-Resolved PIV system to study the evolution of the three-dimensional flow structure during intake and compression in a moderate tumbling ratio SI engine. The jet and its interaction with cylinder walls were believed to be the causes of the generation of high cycle-to-cycle variations

in the tumble structure at the end of the intake. Moreover, an increase in turbulent kinetic energy was measured during the tumble breakdown in the compression stroke, due to high cyclic variability and transfer to small-scale turbulence. Cosadia *et al.* (2007), instead, inspected a fixed horizontal plane by means of TRPIV in an optical CI engine. Using a statistical approach, they studied the main features of the swirling motion, its time evolution and its cyclic variations.

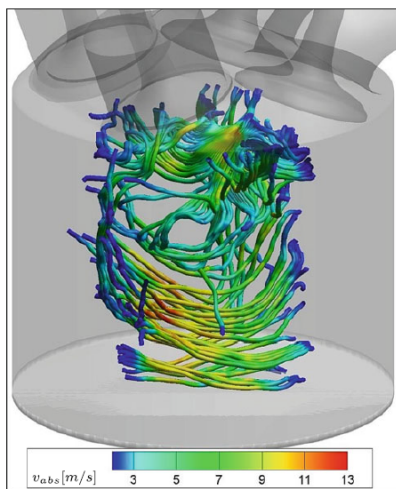


FIGURE 4.2. Three-dimensional distribution of streamlines color-coded by absolute velocity at  $160^\circ$  ATDC. Reproduced from van Overbrüggen *et al.* (2013b).

In the last years, the development of new PIV systems such as Tomographic PIV and Holographic PIV has made it possible to achieve, with some limitations, a full three-dimensional view of the in-cylinder velocity fields. The main drawbacks of these new methods are the difficult implementation and the small measurement volume. Singh *et al.* (2015) and van Overbrüggen *et al.* (2013a) both employed TPIV to study the air motion at different points during intake and compression in a CI and a SI engine respectively. In the first study turbulent kinetic energy distribution was analysed and the propagation of vortices was considered. In the second one, two different operating conditions were compared, and it was shown how different engine speeds affect the air motion leading to different velocities in the cylinder.

Since these technologies are quite recent and still under development, most of the related studies focus on proving the feasibility and the reliability of such measurements. As an example, van Overbrüggen *et al.* (2013b) proved the feasibility of HPIV in comparison to planar PIV with a study involving the

analysis of three-dimensional streamlines, vortices and integral length scales. Zentgraf *et al.* (2016), in a study focused mostly on turbulence and cycle-to-cycle variations, obtained a good agreement comparing Reynolds stress tensor components between two-dimensional PIV and TPIV measurements performed in a DISI engine, while Baum *et al.* (2014) used normal PIV, SPIV and TPIV in the same kind of engine to build a database for the validation of numerical simulations. They obtained an excellent agreement among measured average and standard deviation values. By doing so, they proved an overall reproducibility and reliability of engine operations and PIV measurements.

#### 4.4. The water-analogue engine

While the vast majority of the studies already mentioned utilize air as the working fluid to reproduce real engines operating conditions, the water-analogue engine approach has also been followed for the inspection of the intake stroke. The main assumption of such approach is the incompressibility of the flow during this stroke (Khalighi & Huebler 1988), which allows for the use of water, and consequently for better resolved optical measurements, as long as the original Reynolds number is matched. One of the first studies in this field was the already mentioned work by Khalighi (1991): the tumble vortex was observed in a vertical plane and it was found that varying the engine speed does not affect significantly its structure.

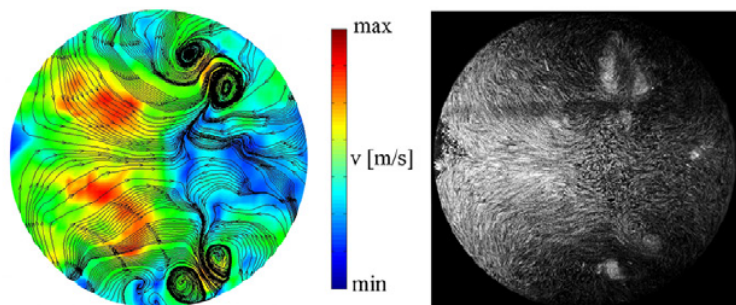


FIGURE 4.3. Velocity magnitude, streamlines and particle-pathline visualization by image superposition in a swirl-plane 1 mm away from the piston surface at  $71.5^\circ$  ATDC. Adapted from Koehler *et al.* (2015).

More recently, Koehler *et al.* (2014) developed a “flying TRPIV” setup to inspect a moving horizontal plane kept a distance of 1 mm from the piston surface throughout the stroke. They observed the stretching of horse-shoe vortices generated in the proximity of the intake valves of a four valves water analogue engine. The same setup was used in Koehler *et al.* (2015) to focus

on the evolution of the flow near the piston crown and its interactions with cylinder walls. Mean flow vortices were believed to be the footprint of the valves wake, while instantaneous ones were studied to highlight cycle-to-cycle variations. The study by Hess *et al.* (2012) justified the use of a glycerol-water mixture comparing the results obtained with measurements performed with pure water in a four valves engine. The glycerol mixture allowed to avoid distortion caused by refractive index disparities with the cylinder walls and to obtain highly resolved volumetric data.

Using the same setup employed for this thesis work, Kalpakli Vester *et al.* (2018) demonstrated that the influence of the Reynolds number on large-scale vortical structures is neglectable when the physical quantities are properly scaled. They studied the features of the swirl motion generated during the intake, comparing the flow fields obtained with fixed and moving valves. It was observed that valve motion does not seem to have a big influence on the flow.

#### 4.5. POD applications

In turbulent and in-cylinder flow studies, PIV datasets are often analysed by means of Proper Orthogonal Decomposition (POD). This data evaluation technique allows the decomposition of the database of all the flow realizations (i.e. engine cycles) in optimal modes from an energetic point of view (see subsection 5.3.1). Either phase-dependent POD or phase-invariant POD have been used in different studies to evaluate the main features of the flow. Borée *et al.* (2002) applied POD at the end of the intake stroke to study the behaviour of the tumble vortex in a vertical plane using a compression test engine with square piston and cylinder. They analysed the physical meaning of the most energetic modes and studied the mode spectrum. However, they agreed that POD does not offer an absolute separation between coherent structures fluctuations and the effect of fine-scale turbulence.

While phase-dependent POD is used mainly to filter out small-scale fluctuations and extract the most energetic structures in the flow for further analysis (Cosadia *et al.* 2006), phase-invariant POD provides a time-resolved view of the flow realizations, since the phase-invariant modes describe the time evolution of the flow (i.e. the entire stroke). Phase-invariant POD was first used by Fogleman *et al.* (2004) to study both intake and compression strokes in a vertical plane. By analysing the square of the time coefficients, they obtained information about the kinetic energy evolution and cycle-to-cycle variations. Druault *et al.* (2005) instead, used phase-invariant POD to extrapolate the velocity fields at any crank angle in a SI engine. In fact, once they extracted the time coefficients for the field they had measured, they reconstructed via temporal spline interpolation the velocity fields at any instant. Eventually they used all the velocity fields to evaluate cycle-to-cycle variations in the tumble pattern.

#### 4.6. Numerical studies

Along with the PIV measurements, numerical simulations play an important role in the study of in-cylinder flows. Although the complexity and accuracy of CFD codes have increased compared to the past, they still require an experimental validation to prove their reliability. While the RANS approach is common within the industry for its low computational power required, most of the research studies involve either LES or hybrid LES-RANS simulations, whereas the DNS approach is too requiring to be pursued in almost every case. In this sense, PIV datasets are often used to validate numerical studies since they allow comparison of the entire velocity fields.

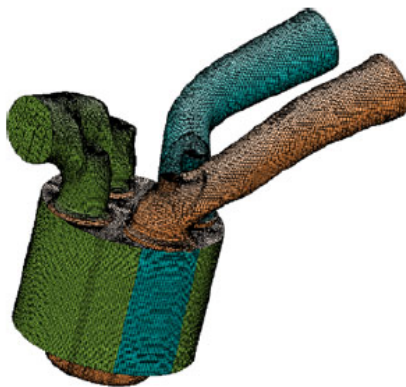


FIGURE 4.4. Full engine mesh at 90° ATDC for LES. Reproduced from Bottone *et al.* (2012).

Following this approach, Baumann *et al.* (2014) performed LES simulations reproducing the engine geometry used for PIV measurements by Baum *et al.* (2014). They obtained an excellent agreement with PIV data on statistical moments of single point velocity, where the only discrepancies were to be attributed to the incomplete statistical convergence due to the insufficient number of cycles simulated. They also proved a good reliability of the code in predicting the general flow pattern, even though they noticed some mesh influence. Bottone *et al.* (2012), reproducing the geometry of a Diesel engine, compared two different numerical approaches: LES and DES (hybrid approach between LES and RANS). They also simulated a spray injected motored engine, to illustrate how the turbulence affects the mixing of the two phases in the combustion chamber. It was found that the hybrid code seems to be more dissipative, leading to lower turbulence levels and cyclic variations.

Other comparisons between LES and PIV results were carried out by Yu *et al.* (2006) and Söder *et al.* (2012). In the first study both methods were used

to inspect the mechanism of turbulent production generated by the breakdown of large-scale, non-turbulent structures in a two valves Diesel engine. Using CFD results, they also gave an explanation of the temperature stratification phenomenon that occurs close to the cylinder walls. In the second study, the steady state setup used by Vernet (2012) for PIV measurements was reproduced and results from both RANS and LES were compared with experimental data. Different valve lifts were inspected, and higher cyclic variations were observed for smaller lift values. Overall, the LES simulation was found to be in good qualitative but not quantitative agreement with the experimental results.

As already mentioned, the application of DNS simulations for in-cylinder flows research is very prohibitive due to the computational power required, and only a single pioneering example can be found in the literature. Schmitt *et al.* (2014) used a DNS incompressible flow solver code to simulate intake and exhaust stroke at low Reynolds numbers ( $Re < 3070$ ) in a simplified geometry. They reproduced the single, fixed valve engine setup utilized for LDV measurements by Morse *et al.* (1979) and compared the outcomes. Only eight cycles were simulated, and a mesh study was carried out. Averaged fields streamlines and statistical moments at different locations and different piston positions showed a very good agreement with the experimental results, proving the DNS code to be able to predict both flow structures and local velocity values.

#### 4.7. Other experimental studies

Although the use of PIV has been spreading among in-cylinder flow researchers, there are also other experimental techniques which has been used for the study of these flows with different purposes. The aforementioned LDV has been often used to provide single point velocity measurements: Kang & Reitz (1999) studied two different intake port arrangements in a Compression Ignition engine, showing a good agreement between swirl ratios calculated using LDV data, and the ones measured with a honeycomb straightener. They found the aligned arrangement to be more effective for swirl generation, and the inclined one to be more sensitive to the effects on swirl motion caused by increasing the valve lift.

More recently, Magnetic Resonance Velocimetry was tested for the measurements of entire velocity fields: Freudenhammer *et al.* (2014) performed 3D3C MRV measurements in a steady state pistonless setup and compared them with PIV measurements at mid-intake in a DISI engine. The feasibility of this method was proved only in the upper part of the engine where the piston influence is neglectable: in this region a comparison between averaged flow field showed a good agreement with the unsteady, piston-limited flow from PIV measurements. In the second part of the study they carried out a detailed analysis of the area close to the valve and inside the intake port.

Other kind of measurements have been used mostly to gain a better understanding of the combustion process and how it is affected by the in-cylinder

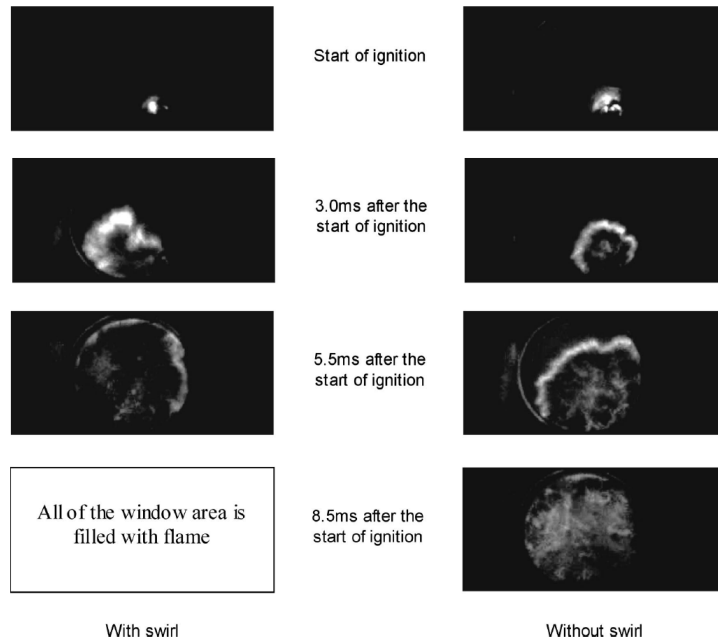


FIGURE 4.5. Effect of swirling motion on flame propagation in a SI engine. Adapted from Joo *et al.* (2003).

large-scale structures generated during the intake. In Joo *et al.* (2003), for example, a high frame-rate camera was used to analyse the flame propagation in a two valves Multi-Point Fuel Injection (MPFI) engine. A propagation model was developed, and the results matched well the experimental outcomes. Furthermore, the swirl ratio was observed to remain constant during combustion, and the swirling motion was found to cause a faster flame propagation. Jayakumar *et al.* (2012) measured different quantities such as fuel mass flow,  $\text{CO}_2$  percentage and hydrocarbons fraction at different swirl ratios and injection pressure in a common-rail Diesel engine. They studied the effects of different operating conditions on combustion and emissions, and they showed how an increase in the swirl ratio promotes premixed burn fraction and leads to an increased combustion quality, reducing soot formation and increasing in-cylinder temperatures. Due to the increase in temperature, an increase in  $\text{NO}_x$  generation was observed as well. They agreed on the need to optimize the swirl ratio to obtain a better combustion process.

#### **4.8. Conclusion**

In the present section, a short review of studies performed in the research field of in-cylinder flows over the last decades has been presented. It was made clear how PIV allows the tracking of large-scale coherent structures such as swirl and tumble. Those structures are of vital importance for the optimization process in the design of intake ports and combustion chambers, which aims to improve fuel consumption and reduce emissions. It is acknowledged how future studies should employ developing volumetric measurements like TPIV and HPIV to achieve a better understanding of the three-dimensional features of the flow in single cycles and for the validation of numerical simulations. Anyway, this review is not exhaustive and does not include all the topics studied by in-cylinder flow research: for a more detailed review the reader is referred to the report by Kalpakli Vester (2015).



## CHAPTER 5

### Experimental setup and data processing

In the current chapter, the experimental setup utilized for the measurements, the post-processing of PIV raw images and the data evaluation techniques used for the present work are described. Since the measurement campaign was not an active part of this thesis project, the focus is mostly on the post-processing and the data analysis procedure.

#### 5.1. Experimental setup

The PIV measurement campaign was carried out at the Fluid Physics Laboratory, Department of Mechanics, KTH in cooperation with Scania CV AB. The aim of the experiments was to characterize the behaviour of the flow during the intake stroke in a water-analogue engine, in order to evaluate the performances of a swirl-generating intake port geometry. A description of the main features of the engine setup utilized, as well as a brief review of the specifics of the PIV system employed, is given within the next subsections.

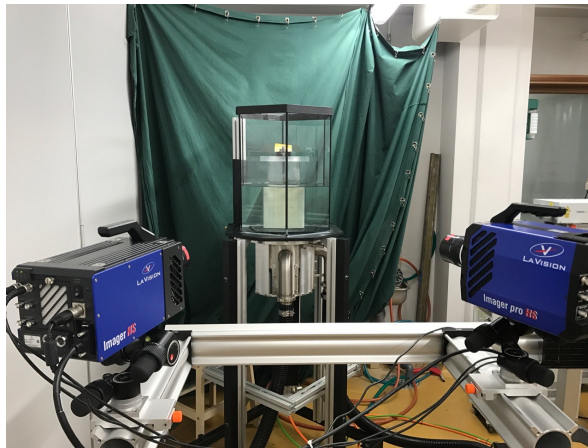


FIGURE 5.1. The Stereo PIV facility and the water-analogue engine setup at the Fluid Physics Laboratory, KTH.

### 5.1.1. The water-analogue engine setup

The experimental setup consists of an optically accessible model of a four-valve engine cylinder with a bore of 130 mm and a stroke of 160 mm. The same experimental cylinder, with different intake ports, has been utilized and described by Kalpakli Vester *et al.* (2018). The size of the model is typical of a heavy-duty Diesel engine, and the apparatus is of a generic nature, such that the cylinder head is interchangeable and valve timing can be easily configured. Since the purpose of this setup is the reproduction of the intake stroke, the exhaust valves are not present. Water is used as the operating fluid in this so-called water-analogue engine, and the cylinder is surrounded by a water-filled hexagonal tank for refractive index matching.

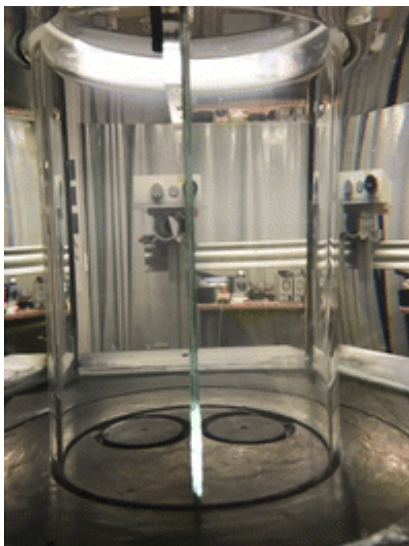


FIGURE 5.2. Close-up of the optically accessible engine model used for the measurements. Adapted from Kalpakli Vester *et al.* (2018).

Assuming the intake flow to be incompressible (Khalighi & Huebler 1988), it is in fact possible to use water instead of air as long as the similarity criteria between the model engine and the real engine at normal operating conditions are fulfilled. Keeping the same geometry of the original engine, the only parameter that needs to be matched is the Reynolds number defined as:

$$Re = \frac{U_p D}{\nu} \quad (5.1)$$

where  $U_p$  is the piston mean speed, and  $D$  is the cylinder bore. Since the ratio of kinematic viscosities of water and air at operating conditions  $\nu_{water}/\nu_{air}$  is

around 0.2 (see Kalpakli Vester *et al.* (2018)), the piston speed in the water-analogue engine model should be around five times smaller than the original one.

This would lead to a mean engine speed in the water-analogue setup of around 1 m/s. However, such piston velocity would cause cavitation issues in the valve flow channel (Koehler *et al.* 2015), and therefore lower piston speeds are used in water-analogue engine experiments (in this case the piston mean velocity is 0.16 m/s). Nevertheless, it has been shown that, as long as the velocity fields are scaled with the piston speed, variations of the Reynolds number have almost no effect on large flow structures (Hess *et al.* 2012; Kalpakli Vester *et al.* 2018) which are of interest in this study.

Such an alternative approach, based on fluid dynamics similarity, is followed because the use of water allows both for lower piston velocities and for refractive index matching, which leads to minimize loss of data due to light reflections. This makes it possible to obtain time-resolved and highly spatially resolved data with the cameras available nowadays. On the other hand, it has to be recalled that the use of water-analogue engine setups is limited to the inspection of the intake in a single stroke experiment, where the flow is started from rest. Furthermore, mixing phenomena between cold aspirated air and hot exhaust gases occurring in real internal combustion engines during the intake stroke can not be observed and studied by means of this approach.

Regarding the working operations, the intake valves and the flow are driven by two different linear motors: the first one controls the valve lift profile, the second one forces the water through the system, pushing the floating piston upwards in the cylinder as showed in Fig. 5.3. In fact, to minimize leakages, the whole engine is turned upside down. Therefore the Bottom Dead Center is when the piston is located at the highest position throughout the stroke.

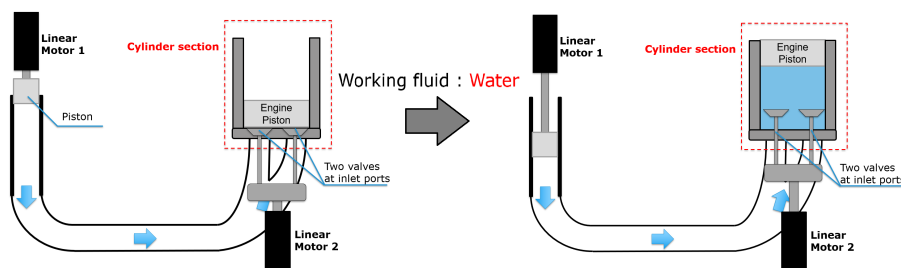


FIGURE 5.3. Scheme of the experimental setup. The valves and the flow are driven by two different linear motors.

The two linear motors, provided by LinMot®<sup>®</sup>, are synchronized so that a real engine intake stroke can be mimicked. As can be seen in Fig. 5.4, two different cases were evaluated: in the first one, the valve lift was kept fixed at

15 mm during the entire stroke, while in the second, realistic one, the valves were moving between 0 and 15 mm of lift according to a typical profile. The piston motion, instead, was kept the same between the two cases.

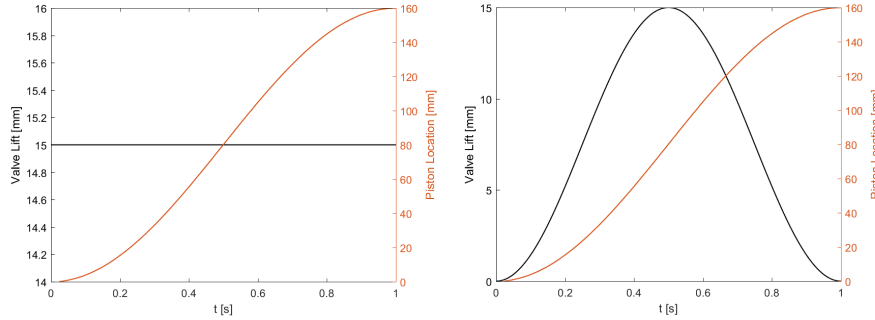


FIGURE 5.4. Valve lift and piston position profiles for the fixed (left) and the moving (right) valves case.

At the beginning of the intake stroke a clearance volume with a height of around 15 mm filled with still water separates the cylinder head from the flat-surfaced floating piston. The stroke duration is 1 s. The water is at room temperature, but the exact value has not been measured due to the small influence of viscosity and thus Reynolds number variations on large-scale structures. The geometrical properties of the engine, as well as the operating conditions, are summarized in Tab. 5.1.

Bore	130 mm
Stroke	160 mm
Intake Stroke Duration	1 s
Piston Mean Speed	0.16 m/s
Model Engine Speed	30 rpm
Re	26000

TABLE 5.1. Engine geometrical properties and operating conditions.

### 5.1.2. PIV system and measurements plan

The Stereo PIV system utilized for the experimental campaign is from LaVision GmbH and consists of two high-speed cameras (Imager Pro HS 4M, 2016 × 2016 pixels resolution) and a Litron Nd:YAG laser. For the seeding of the flow, Vestosint particles with a diameter of 56  $\mu\text{m}$  were mixed with the water.

Time-Resolved Stereoscopic PIV measurements were performed in different vertical planes to obtain three-component velocity fields. This was accomplished by rotating the whole cylinder around its axis, in order to avoid moving or recalibrating the PIV system. The purpose of such multi-plane measurements was the reconstruction of the averaged three-dimensional velocity fields from planar data by means of linear interpolation, which allows for the study of the swirling motion occurring in the flow. However, due to technical problems, only 17 consecutive planes with a  $9^\circ$  step between them were inspected, instead of the 21 required for a complete equi-spaced coverage of the entire 360 degrees. Consequently, a  $36^\circ$  interpolation gap is present between the  $144^\circ$  and the  $0^\circ$  planes. To move from a plane to the other, the cylinder head was rotated counterclockwise, so that tumble planes are rotated clockwise relative to the previous ones (Fig. 5.5).

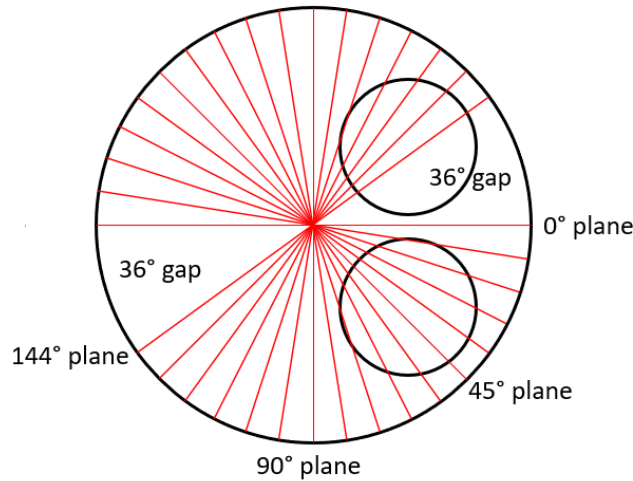


FIGURE 5.5. The traces of the inspected vertical planes as seen from inside the cylinder.

For each plane, the SPIV data were sampled at a frequency of 200 Hz in a time interval of 1.05 s resulting in 210 fields obtained per cycle and providing a time-resolved coverage of the intake process. The last 10 frames for each cycle were taken after the end of the stroke to inspect the dynamics of the flow once the piston stops moving. In both the moving and fixed valves case, around 50 cycles per plane were evaluated to obtain a good convergence of phase-averaged fields (based on the correlation coefficient between phase-averaged quantities). The entire measurement campaign scheme is summarized in Tab. 5.2.

	Fixed Valves	Moving Valves
0° plane	53 cycles	59 cycles
9° plane	54 cycles	53 cycles
18° plane	52 cycles	53 cycles
27° plane	61 cycles	57 cycles
36° plane	58 cycles	56 cycles
45° plane	51 cycles	58 cycles
54° plane	62 cycles	55 cycles
63° plane	51 cycles	56 cycles
72° plane	55 cycles	56 cycles
81° plane	52 cycles	56 cycles
90° plane	51 cycles	59 cycles
99° plane	58 cycles	46 cycles
108° plane	50 cycles	54 cycles
117° plane	50 cycles	52 cycles
126° plane	52 cycles	51 cycles
135° plane	51 cycles	57 cycles
144° plane	53 cycles	53 cycles

TABLE 5.2. Scheme of the measurement campaign plan.

## 5.2. PIV post-processing

Once the measurement campaign was finished, the database of time-resolved PIV raw data had to be processed to extract all the velocity fields and to export them in a format suitable for the evaluation. At the beginning, only a fraction of the total dataset had been processed in order to gain familiarity with the database, to assess the quality of the measurements and to carry out a preliminary analysis. Eventually, the processing of the entire experimental database was performed. The different options used in the post-processing, as well as the format and the reference frame of the extracted velocity fields are described in the next subsections.

### 5.2.1. Images processing

For the processing of PIV images, the commercial software DaVis 8.3.0 by LaVision GmbH has been used. As already mentioned, the analysis of the images database has been carried out in two phases: in the first one, for each inspected cycle, one frame of every four was processed, resulting in 53 processed velocity fields out of 210 frames taken. For this first 50 Hz elaboration, the vector fields were calculated using CPU computing through a multi-pass correlation iteration procedure for increased spatial resolution. The iterative algorithm

employed starts from a  $64 \times 64$  pixels window size to decrease to a  $16 \times 16$  pixels interrogation area with 50% overlap.

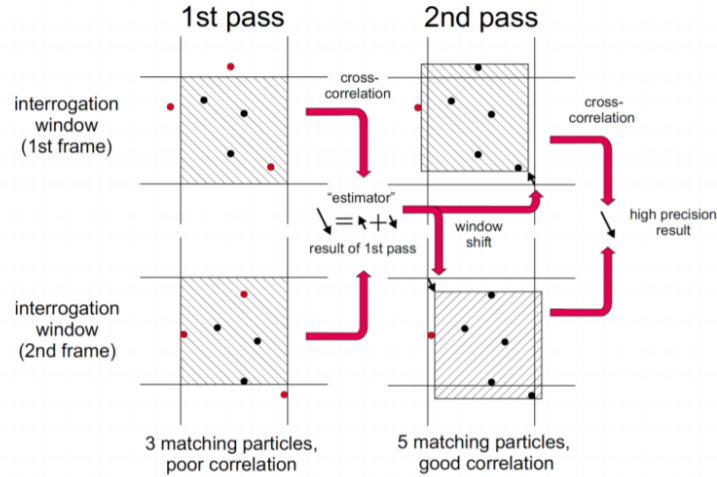


FIGURE 5.6. Working principle of a multi-pass cross-correlation algorithm. Reproduced from Dembinski (2013).

During the second phase of the analysis, the entire 200 Hz database was processed. To do so, due to the extended amount of computational time otherwise required, some processing settings had to be modified. In fact, GPU computing was used to speed up the elaboration of the particle images: a multi-pass correlation iteration procedure decreasing from  $64 \times 64$  pixels to  $32 \times 32$  pixels interrogation area with 50% overlap was employed. The usage of GPU hardware acceleration (CUDA PIV) allows for an increased processing speed without affecting the output results. However, due to differences in the CPU and GPU codes, some processing options are not available for the CUDA PIV. Nevertheless both methods give the same precision and robustness in calculating the vector fields (LaVision GmbH 2015). Once the elaboration was over, all the velocity fields, from both the partial 50 Hz and complete 200 Hz database processing operation, have been exported with DaVis and saved as ASCII files.

### 5.2.2. Data format and frames of reference

In each ASCII file, in-plane coordinates and the three components of the velocity field are given: the first two columns represent the  $x$  and  $y$  coordinate of the vector location, whereas the last three columns contain the components of the velocity vectors along the  $x$ ,  $y$  and  $z$  direction respectively. The reference

frames relative to the inspected vertical planes are defined as shown in Fig. 5.7. The reference frame of each plane is rotated clockwise relative to the frame of the previous one, and they all share the same  $y$ -axis which coincides with the cylinder axis.

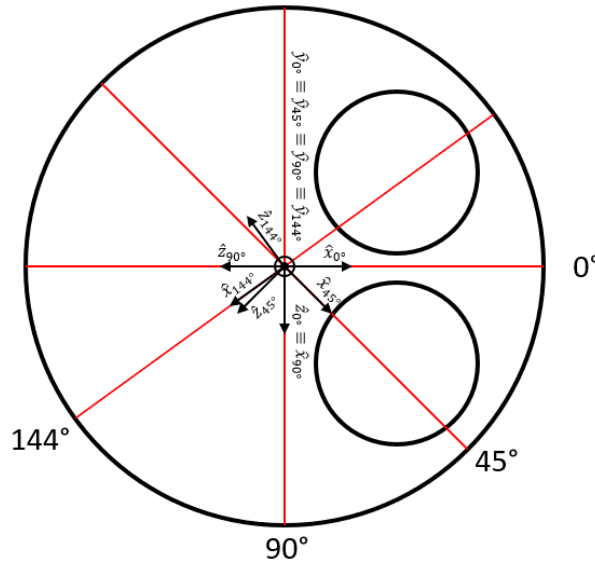


FIGURE 5.7. Frames of reference of the most significant inspected planes as seen from inside the cylinder.

The velocity fields have been processed and exported on a  $276 \times 249$  grid with a spacing in the  $x$  and  $y$  direction of  $0.7475$  mm. It covers an area of around  $380 \text{ cm}^2$ . Due to a bug in the post-processing procedure, the grid used to evaluate and export the velocity fields measured in the  $0^\circ$  plane with fixed valves is slightly different from the one just mentioned. In fact, a  $279 \times 250$  grid with a neglectable difference in the  $x$  and  $y$  spacing ( $0.7475$  mm and  $0.7474$  mm) was utilized in this case. Anyway, this different grid covers almost the same area as the other grid, and represented a problem only when the velocity fields had to be imported into MATLAB<sup>®</sup>.

### 5.3. Evaluation techniques

Different data evaluation techniques have been used to inspect the experimental database in order to study, analyse and highlight important features of the flow. Hence, the next subsections go through an introduction and a superficial

mathematical description of such techniques, providing a general background useful for the understanding of the outcomes.

### 5.3.1. Proper Orthogonal Decomposition (POD)

Among all the statistical tools employed in the analysis of complex turbulent flows, Proper Orthogonal Decomposition has received a particular attention by the fluid dynamics research community. From its first implementation for the study of turbulence (Lumley 1967), POD has found a wide range of applications. Recently, it has been employed, in its different forms, for the analysis of in-cylinder flows (Borée *et al.* 2002; Moreau *et al.* 2005) and for the comparison of experimental and numerical datasets (Fogleman *et al.* 2004; Meyer *et al.* 2007).

Proper Orthogonal Decomposition can be described as a “powerful and elegant method of data analysis aimed at obtaining low-dimensional approximate descriptions of high dimensional processes” (Chatterjee 2000). Based on the Karhunen-Loève theorem, this statistical tool has been used in various disciplines other than fluid mechanics, since it provides an optimal modal decomposition of an ensemble of functions such as data collected during an experiment. POD is then used to analyse experimental data with the purpose of extracting dominant features and trends, or coherent structures and flow patterns when it comes to fluid dynamics velocity data. To understand POD optimality, a brief mathematical introduction is necessary. However, for a detailed discussion of Proper Orthogonal Decomposition properties, and for its mathematical derivation, the reader is referred to Holmes *et al.* (1996).

Finite-dimensional POD is applied to experimental data to find an optimal orthonormal basis for an ensemble of vectors containing measured quantities. Assume that we have an experimental database made of an ensemble of  $N$  measurement sets. Each of these sets features  $m$  measured values at different positions. In our case, we have  $N$  engine cycles inspected and  $k$  vectors measured per velocity field. This gives us  $m = 3k$ , since we take into consideration all three velocity components. The measurement database can thus be represented as an  $N \times m$  matrix  $A$ , where  $A_{ij}$  is the measurement taken in the  $i$ -th set at the  $j$ -th position. As any modes decomposition, POD provides a basis of  $N$  orthonormal vectors  $\Phi^{(j)}$  such that any measurement set  $\mathbf{a}^{(i)}$ , which corresponds to the  $i$ -th line of the matrix  $A$ , can be expressed as a linear combination of the basis vectors (or modes):

$$\mathbf{a}^{(i)} = \sum_{j=1}^N q^{(i,j)} \Phi^{(j)} \quad (5.2)$$

where  $q^{(i,j)}$  is the scalar coefficient relative to the  $i$ -th set and  $j$ -th mode. If we define the matrix of the coefficients  $Q$ , which contains all the scalar coefficients  $q^{(i,j)}$ , and the modes matrix  $M$ , whose columns correspond to the basis vectors,

we can express the same relation using the aforementioned matrix  $A$ :

$$A = QM^T \quad (5.3)$$

The POD modes are extracted by computing the Single Value Decomposition (SVD) of the matrix  $A$ , which is of the form:

$$A = U\Sigma V^T \quad (5.4)$$

where  $U$  is an  $N \times N$  orthogonal matrix,  $V$  is an  $m \times m$  orthogonal matrix and  $\Sigma$  is an  $N \times m$  matrix whose diagonal elements  $\lambda_i = \Sigma_{ii}$ , called singular values, are the only non-zero values. Furthermore, these entries are non negative and arranged in decreasing order. By letting  $U\Sigma = P$  we obtain:

$$A = PV^T \quad (5.5)$$

which is equivalent to Eq. 5.3. The only difference is that the columns of  $V$  are orthogonal but not orthonormal, and therefore they need to be normalized to obtain the POD modes.

The crucial property of the SVD, and thus of the POD, is that it provides an optimal  $k$ -rank approximation of the original matrix, for any  $k < m$ , in the least squares sense. In fact, if we define  $\Sigma_l$  by setting  $\Sigma_{ii} = 0$  for  $i > k$  in  $\Sigma$ , we obtain a  $k$ -rank optimal approximation of  $A$  defined as:

$$A_k = U\Sigma_k V^T \quad (5.6)$$

such that  $A_k$ , among all the matrix with rank  $k$ , minimizes the distance from  $A$  in the Frobenius norm  $\|A - A_k\|$ . The Frobenius norm of a matrix is defined as the square root of the sum of squares of all the elements.

Approximating  $A$  with a  $A_k$  means using only the first  $k$  modes to reconstruct the matrix. In the case of velocity measurements, the Frobenius norm of the matrix  $A$  is strictly related to the total kinetic energy. Hence,  $A_k$  is a reconstruction of all the measured fields using the  $k$  most energetic modes. In fact, the singular values  $\lambda_i$  are arranged in a decreasing order and are related to the energy contained in each mode such that:

$$\frac{KE_i}{KE_{tot}} = \frac{\lambda_i}{\sum_{j=1}^m \lambda_j} \quad (5.7)$$

where  $KE_i$  is the energy contained in the  $i$ -th mode, and  $KE_{tot}$  is the total kinetic energy. The most energetic modes represent the most energetic and/or frequent flow structures that appear among the different measurement sets (*i.e.* engine cycles), even though they should not be considered as real physical structures. In fact, in most of the real, irregular cases, each mode represents an overlapping of actual physical structures (Chen *et al.* 20012). An interesting analysis about the relation between POD modes and physical structures using artificially-generated velocity fields is carried out in Régert *et al.* (2005).

Computing the SVD of the  $N \times m$  matrix  $A$  requires the solution of the following eigenvalue problem:

$$C\mathbf{v}_i = \lambda_i \mathbf{v}_i \quad (5.8)$$

where  $C = A^T A$ , which is an  $m \times m$  square matrix. The number of computational steps needed grows markedly with  $m$ , and since in our case  $m$  is a multiple of the number of vectors per velocity fields (depending on the components considered), the solution would not be feasible. To overcome such computational issue, a new POD algorithm, the so-called Snapshot POD, was introduced by Sirovich (1987). It solves instead the eigenvalue problem for a  $N \times N$  matrix, leading to a drastic decrease in the computational time if the number of measurement sets is much lower than the values measured.

Classical POD allows for the decomposition of a set of measurements in modes containing a specified amount of energy. Therefore it can be used as a filter: by considering only a small number of modes in the reconstruction of a velocity fields, one can highlight the most energetic structures and filter out noise, turbulence and less energetic coherent structures. Furthermore, the regularity of the flow can be estimated by the modes energy spectrum: the higher the energy contained within the first modes, the less modes are needed to reconstruct the velocity fields and hence the more organized is the flow. However, when dealing with unsteady flows in a time-dependent domain, as in-cylinder flows, the so called phase-dependent POD does not consider the time evolution of the flow. In fact, it only allows for the optimal reconstruction of the flow fields measured at a single crank-angle, or phase, at a time. Consequently, the modes depend on the instant during the stroke they have been computed for.

Phase-invariant POD, instead, allows the inspection of the time-evolution of unsteady flows, providing a single set of modes capable of describing, by a linear combination with scalar coefficients depending both on the time instant and on the cycle considered, the time evolution of the flow realizations during the stroke. This method, introduced by Fogleman *et al.* (2004), uses the SVD approach as well. However, the matrix  $A$  now contains all the velocity fields measured. If we assume we have measured the velocity fields at  $t$  time instants during each cycle,  $A$  becomes a  $Nt \times m$  matrix (or  $m \times Nt$  since Snapshot POD is used in most of the cases).

To be consistent, each velocity field in  $A$  must have the same number of vectors, even though the number of measured vectors depends on the spatial domain of the flow, which is determined by the piston location. Therefore, all the velocity fields have to be adapted to a common grid, which is usually the vectors grid limited by the piston at the middle of the stroke. All the velocity fields measured in the first half of the stroke are stretched into the new grid, whereas the ones measured in the second half are compressed into the common

grid. Eventually, a cubic interpolation scheme is utilized to properly fit all the fields into the grid due to its minimum influence on the kinetic energy (Moreau *et al.* 2005). The next step is to normalize each velocity field by the square root of its energy, in order to weight equally the phase of the flow which have less total energy with the higher-energetic phases when extracting flow structures. Snapshot POD is then applied to the velocity fields, and the modes are computed and normalized. By projecting the non-normalized velocity fields onto the orthonormal basis, the coefficients for each velocity field are obtained. Due to the orthonormality of the basis, the ratio between the square of the  $i$ -th mode coefficient and the sum of the squares of all the coefficients represents the contribution of the  $i$ -th mode to the total energy of the velocity field.

However, some authors (Fogleman *et al.* 2004; Druault *et al.* 2005) proposed an extra intermediate step in the phase-invariant POD algorithm. When adapting all the velocity fields to the new common grid, they also modify the velocity component in the direction of the transformation in order to preserve the divergence of the field:

$$v_{fix}(\mathbf{x}) = \frac{l_{fix}}{l_{og}} v_{og}(\mathbf{x}) \quad (5.9)$$

where  $v_{fix}(\mathbf{x})$  and  $v_{og}(\mathbf{x})$  are the velocity components in the direction of the stretching/compression, in the new common grid and in the original one respectively. Instead,  $l_{fix}$  and  $l_{og}$  are the length of the two grids. By doing so, they affect the energy content of the velocity fields, even though they observed no effects on the shape of the first modes and their eigenvalues distribution. On the other hand, this approach does not allow for an accurate description of the kinetic energy distribution among the modes by the use of scalar coefficients. Such coefficients, in fact, are relative to the modes as considered in the fixed grid. To move back to the original grid of each velocity field, the modes have to be stretched/compressed. Therefore they lose their orthonormality, the property which makes it possible to use the squares of the coefficients to describe the kinetic energy distribution.

Phase-invariant POD enables the extraction of an unique set of modes, independent on the specific time instant during the stroke, and thus provides an unique way to describe the time evolution of each cycle using scalar coefficients. By the analysis of such coefficients one can study the behaviour of the flow, and how the relative energetic contribution of each mode evolves throughout the stroke for each cycle. Furthermore, comparing the distribution of the coefficients among the different cycles, a time-resolved evaluation of the cyclic variability can be carried out.

### 5.3.2. *Three-dimensional reconstruction*

The main purpose of performing Stereo PIV measurement in differently oriented tumble planes is the three-dimensional reconstruction of the ensemble

averaged properties of the flow. Once these quantities, such as the mean velocity fields and the turbulent kinetic energy (see subsection 2.2.4), have been evaluated, it is possible to reconstruct the equivalent three-dimensional fields by adapting the averaged fields into a three-dimensional frame of reference and by interpolating them over the cylinder volume. To do so, the frame of reference shown in Fig. 5.8 was used.

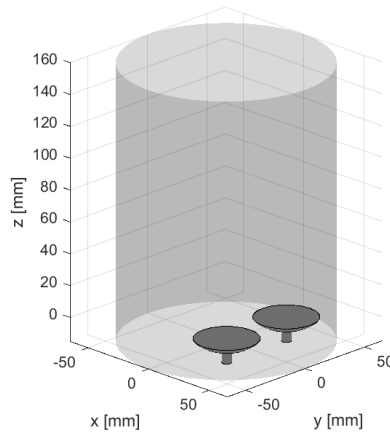


FIGURE 5.8. The frame of reference used for the reconstruction of the three-dimensional averaged fields. The  $z$ -axis coincides with the cylinder axis.

As can be noticed, the  $z$ -axis is set to coincide with the cylinder-axis, whereas in the planar data the cylinder axis is superposed to the  $y$ -axis. Similarly to the planar frame, the zero of the vertical axis is located 15 mm away from the cylinder deck, at the position kept by the valves in the fixed case, since the PIV data in these first 15 mm are neither reliable nor available in every plane. Anyway, the coordinate transformation between the planar and the three-dimensional frame of reference is the following:

$$\begin{cases} x_3 = x_p \cos(-\Theta_p) \\ y_3 = x_p \sin(-\Theta_p) \\ z_3 = y_p \end{cases} \quad (5.10)$$

where  $(x_3, y_3, z_3)$  are the coordinates in the three-dimensional frame of reference (Fig. 5.8),  $(x_p, y_p)$  are the coordinates in the two-dimensional frame of reference of the vertical plane (Fig. 5.7) and  $\Theta_p$  is the angular position of the vertical plane (Fig. 5.5). The components of the velocity fields in the planar frame of

reference are instead transformed into the three-dimensional frame as follows:

$$\begin{cases} u_3 = u_p \cos(-\Theta_p) + w_p \sin(-\Theta_p) \\ v_3 = u_p \sin(-\Theta_p) - w_p \cos(-\Theta_p) \\ w_3 = v_p \end{cases} \quad (5.11)$$

where  $(u_3, v_3, w_3)$  and  $(u_p, v_p, w_p)$  are the components of the velocity vector in the three-dimensional and planar frame of reference respectively.

With the averaged velocity fields adapted into the three-dimensional frame of reference for each time instant, the linear interpolation of each component was performed in order to reconstruct the fields within the entire cylinder volume. The same procedure was carried out with the TKE scalar field, allowing for a complete three-dimensional and time-resolved analysis of the averaged fields.

### 5.3.3. Vortex Tracking

For a detailed analysis of the swirl motion in the three-dimensional flow, a vortex tracking algorithm was used to assess the position of the swirl center in each horizontal plane and to study the organization of the swirling pattern at different heights. The algorithm employed is described in Graftieaux *et al.* (2001), and features the evaluation of the tangential velocity distribution around each point of the plane. The aim is to find the in-plane maximum value of the function  $\Gamma$  defined as:

$$\Gamma(\mathbf{P}) = \frac{1}{S} \int_{M \in S} \frac{(\mathbf{PM} \times \mathbf{U}_M) \cdot \hat{\mathbf{k}}}{\|\mathbf{PM}\| \cdot \|\mathbf{U}_M\|} dS = \frac{1}{S} \int_S \sin(\theta_M) dS \quad (5.12)$$

where  $\mathbf{P}$  is a fixed point in the plane,  $S$  is a two-dimensional area surrounding  $\mathbf{P}$ ,  $\theta_M$  represents the angle between the velocity vector  $\mathbf{U}_M$  and the radius vector  $\mathbf{PM}$  and  $\hat{\mathbf{k}}$  is the unit vector in the direction normal to the plane. Consequently,  $\Gamma$  is a dimensionless scalar with  $|\Gamma|$  bounded by 1.

By finding the maximum planar value of  $|\Gamma|$  and the respective position, it is possible to find the location of the vortex center in the plane considered. Furthermore, by evaluating the actual sign of this value and its magnitude, one can assess the direction of the vortex and its organization. The higher the magnitude of  $|\Gamma|$ , the more organized is the vortical motion around its center. In fact, its maximum possible value is reached by a velocity field with no radial component and all the velocity vectors following the same direction of rotation.

The algorithm implemented computes the function  $\Gamma$  in its discrete form:

$$\Gamma(\mathbf{P}) = \frac{1}{N} \sum_S \frac{(\mathbf{PM} \times \mathbf{U}_M) \cdot \hat{\mathbf{k}}}{\|\mathbf{PM}\| \cdot \|\mathbf{U}_M\|} = \frac{1}{N} \sum_S \sin(\theta_M) \quad (5.13)$$

where  $N$  is the number of points contained in  $S$ . In our case,  $\hat{\mathbf{k}}$  is the unity vector in the  $z$  direction and  $S$  is a two-dimensional area in the horizontal plane.

Since the expected length scale of the swirling vortex is comparable with the diameter of the cylinder,  $S$  can be considered as the area of the horizontal plane limited by the cylinder walls. By maximizing this function it is then possible to evaluate the swirl center, the direction of the rotation and most importantly the organization of the swirl pattern.



## CHAPTER 6

### Results and discussion

In the current chapter, the results of this study are presented and discussed. A description of the dynamics of the flow is given, considering both planar and three-dimensional reconstructed velocity fields. An evaluation of cyclic variability, as well as a detailed assessment of the three-dimensional averaged flow, is presented. Eventually, the outcomes of a comparison between SPIV and RANS CFD data are introduced and discussed.

#### **6.1. Intake flow overview: planar data**

Within the next subsections, an overview of the flow behaviour is given by presenting and describing two-dimensional two-component velocity fields at different time instants during the intake stroke. The main features of the evolving flow, along with the differences between instantaneous and ensemble-averaged velocity fields, are identified and discussed. For these purposes, the two most significant and representative planes are taken into consideration, for both the moving and the fixed valves cases. In fact, the planar velocities fields in the  $0^\circ$  and  $90^\circ$  plane (see Fig. 5.5) are shown and analysed to highlight general information about typical flow structures and their time evolution.

##### **6.1.1. Averaged velocity fields**

An effective way to study the features of the intake flow and the rise of typical large-scale structures is to consider ensemble-averaged velocity fields. An ensemble average is defined as the average over a certain number of flow realizations (Eq. 2.23). For the study of in-cylinder flows, this average is therefore taken over the number of engine cycles inspected. This approach allows to extract the main structures of the flow and its frequent features, and to filter out measurement errors, small cyclic variations and turbulent effects affecting single cycles. Moreover, the three-dimensional reconstruction is only possible for averaged velocity fields, since single cycle measurements in different planes can not be correlated. Also the comparison with RANS CFD data is only possible using average velocity fields, due to the averaged nature of RANS equations.

In Fig. 6.1 and Fig. 6.2, the time evolution of the averaged velocity field in the  $90^\circ$  plane is shown for the fixed and moving valves case respectively. To compute the ensemble average, all the cycles inspected were considered.

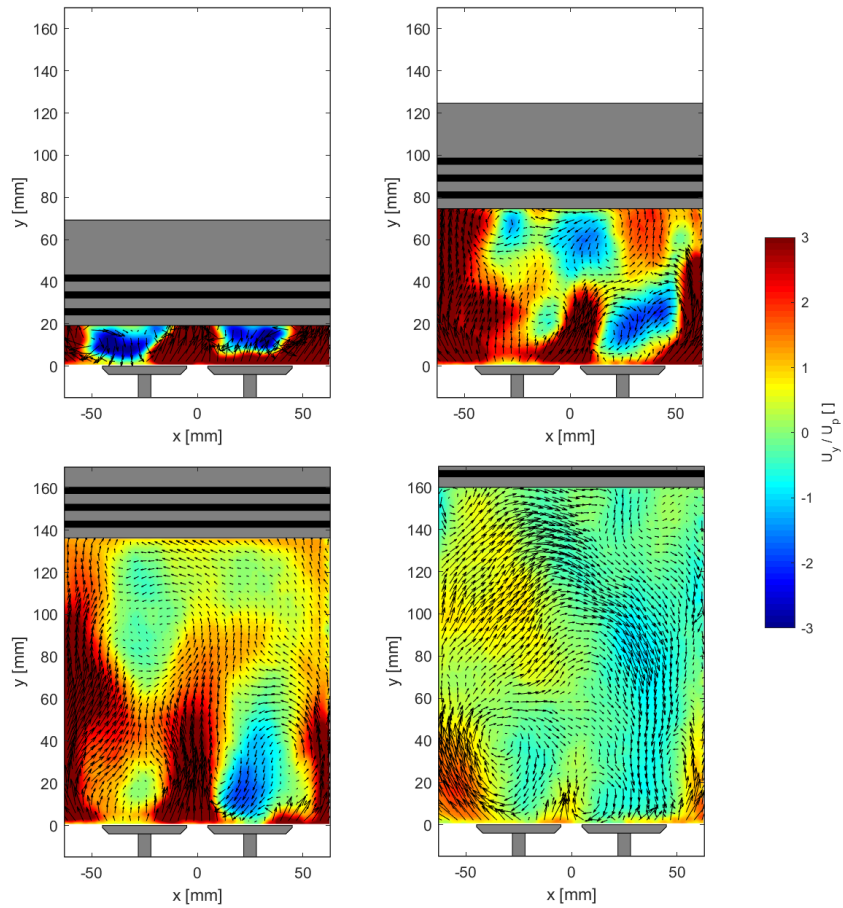


FIGURE 6.1. Averaged two-dimensional velocity fields in the  $90^\circ$  plane for the fixed valves case, at 0.3, 0.5, 0.75 and 1 s from the beginning of the intake stroke (left-to-right, top-to-bottom respectively). One vector of every four is plotted, and the vertical velocity component normalized by the mean piston speed is colour-coded. Vectors length is scaled with respect to the highest-magnitude vector for each field.

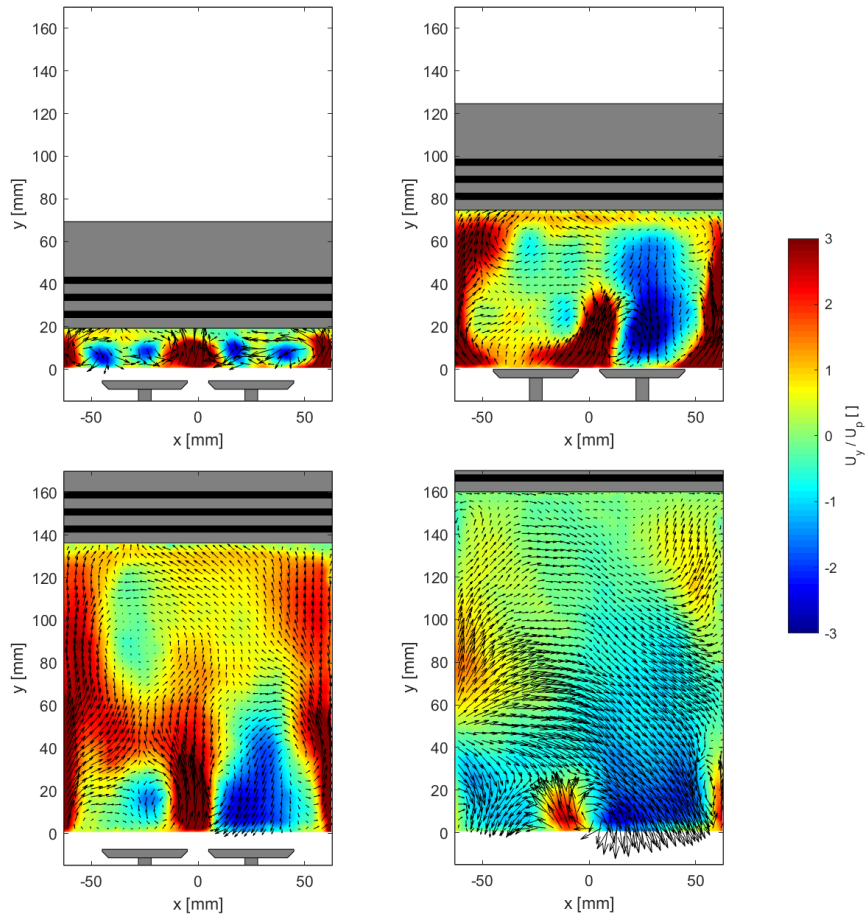


FIGURE 6.2. Averaged two-dimensional velocity fields in the  $90^\circ$  plane for the moving valves case, at 0.3, 0.5, 0.75 and 1 s from the beginning of the intake stroke (left-to-right, top-to-bottom respectively). One vector of every four is plotted, and the vertical velocity component normalized by the mean piston speed is colour-coded. Vectors length is scaled with respect to the highest-magnitude vector for each field.

As one would expect, the dynamics of the flow during most part of the stroke is dominated by the intake jet entering the cylinder from the inlet port. Although the same mass flow and the different valve curtain area between the moving and the fixed valves case should result in higher velocities in the former case, no big differences in the vertical component (and in the velocity magnitude) can be noticed throughout the stroke. This might be related to the lack of velocity data in the first 15 mm of the cylinder, where the two cases might feature some noticeable differences because of the aforementioned reason. The interaction of the jet with the valves causes the generation of a recirculation bubble above each valve as soon as the mass flow starts to get into the cylinder. Towards the end of the stroke, the overall symmetry of the flow is broken by the jet interactions with cylinder walls and the piston, resulting in a tumbling motion that appears to be slightly stronger, yet less organized, in the moving valves case.

Fig. 6.3 and Fig. 6.4, instead, show the time evolution of the intake flow in the  $0^\circ$  plane for the fixed and moving valves case respectively. Whereas for the former case all the cycles inspected were considered when averaging, for the latter some cycles were removed from the ensemble, as explained in 6.2.3. The flow is again dominated by the intake jet, even though it lacks symmetry because of the relative position of the valves. This flow asymmetry results in a stronger in-plane tumble at the end of the stroke. In fact, the recirculation bubble generated by the valve-jet interaction grows bigger and becomes a vortex as soon as the jet hits the wall. Eventually, when the jet gets deflected by both the wall and the piston, the vortex evolves in an overall tumbling motion, which is significantly clearer in the fixed valves case. In the moving case, a higher-velocity zone probably caused by the lower valve lifts is still present at the end of the stroke, opposing the generation of an organized tumble motion.

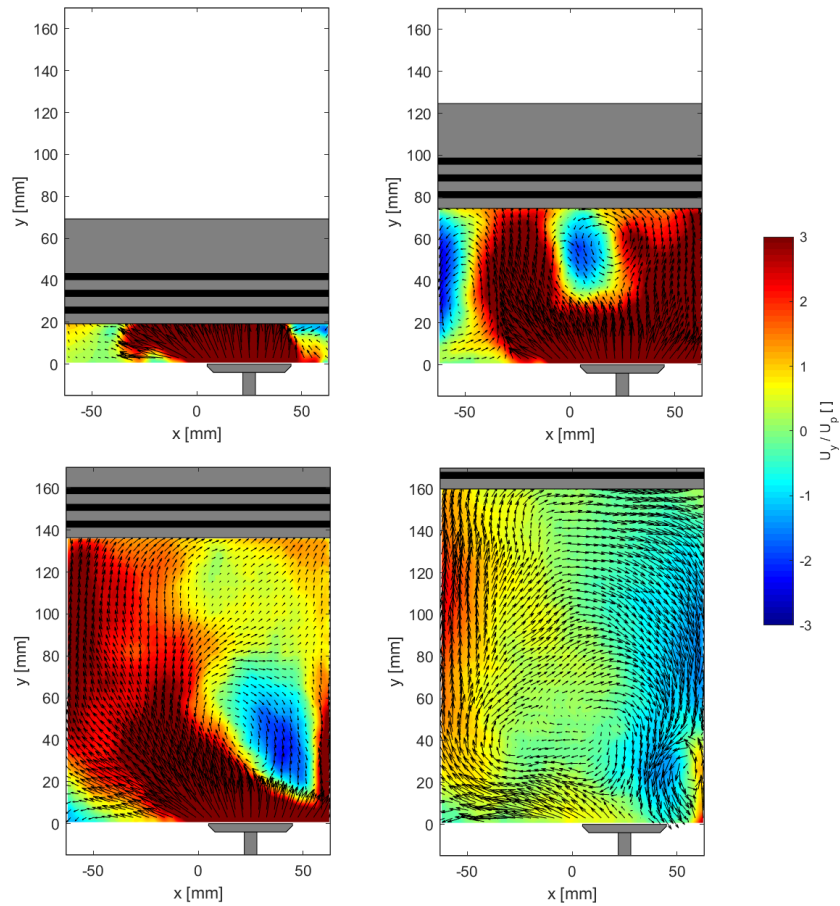


FIGURE 6.3. Averaged two-dimensional velocity fields in the  $0^\circ$  plane for the fixed valves case, at 0.3, 0.5, 0.75 and 1 s from the beginning of the intake stroke (left-to-right, top-to-bottom respectively). One vector of every four is plotted, and the vertical velocity component normalized by the mean piston speed is colour-coded. Vectors length is scaled with respect to the highest-magnitude vector for each field.

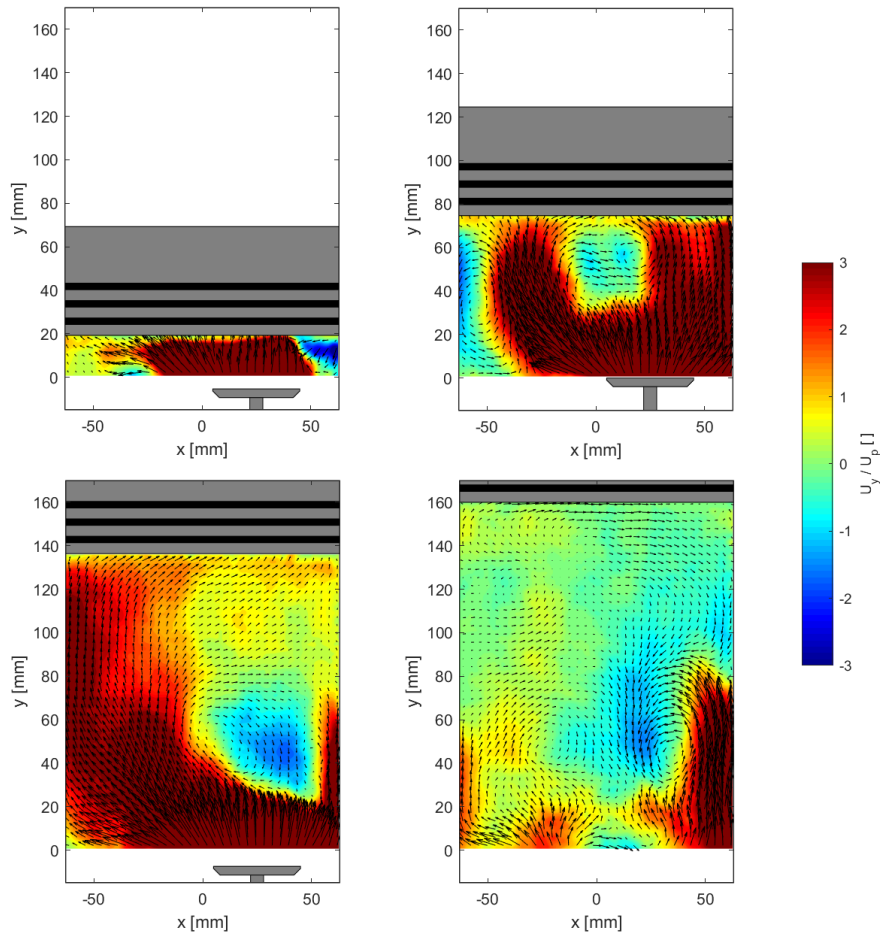


FIGURE 6.4. Averaged two-dimensional velocity fields in the  $0^\circ$  plane for the moving valves case, at 0.3, 0.5, 0.75 and 1 s from the beginning of the intake stroke (left-to-right, top-to-bottom respectively). One vector of every four is plotted, and the vertical velocity component normalized by the mean piston speed is colour-coded. Vectors length is scaled with respect to the highest-magnitude vector for each field.

### 6.1.2. Instantaneous velocity fields

Although averaged velocity fields are an useful tool to identify and describe the main features of the flow and to extract important information and flow parameters, they do not represent the physical reality. No averaged cycle occurs in an engine, and turbulent variations along with major cyclic variations affect each cycle making it different from the others. The analysis of instantaneous velocity field is then necessary to detect possible large fluctuations in the flow structures, which might be misleading for the interpretation of the averaged flow, as shown in section 6.2, and for the prediction of engine performances. However, most of the times instantaneous fields present only minor variations caused by turbulence. Such variations do not affect markedly the larger structures of the flow, and therefore the analysis of the averaged flow is usually sufficient to obtain a good estimation of the flow dynamics.

Nevertheless, it is interesting to see the differences between instantaneous and ensemble averaged velocity fields. Fig. 6.5 compares two instantaneous velocity fields from different cycles and the ensemble average flow at the same time instant. Even though the main flow structures highlighted by the averaged velocity field, such as the quasi-symmetric jet and the recirculation bubbles, are present in both the instantaneous fields, small variations can be noticed especially in the left part of the plane. Such variability is mostly caused by the strong turbulent nature of the flow, even if larger-scales cyclic variations provoked by high sensitivity to inlet conditions and other factors might occur as well.

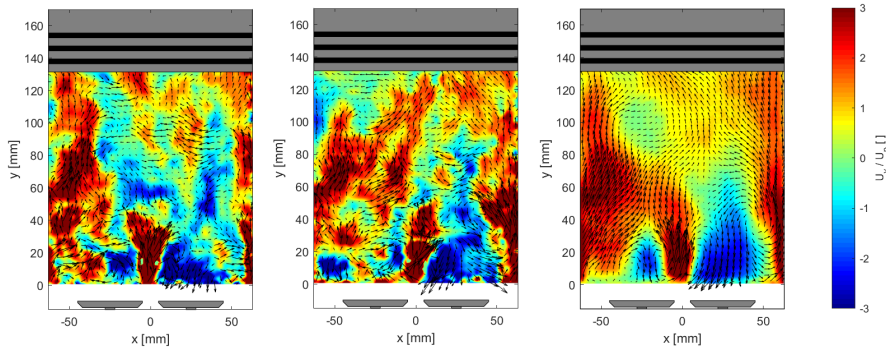


FIGURE 6.5. Instantaneous and averaged two-dimensional velocity fields in the  $90^\circ$  plane for the moving valves case, at 0.8 s from the beginning of the intake stroke. One vector of every four is plotted, and the vertical velocity component normalized by the mean piston speed is colour-coded. Vectors length is scaled with respect to the highest-magnitude vector for each field.

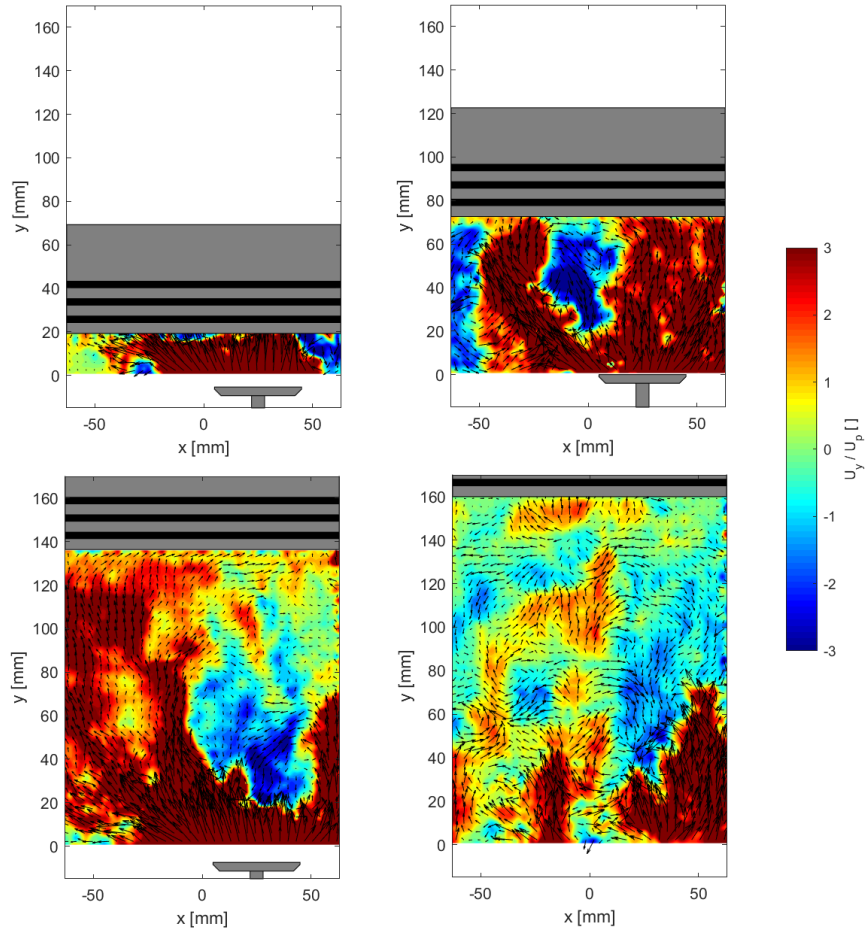


FIGURE 6.6. Instantaneous two-dimensional velocity fields from the same cycle in the  $0^\circ$  plane for the moving valves case, at 0.3, 0.5, 0.75 and 1 s from the beginning of the intake stroke (left-to-right, top-to-bottom respectively). One vector of every four is plotted, and the vertical velocity component normalized by the mean piston speed is colour-coded. Vectors length is scaled with respect to the highest-magnitude vector for each field.

Fig. 6.5, instead, shows the time evolution of the flow during a single cycle by representing instantaneous velocity fields at different time instants during the stroke. If we compare it with the corresponding ensemble averaged flow shown in Fig. 6.4, we can notice the same overall flow behaviour throughout the stroke. On the other hand, this comparison underlines the filtering action of the averaging operation. As it happens also in Fig. 6.5, the mean flow field is significantly smoother and more organized than the instantaneous one, and the flow main structures are easier to distinguish from the general flow pattern.

## 6.2. Cycle-to-cycle variations: a POD analysis

Before computing ensemble-averaged planar velocity fields and proceeding to the three-dimensional reconstruction of the mean flow, a phase-invariant POD analysis of the 50 Hz data was carried out to detect unusual cyclic variability among the ensembles of instantaneous velocity fields. This mode decomposition makes it easier to find out major cyclic variations in large-scale flow structures by evaluating the distribution and the time evolution of the coefficients relative to the most energetic modes.

For each inspected plane, the phase-invariant algorithm described in subsection 5.3.1 was applied to the planar components of the instantaneous velocity fields. Time instants between 0 and 0.3 s were not considered due to the presence of high levels of noise. Dealing with two-component velocity fields, instead of considering all three components, allows for a decrease of the computational time needed without affecting the capability to detect cycle-to-cycle variations. In fact, it is believed that major cyclic variations affect simultaneously all the components of the velocity fields, and there is no separation between in-plane and out-of-plane components cyclic variability. In this sense, neglecting the third component in the analysis does not influence the outcomes and makes the visualization of the results easier and more intuitive.

Interesting results were found in two of the planes inspected, and only in the moving valves case. The outcomes of this evaluation for the two aforementioned planes are presented within the next subsections.

### 6.2.1. *Cyclic variability in the 0° plane*

Some unexpected cyclic variations in the jet behaviour were found when analysing the instantaneous velocity fields in the 0° plane for the moving valves case. The first three POD modes with the respective time coefficients were taken into account for this evaluation. In fact, a threshold on the fraction of the total kinetic energy contained in each mode had been set to 5% in order to consider only high-energy, frequent structures in the flow. As can be seen in Fig. 6.7, the first three modes account collectively for around 56% of the total kinetic energy contained in the ensemble of the normalized instantaneous fields adapted to the intermediate grid (see subsection 5.3.1). A marked decrease in the energy content of the subsequent modes can be noticed as well.

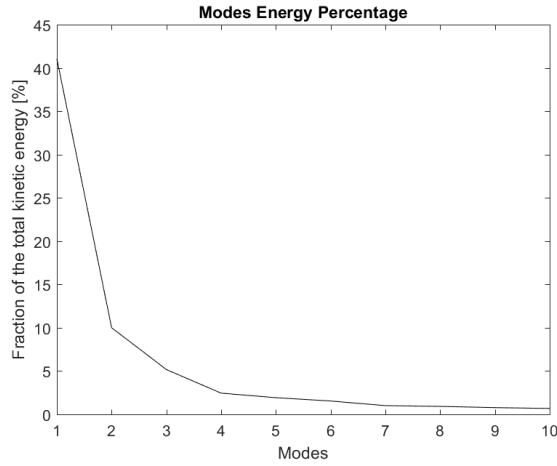


FIGURE 6.7. Energy content of the first ten phase-invariant POD modes in the  $0^\circ$  plane for the moving valves case.

The first three modes are shown in Fig. 6.8. As expected, the first, most energetic mode contains the intake jet, which is the most energetic flow structure throughout the stroke. The second mode represents the recirculation bubble developing in the second part of the stroke. The third mode, instead, contains the right side jet arising during the last part of the intake .

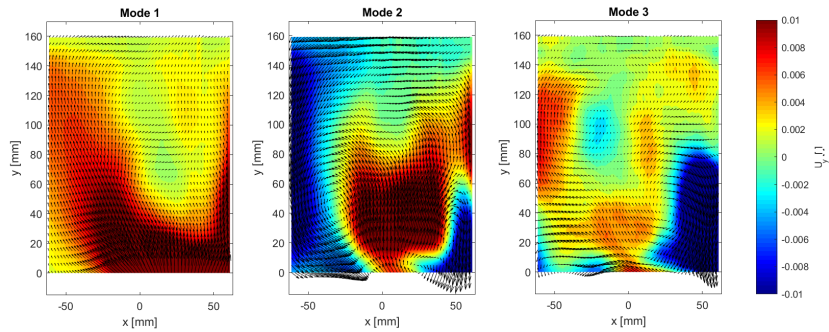


FIGURE 6.8. First three phase-invariant modes in the  $0^\circ$  plane for the moving valves case. One vector of every four is plotted, and the vertical component is colour-coded. Vectors length is scaled with respect to the highest-magnitude vector for each mode. The velocity fields are stretched back to the final time-instant grid.

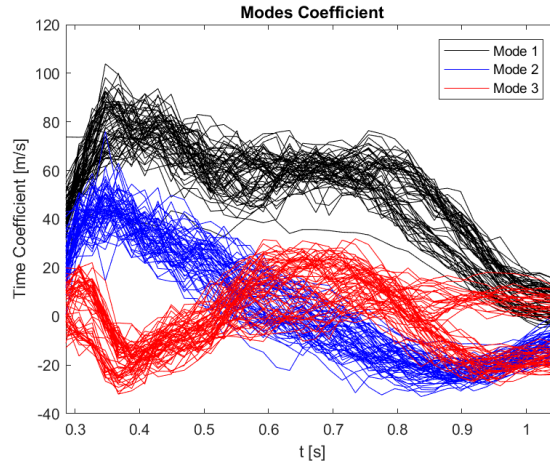


FIGURE 6.9. Time coefficients of the first three phase-invariant POD modes. For each one of the three modes, each line plot represents a single cycle.

To evaluate cyclic variations of these three structures, the time coefficients relative to the first three modes are to be taken into consideration. As can be seen in Fig. 6.9, some major cycle-to-cycle variations are present in the coefficients distribution. Whereas the coefficients of the second mode present a normal distribution, where the differences among the cycle are to be attributed to turbulent fluctuations, the second and third modes present an unusual trend. In particular, by looking at the time coefficients of the third mode in the last part of the stroke, it can be noticed how the cycles are clearly divided in two groups featuring different behaviours. This difference between the two ensembles of cycles is noticeable also in the first part of the stroke and in the distribution of the coefficients relative to the first mode. However, it affects mostly the flow in the final part of the stroke, resulting in significant difference in the late flow pattern.

In fact, as already mentioned, the third mode represents the jet developing during the last part of the stroke in the right side of the plane. Consequently the variations in the third time coefficient highlighted in Fig. 6.10 lead to two different jet behaviours. In the black ensemble of cycles, the value of the coefficient at the end of the stroke is negative and therefore the jet develops normally in the right side. In the red group, the value is around zero and the flow does not feature any strong jet in this position. An intense jet structure develops instead in the left side of the plane. Such cyclic variability can be seen in Fig. 6.11, where the mean fields averaged over the two groups are plotted.

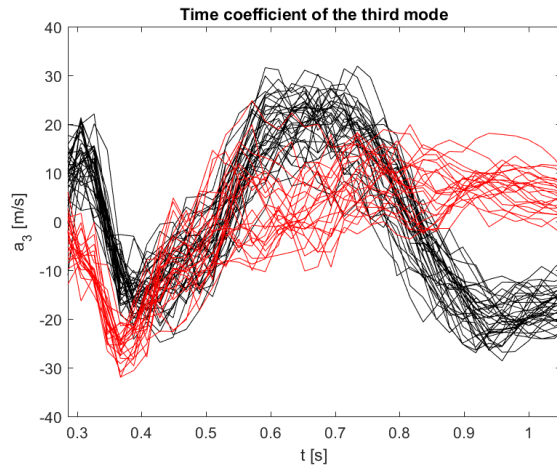


FIGURE 6.10. Time coefficient of the third phase-invariant POD mode.

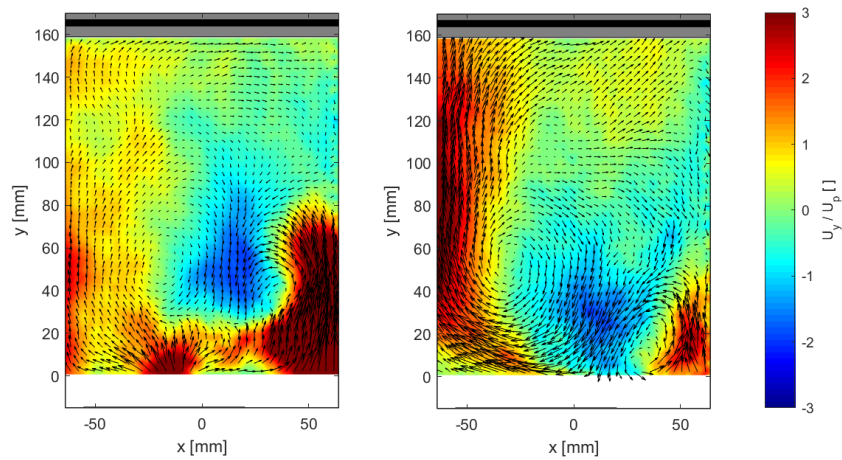


FIGURE 6.11. In-plane velocity fields at  $t = 0.95$  s, averaged over the two ensemble of cycles highlighted in Fig. 6.10. The left field is averaged over the cycles of the black group, whereas the right one is averaged over the cycles of the red ensemble. One vector of every four is plotted, and the vertical component is colour-coded. Vectors length is scaled with respect to the highest-magnitude vector for each field.

### 6.2.2. Cyclic variability in the 135° plane

Similarly, some major cyclic variations were noticed in the 135° plane (see Fig. 5.5), again for the moving valves case. For this planar evaluation, only the first two modes were taken into consideration. In fact, by imposing the same threshold to the relative kinetic energy content of each mode, all the following modes were filtered out. The first two modes account globally for around 47% of the total kinetic energy (Fig. 6.12), whereas the energetic contribution of the subsequent modes falls rapidly to a level negligible for the purpose of the POD analysis.

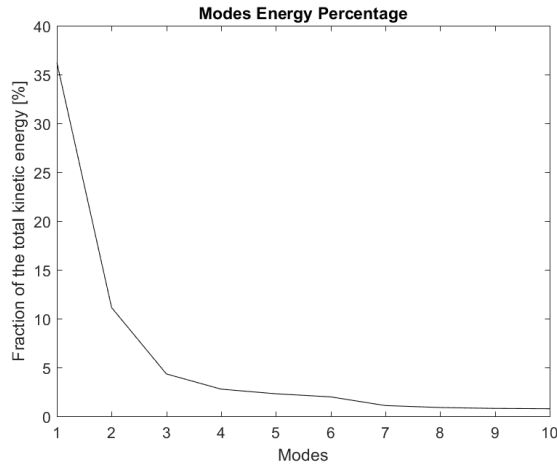


FIGURE 6.12. Energy content of the first ten phase-invariant POD modes in the 135° plane for the moving valves case.

The first two modes, shown in Fig. 6.13, represent the most energetic structures, or an overlapping of them, of the in-plane intake flow measured in the 135° plane. The first mode contains the high-velocity zone developing during the first half of the stroke in the right side of the plane as a consequence of the intake jet entering the cylinder. The second mode, instead, represents the jet arising in the right extremity of the field during the final part of the intake.

The distribution of the time coefficients relative to the first two POD modes (Fig. 6.14) underlines the presence of an unusual cyclic variability in the last part of the intake stroke. Again, the whole ensemble of cycles can be split in two different groups, showing different trends. Such division is particularly noticeable in the distribution of the time coefficient relative to the second mode, whereas the first mode coefficient shows a normal behaviour throughout the stroke.

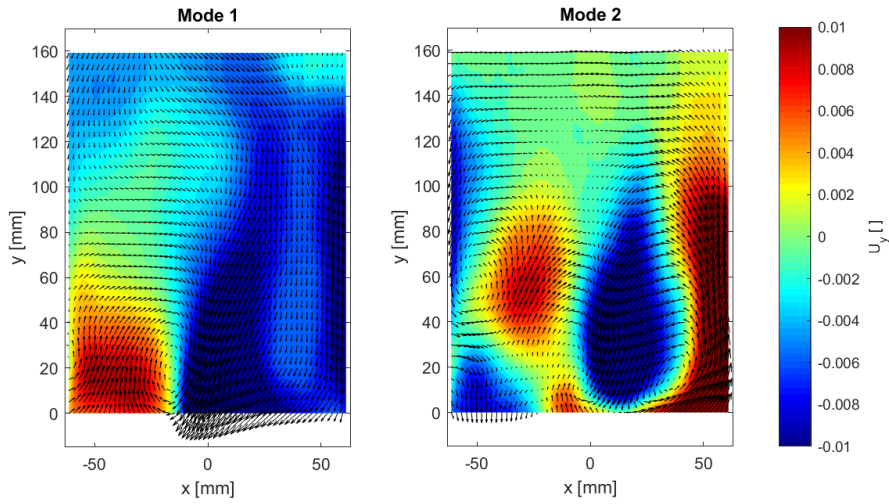


FIGURE 6.13. First two phase-invariant modes in the  $135^\circ$  plane for the moving valves case. One vector of every four is plotted, and the vertical component is colour-coded. Vectors length is scaled with respect to the highest-magnitude vector for each mode. The velocity fields are stretched back to the final time-instant grid.

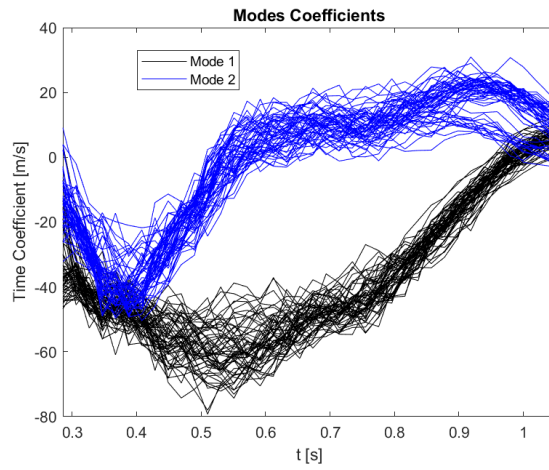


FIGURE 6.14. Time coefficients of the first three phase-invariant POD modes. For each one of the three modes, each line plot represents a single cycle.

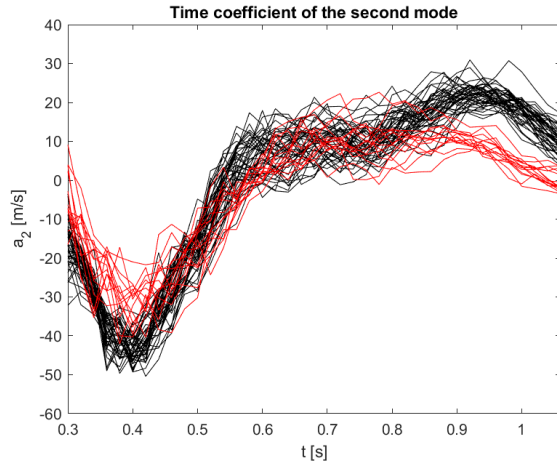


FIGURE 6.15. Time coefficient of the second phase-invariant POD mode.

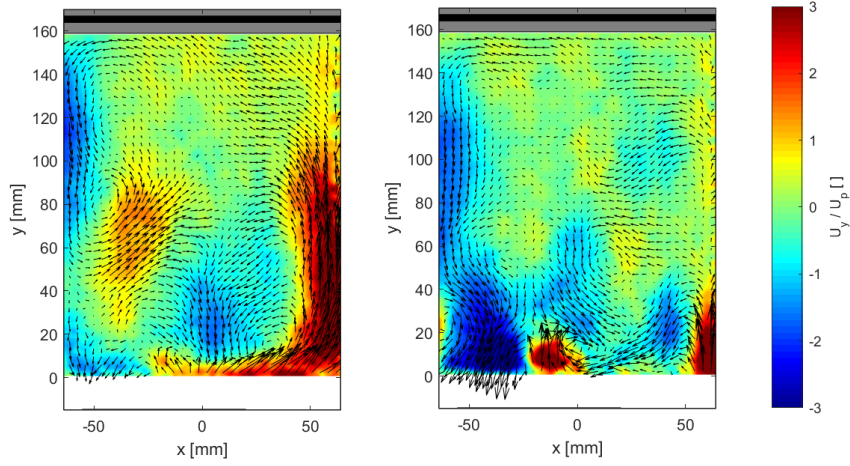


FIGURE 6.16. In-plane velocity fields at  $t = 0.95$  s, averaged over the two ensemble of cycles highlighted in Fig. 6.15. The left field is averaged over the cycles of the black group, whereas the right one is averaged over the cycles of the red ensemble. One vector of every four is plotted, and the vertical component is colour-coded. Vectors length is scaled with respect to the highest-magnitude vector for each field.

The variability in the distribution of the second mode coefficient affects the jet structure in the final part of the stroke. The two ensembles of cycles, highlighted with two different colours in Fig. 6.15, feature two different jet behaviours. As shown in Fig. 6.16, in the black group of cycle, the jet structure in the right side of the plane is still strong at the end of the stroke. In the red ensemble, instead, a significantly weaker structure is present in the same position, whereas a stronger recirculation flow characterizes the left side of the velocity field.

### 6.2.3. *Common features and remarks*

The major cyclic variability found in the two aforementioned planes features some common characteristics, which can be meaningful for the understanding of the underlying phenomena.

First of all, in both the cases each ensemble of similar fields is made of consecutively measured cycles. For the  $0^\circ$  plane, the flow pattern of the black group is the most common among the cycles, since it is featured in the first 36 cycles measured out of 59. Similarly, in the  $135^\circ$  plane the black ensemble behaviour is the most present and appears in the last consecutive 43 cycles inspected out of 57. This trend might be related to a high sensitivity of the port geometry to small perturbations in the boundary conditions. A small fluctuation arisen during the measurements of the two planes might have triggered this sensitivity, causing the splitting of the ensemble of cycles in the two distinct behaviours. In this sense, the absence of a similar cyclic variability in the other planes inspected would be due to the absence of a triggering fluctuation during the respective measurements. Furthermore, a similar situation was found when measuring the swirl ratio generated by the same port in a steady-state flow straightener (Björn Lindgren, Scania, personal communication). A similar splitting trend was observed in consecutive swirl ratio measurements, probably related to some small perturbations in the experimental conditions.

Secondly, the variations regard mostly the jet structure close to the cylinder walls, especially at the end of the stroke. This jet instability might have been amplified by the motion of the valves, since no noticeable variability was found in the fixed valves case. These marked differences in the jet pattern affect the tumble structure at the end of the stroke, which plays an important role in the compression stroke and in the combustion. In this sense, taking into consideration the average over the whole ensemble of cycle might be misleading for the evaluation of the tumble number. Averaging over the entire ensemble of cycles might be misleading for the evaluation of the flow structure as well, since the mean flow would represent an average of two different behaviours. Following this reasoning, only the ensemble of cycles with the most common flow pattern was considered when averaging the instantaneous velocity fields for the  $0^\circ$  and  $135^\circ$  planes. Such an approach was validated by a comparison with the mean flow measured in the adjacent planes.

### 6.3. Intake flow overview: three-dimensional data

Once the aforementioned deviating cycles had been removed from the ensemble, the averaged properties of the flow were computed for each one of the inspected vertical planes and a three-dimensional reconstruction was performed using a linear interpolation scheme. By doing so, the three-dimensional velocity fields along with the volumetric distribution of the turbulent kinetic energy were obtained for each time instant during the intake stroke. The main features of the three-dimensional intake flow, as well as the evolution of its energetic content, are introduced and described in the next subsections. A deeper evaluation of the coherent swirling motion developing throughout the intake stroke in the three-dimensional flow is instead presented in section 6.4.

#### 6.3.1. Averaged velocity fields

The out-of-plane velocity component measured in the different vertical planes is often significantly larger than the in-plane velocity magnitude. Consequently, the three-dimensional averaged intake flow is characterized by the presence of a large azimuthal component, which results in the development of a strong swirling motion.

The evolution of this strong azimuthal flow is generally chaotic during the first part of the stroke, both for the moving and for the fixed valves case. In this time interval, in fact, the three-dimensional flow features high velocities and chaotic structures like counter-rotating and high-gradient zones in the azimuthal component distribution. However, the velocity fields for the fixed valves case are usually more organized than the moving valve case, as shown in the left column in Fig. 6.17. This is probably due to the influence of the valves motion itself, which introduces some instabilities in the development of a coherent rotating flow.

The second part of the stroke, instead, features the rise of a strong, organized swirling motion in most of the cylinder volume. As can be seen in the right column in Fig. 6.17, the two cases inspected show a rather similar behaviour, especially in the higher zones of the cylinder, where the in-plane swirl developed is coherent and comparable to a solid body-like rotation. Again, in the lower zones of the cylinder, the valve motion, as well as the higher azimuthal velocities, might affect the organization and the strength of the rotating motion.

It is then useful to visualize and inspect the flow in its complete three-dimensionality. So far, the components in the vertical planes and the azimuthal one have been considered separately. However, it should be recalled that the intake flow is strongly three-dimensional, and therefore a comparison of the piston-limited vertical motion, whose main feature is the tumbling pattern, and the azimuthal, swirling motion has to be considered for a better understanding of the overall flow structure.

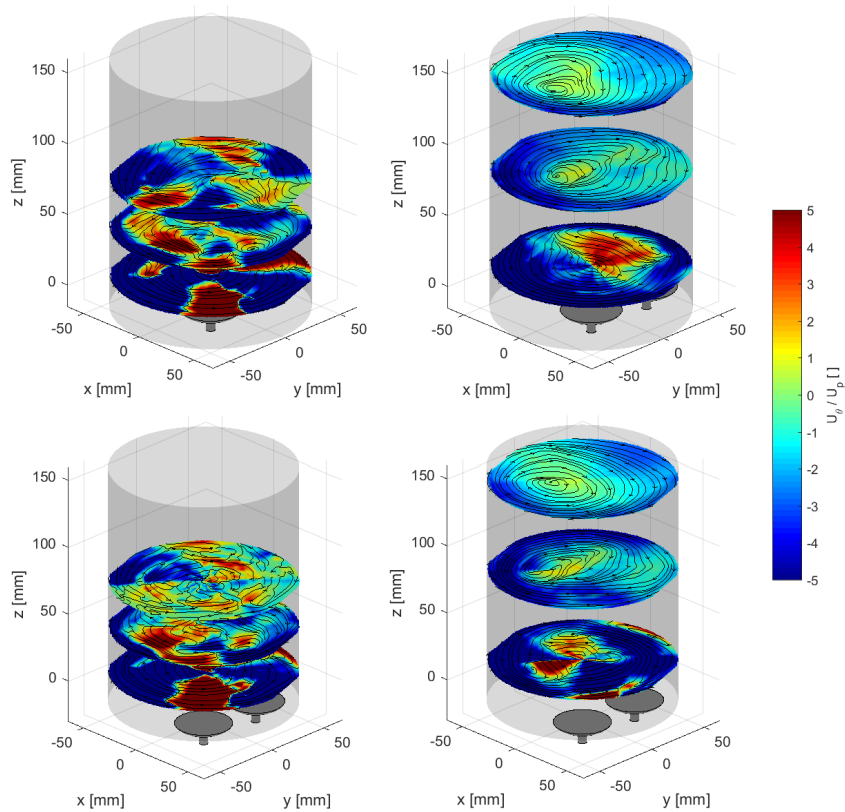


FIGURE 6.17. Three-dimensional reconstructed velocity fields at  $t = 0.5$  s (left column) and  $t = 1$  s (right column) for the fixed (top row) and the moving (bottom row) valves case. In-plane velocity is represented by the streamlines, whereas the azimuthal velocity normalized by the mean piston speed is colour-coded. Three equispaced horizontal planes are shown for each field.

In this sense, Fig. 6.18 show the three-dimensional streamlines at the end of the stroke for the two cases inspected. The velocity field in the final time instant of the intake is particularly important since it represents the initial condition for the subsequent compression stroke. Hence, velocity data measured at the end of the intake stroke can be used, with some simplifications, as initial conditions for numerical simulations of the compression.

Due to the large azimuthal component, the flow presents a predominant swirling behaviour. However, it can be noticed that the rotation does not seem

to take place around the cylinder axis. The axis of rotation seems to be inclined of a tilt angle with respect to the cylinder axis, and this is due to the influence of the vertical tumbling motion. Nevertheless, the similarity with a solid body-like rotation seems to be reasonable, especially in the fixed valves case. In fact, the three-dimensional flow at the end of the intake stroke in the moving valves case appears to be a bit more disorganized than the fixed valves case. This is probably caused by dishomogenities in the vertical and radial components, since the azimuthal flow does not present significant differences when compared to the fixed valves case (Fig. 6.17).

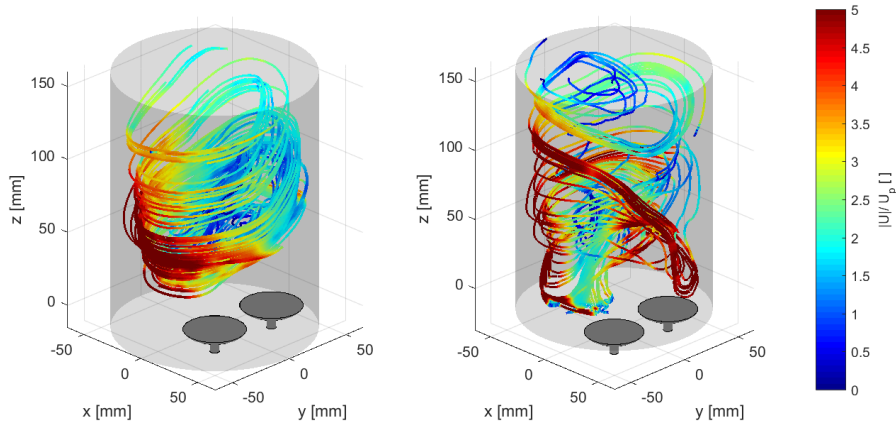


FIGURE 6.18. Three-dimensional reconstructed velocity fields at the end of the stroke ( $t = 1$  s) for the fixed (left) and moving (right) valves case. Streamlines represent the three-component, three-dimensional velocity fields and are colour-coded by the velocity magnitude normalized by the mean piston speed.

### 6.3.2. *Turbulent kinetic energy*

Following the definition given in subsection 2.2.4, the turbulent kinetic energy was evaluated in the different planes inspected and reconstructed in the cylinder volume to gain an insight into the development of turbulence during the intake. However, the first half of the stroke is not considered in this analysis for the lack of reliability of the TKE data computed in this time range. In fact, the small volume measured and thus the larger influence of noisy zones in the piston and cylinder walls proximity, along with some discrepancies in the measured piston position, affect significantly the fluctuations of the velocities measured and therefore the outcomes the turbulent kinetic energy assessment.

Nevertheless, it is interesting to analyse and compare the TKE evolution during the second part of the stroke, as well as its spatial distribution at the end of the intake, between the fixed and the moving valves case. Fig. 6.19 shows the time evolution of the total turbulent kinetic energy retained in the cylinder during the second part of the intake stroke.

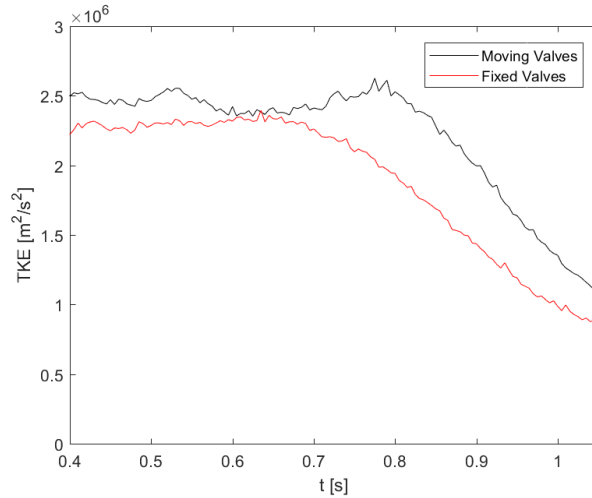


FIGURE 6.19. Evolution of the total turbulent kinetic energy throughout the second part of the stroke. The total value plotted here is defined as the sum of the TKE contributions of each one of the points of the three-dimensional grid.

Turbulent kinetic energy levels are higher at mid-intake, whereas in the final part of the stroke a marked drop is noticeable. As pointed out in Celik *et al.* (2001), this might be due to the decrease of the intake jets momentum in the second part of the intake. Furthermore, the relative difference between the two cases inspected seems to increase in the final part of the stroke in comparison to mid-intake (Fig. 6.20). In particular, the turbulent kinetic energy of the flow in the moving valves case is higher than the fixed valves case towards the end of the stroke. This trend is probably related to the higher velocities in the lower zone of the cylinder caused by the lower valve lift in the moving valves case. In fact, at mid intake, when the valve lift is close to the fixed valve lift, the overall difference is smaller.

Such difference is highlighted in Fig. 6.21, where the three-dimensional spatial distributions of the turbulent kinetic energy are compared at the end of the stroke. In both the cases, the turbulence induced by the jet in the lower part of the cylinder is dominant, but in the moving valves case the high-turbulence region is slightly larger for the aforementioned reason.

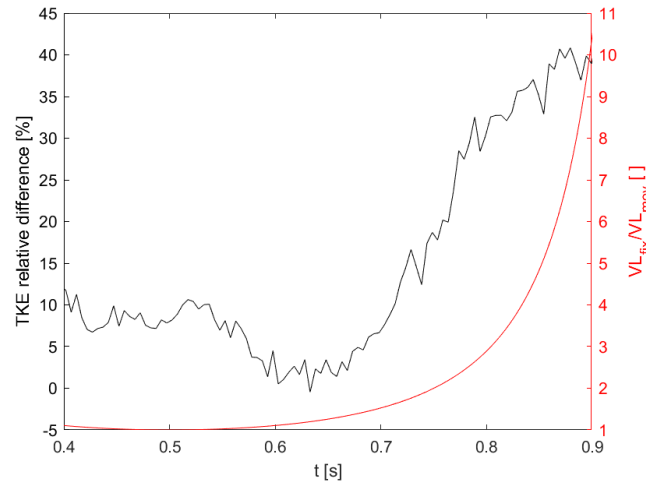


FIGURE 6.20. Relative difference between the TKE in the moving and in the fixed valves case and ratio between the fixed and the moving valves lift in the second part of the stroke.

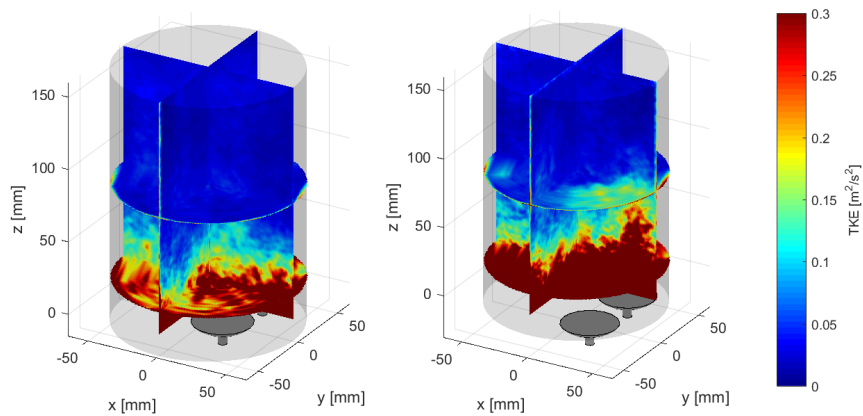


FIGURE 6.21. Three-dimensional distribution of the turbulent kinetic energy at the end of the stroke ( $t = 1$  s) in the fixed (left) and moving (right) valves case. TKE is colour-coded.

### 6.3.3. Kinetic energy

To complete the overview on the three-dimensional flow, the time evolution of the total kinetic energy of the mean velocity fields and the total kinetic energy as defined in subsection 2.2.4 were evaluated. As can be noticed in Fig. 6.22, the kinetic energy of the mean flow shows a behaviour similar to the turbulent kinetic energy, with the high-energy level reached around mid-intake and a marked drop due to viscous dissipation in the final part of the stroke. Generally, the fixed valves case shows higher-kinetic energy values throughout the time range inspected. Considering that the mean kinetic energy of the flow should be the same in the two cases, this trend seems to be in agreement with the opposite behaviour shown in the turbulent kinetic energy evolution. However, in the very last part of the stroke, the fixed valves case features higher values than the moving valves one.

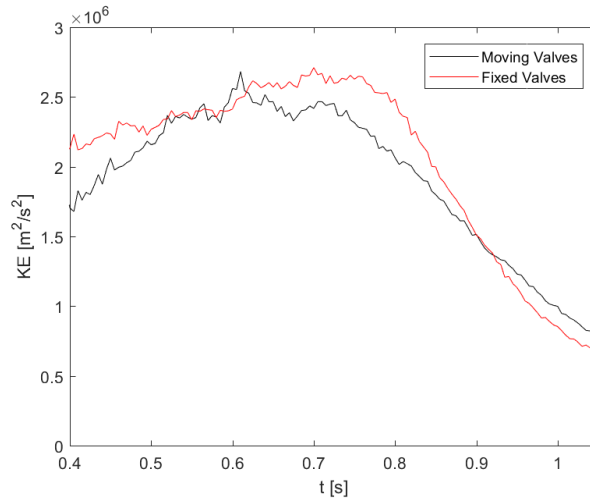


FIGURE 6.22. Evolution of the total kinetic energy of the mean flow throughout the second part of the stroke. The total value plotted here is defined as the sum of the KE contributions of each one of the points of the three-dimensional grid.

The three-dimensional distribution of the kinetic energy during the intake stroke is dominated by the strong swirling component and the jet. As an example, the kinetic energy of the velocity fields at the end of the intake stroke is shown in Fig. 6.23 for the two cases inspected. The highest contribution to the kinetic energy is given by the azimuthal component and therefore by the swirling motion, which features high-energy zones close to the cylinder walls.

The influence of the jet is more significant at lower heights, where the difference between the azimuthal and the vertical component of the velocity is smaller.

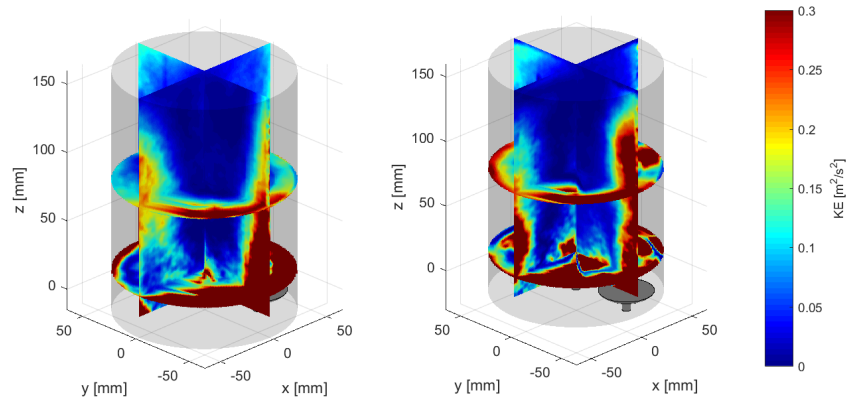


FIGURE 6.23. Three-dimensional distribution of the kinetic energy of the mean flow at the end of the stroke ( $t = 1$  s) in the fixed (left) and moving (right) valves case. KE is colour-coded.

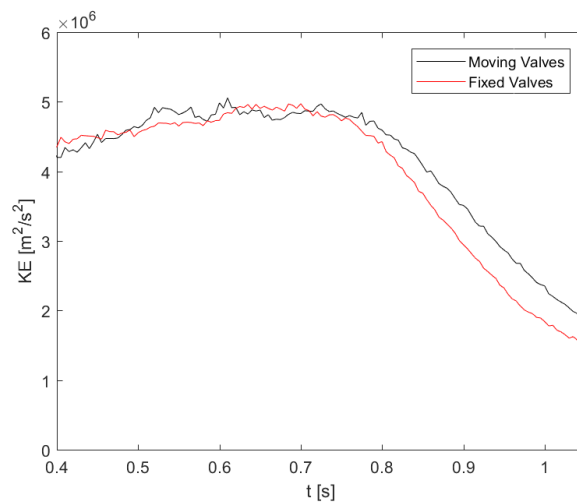


FIGURE 6.24. Evolution of the total mean kinetic energy throughout the second part of the stroke. The total value plotted here is defined as the sum of the KE contributions of each one of the points of the three-dimensional grid.

Finally, the evolution of the mean kinetic energy is plotted in Fig. 6.24. As expected, the two cases studied show quite a similar trend, apart from a noticeable difference in the last part of the stroke. This difference is due to the aforementioned higher values reached by the kinetic energy of the mean flow in the moving valves case at the end of the intake.

## 6.4. A detailed evaluation of the swirling motion

The three-dimensional swirl pattern developing during the intake stroke plays a central role in the mixing processes featured in the combustion of a Diesel engine, and therefore further investigation is needed to assess its strength and organization. Within the next subsections, a quantitative analysis of the swirl in the three-dimensional reconstructed averaged flow is presented, both from a volumetric and from a planar point of view. The fixed and moving valves cases are studied and compared, and the three-dimensional tumbling motion is evaluated as well.

### 6.4.1. Swirl and Tumble numbers

The Swirl and Tumble numbers defined in subsection 3.1.1 were computed for the two cases inspected throughout the intake stroke. Again, being the three-dimensional reconstruction of the averaged fields affected by noise and by fluctuations and uncertainties in the piston position during the first part of the stroke, the outcomes obtained for this time range were not taken into consideration in the analysis. To evaluate  $\Omega_i$  as defined by Eq. 2.31 for each one of the time instants,  $I_{ij}$  and  $L_j$  had to be computed with respect to the center of gravity of the flow. In this sense, the reference frame used to estimate the characteristic angular velocity of the flow depends on the specific time instant. Although the orientation of the three axes is kept fixed (Fig. 5.8), the zero of the  $z$ -axis moves upward in order to follow the center of gravity of the flow, whose motion is provoked by the expansion of the volume considered. By doing so, the  $xy$ -plane is always set to coincide with the mid-height horizontal plane in the cylinder.

The results of this analysis reveal a good matching between the Swirl Number computed for the moving and the fixed valves case (Fig. 6.25). This is in good agreement with the overview of the azimuthal velocity distribution given in subsection 6.3.1, where no big differences in the overall swirl pattern were noticed between the two cases inspected. Usually, the value assumed by the Swirl Number at the end of the stroke ( $t = 1$  s) is the most significant one, and it is utilized as an input for combustion optimization purposes, as well as to define the artificially-generated flow field used to initialize compression simulations. In this case, the Swirl Number assessed at the end of the intake stroke is 3.09 for the moving valves case and 3.16 for the fixed valves one, resulting in a relative difference of around 2% between them.

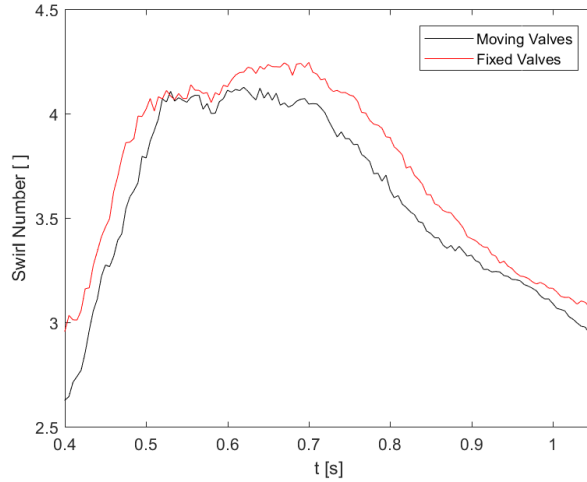


FIGURE 6.25. Evolution of the Swirl Number throughout the second part of the stroke. Note that the actual Swirl Number is negative since the flow rotates clockwise with respect to the  $z$ -axis, and thus the absolute value is taken for ease of visualization.

The evolution of the Tumble Number during the second part of the stroke reveals instead some major differences between the two cases, as can be noticed in Fig. 6.26. These differences characterize mostly the final part of the stroke, where the Tumble Number is significantly lower in the moving valves case with respect to the fixed valves one. Such trend is related to the noticeable differences in the planar averaged velocity fields at the end of the stroke illustrated in subsection 6.1.1. Whereas the averaged azimuthal motion does not show marked discrepancies between the two cases, the planar (vertical and radial) motion seems to be strongly affected by the valve motion towards the end of the stroke. These variations result in different flow patterns and therefore in a different tumbling motion intensity and organization.

Fig. 6.27 compares the relative differences between the two cases inspected in the Swirl and Tumble Number. The two different trends previously mentioned are here underlined. While the relative Swirl Number difference stays below 5% for most of the time range inspected, the relative difference in the Tumble Number reaches values up to 80% in the final part of the stroke. The negligible difference in the values assumed by the Swirl Number is important for future investigations of this parameter. If the main purpose is the inspection of the swirl pattern and its features, future experimental works might neglect the influence of the valve motion on swirl and hence employ simplified setups.

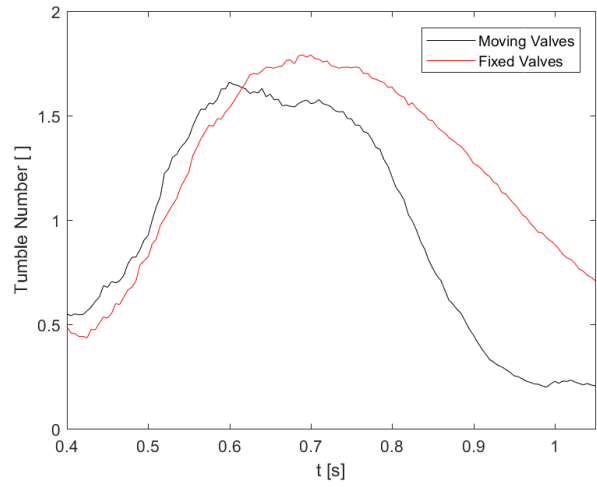


FIGURE 6.26. Evolution of the Tumble Number throughout the second part of the stroke.

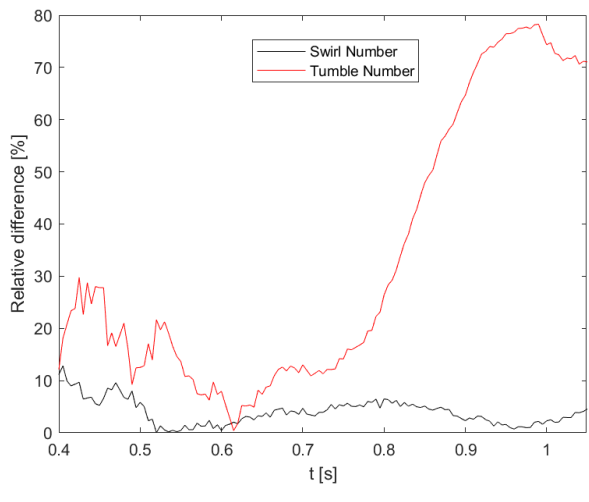


FIGURE 6.27. Relative differences between the moving and the fixed valves case in the Swirl and Tumble Number.

### 6.4.2. Planar swirl analysis

An assessment of the planar swirl motion at different heights in the cylinder is necessary to understand how the organization and the intensity of the swirling pattern vary along the cylinder axis. For these purposes, the Planar Swirl Number, defined in a horizontal plane as the two-dimensional version of the Swirl Number, and the Planar Swirl Organization, defined by maximizing the function  $\Gamma$  (Eq. 5.13) in a horizontal plane, were computed at each height for different time instants. To better understand and visualize the meaning of these two parameters, two sample planar velocity fields are shown in Fig. 6.28. The left one is characterized by a high Planar Swirl Number and a low Planar Swirl Organization, whereas the right one features a low Planar Swirl Number and a high Planar Swirl Organization.

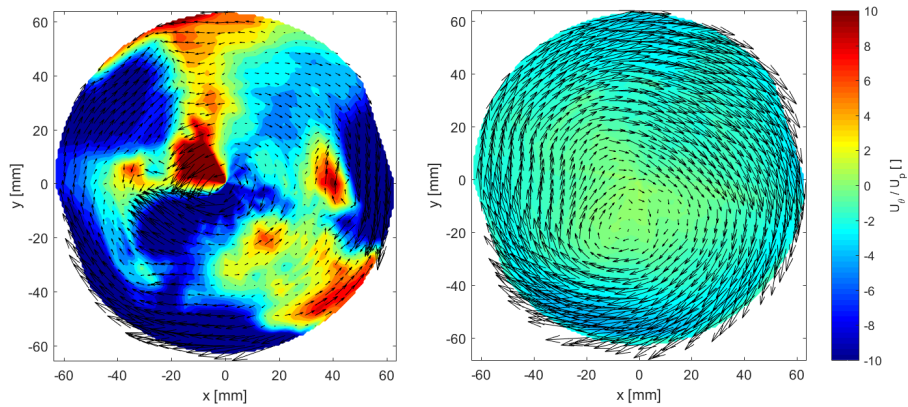


FIGURE 6.28. Comparison of a low-organization, high-intensity swirl pattern (left) with a highly-organized, low-intensity swirling velocity field (right). The azimuthal velocity normalized by the mean piston speed is colour-coded. Vectors length is scaled with respect to the highest-magnitude vector for each field.

Fig. 6.29 and Fig. 6.30, instead, show respectively the distribution of the Planar Swirl Number and the Planar Swirl Organization along the cylinder axis at three different time instants during the second half of the intake stroke. The decreasing trend of the three-dimensional Swirl Number shown in Fig. 6.25 is reflected here in the time evolution of its planar version. In fact, in the first two time instants considered, the high azimuthal velocities in the lower cylinder zones result in high Planar Swirl Number values, whereas at the end of the intake lower values are reached in the same zones due to a decrease in the azimuthal component. Higher zones in the cylinder are instead characterized by

lower Planar Swirl Number values, which present a similar behaviour throughout the time range inspected. Noticeable differences between the moving and the fixed valves case develop during the final part of the stroke. In this time interval, the former case features lower values close to the cylinder deck due to a lack of organization and higher values in intermediate zones caused by slightly higher azimuthal velocities.

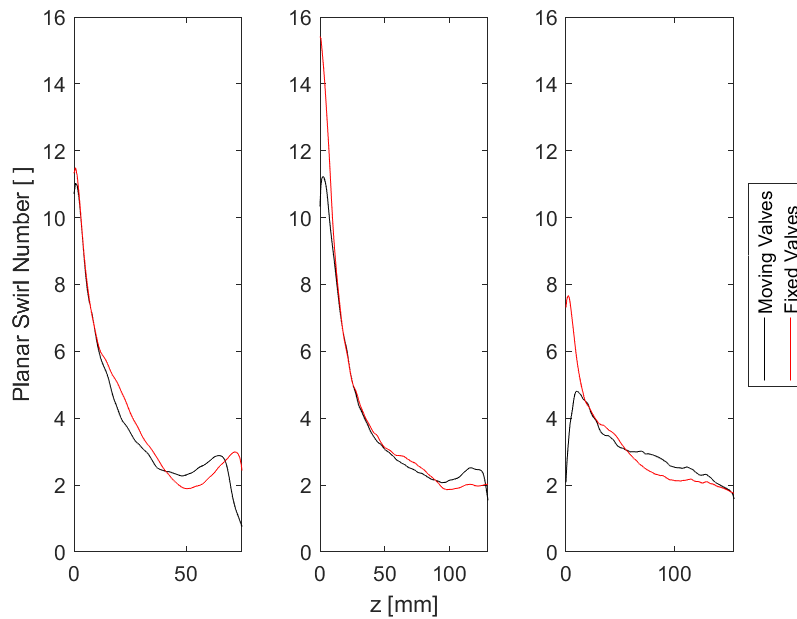


FIGURE 6.29. Planar Swirl Number along the  $z$ -axis for the moving and the fixed valves case at 0.5, 0.75 and 1 s after the beginning of the intake stroke (left-to-right).

The Planar Swirl Organization presents an opposite trend. Starting from lower values at mid-intake, it grows higher throughout the stroke, with a high-organized zone occupying an increasing portion of the cylinder volume. The swirl pattern is generally more chaotic in the lower zones of the cylinder, where marked differences between the two cases inspected can be noticed at the end of the stroke. The fixed valves case, in fact, presents a higher-organized swirling flow in such zones, as already pointed out in subsection 6.3.1. Instead, the high-organized swirling zone, located at higher distances from the cylinder deck, features similar values and characteristics between the two cases in the time instants inspected.

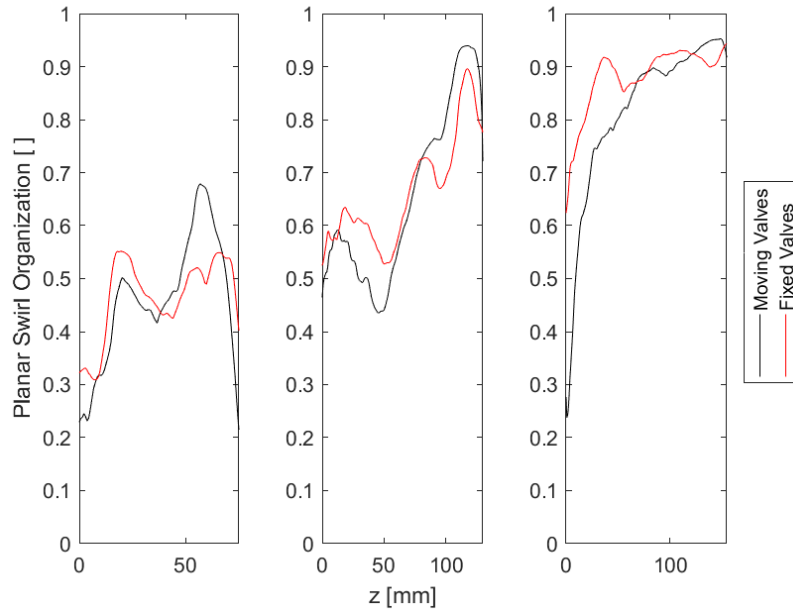


FIGURE 6.30. Planar Swirl Organization along the  $z$ -axis for the moving and the fixed valves case at 0.5, 0.75 and 1 s after the beginning of the intake stroke (left-to-right).

In conclusion, the overall swirl behaviour is characterized by an increasing organization and a decreasing intensity through the second part of the stroke. Despite some differences between the moving and fixed valves case, the decreasing azimuthal component in the lower zones of the cylinder affects the strength of the swirling motion, making the Planar Swirl Number distribution along the cylinder axis flatter and less intense. On the other hand, the swirl pattern tends to be more stable, reaching higher organization values and developing larger organized zones throughout the stroke.

### 6.5. Comparison of PIV measurements with RANS results

RANS CFD simulations of the intake stroke in the experimental setup used for the SPIV measurement campaign were carried out at SCANIA CV AB by M. Söder with the purpose of comparing the outcomes and assessing the reliability of the numerical method. Only the realistic, moving valves case was numerically inspected. Some differences with the experimental conditions had to be introduced in the numerical simulations in order to avoid issues related to the incompressibility of the working fluid. Furthermore, the piston motion

was modeled with some discrepancies with the actual motion (Fig. 6.31), again for simulation purposes.

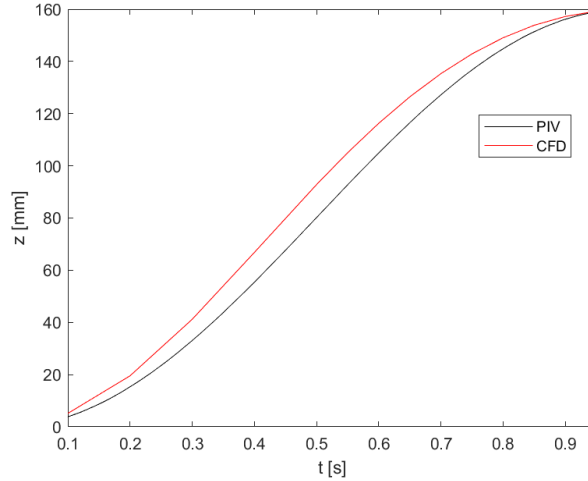


FIGURE 6.31. Piston motion profile used in the experimental PIV measurements and in the CFD simulations.

The comparison of the velocity fields obtained by means of experimental and numerical approach in the time range between 0.1 and 0.95 s from the beginning of the intake stroke is presented in the next subsections. To carry out a quantitative analysis, some of the evaluation tools introduced in the previous chapters were used. For planar and three-dimensional data, the frames of references described in subsections 5.2.2 and 5.3.2 are used respectively.

### 6.5.1. Planar velocity fields

The two-dimensional, two-component averaged velocity fields in the  $0^\circ$  and  $90^\circ$  planes (see Fig 5.5) were firstly compared to gain insight into the accuracy of the numerical method in predicting the distribution of the vertical and the radial velocity component. The time evolution of the planar fields was inspected, with the focus on the second part of the stroke, in order to investigate the development of similar large-scale flow structures in the two cases.

The data obtained in the  $0^\circ$  plane, plotted at three different time instants throughout the stroke in Fig. 6.32, show an overall good agreement between the numerical and the experimental approach. The CFD method catches the dynamics of the large scales in the flow, predicting with good accuracy the range of velocity values in the cylinder, as well as the evolution of the jet pattern and the development of the recirculation zone. The agreement between the two methods is particularly precise at the end of the stroke, when the RANS data

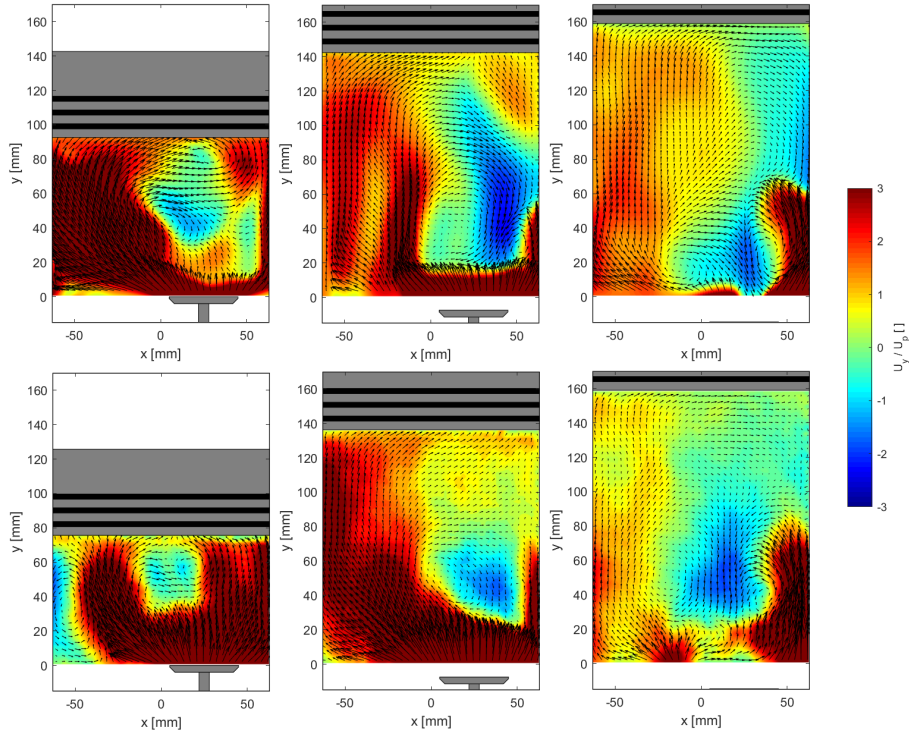


FIGURE 6.32. Comparison of RANS data (top row) with SPIV measurements (bottom row) in the  $0^\circ$  plane at 0.5, 0.75 and 0.95 s from the beginning of the intake stroke (left-to-right). One of every four vector is plotted for PIV data, whereas CFD results were interpolated to fit the same equispaced grid. The azimuthal velocity normalized by the mean piston speed is colour-coded and vectors length is scaled with respect to the highest-magnitude vector for each field.

match the most common flow behaviour present within the ensemble of cycles measured by means of PIV (Fig. 6.11). In fact, as explained in subsection 6.2.1, major cyclic variations resulting in two possible flow patterns were found in this plane. The removal of the less common one from the global average therefore finds a further validation in the comparison with the RANS results.

Fig. 6.33 shows instead the time evolution of the velocity fields obtained by means of PIV and RANS in the  $90^\circ$  plane. The dynamics of the flow, dominated by the development of a quasi-symmetric jet structure characterized by oscillations and two recirculation zones above the valves, is well predicted by RANS simulations during the first half of the stroke. Again, the values of the

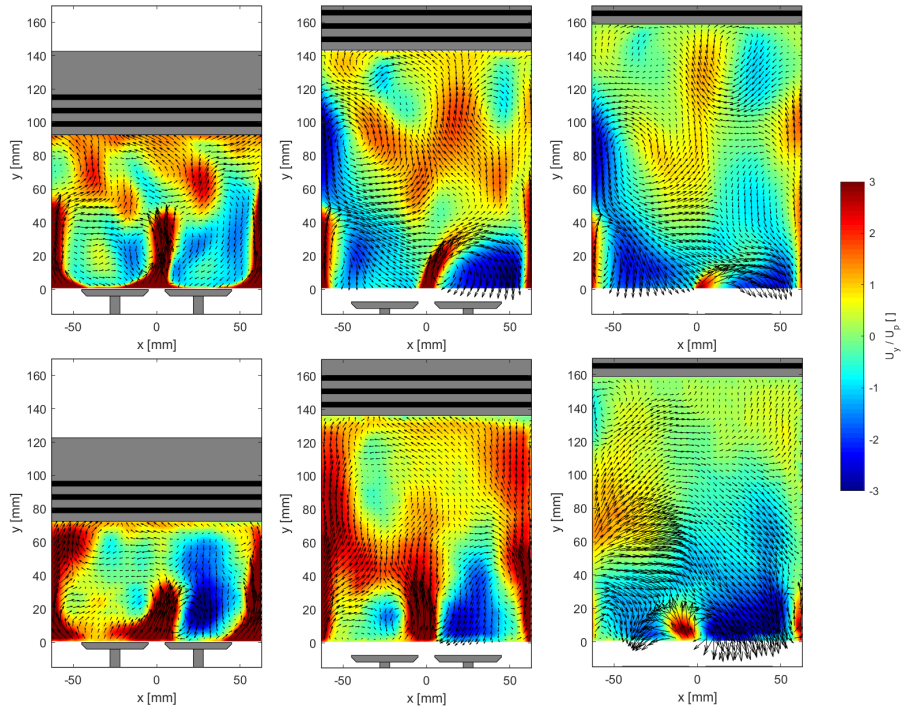


FIGURE 6.33. Comparison of RANS data (top row) with SPIV measurements (bottom row) in the  $90^\circ$  plane at 0.5, 0.75 and 0.95 s from the beginning of the intake stroke (left-to-right). One of every four vector is plotted for PIV data, whereas CFD results were interpolated to fit the same equispaced grid. The azimuthal velocity normalized by the mean piston speed is colour-coded and vectors length is scaled with respect to the highest-magnitude vector for each field.

velocity magnitude are generally matched in all the cylinder volume. However, the agreement between RANS and PIV gets worse after mid-intake, and the numerical method fails to describe accurately the evolution of the flow pattern, especially in the left side of the field. In fact, comparing to PIV data, RANS simulations underestimate the intensity of the jet close to the cylinder walls in the second part of the stroke, showing instead a larger recirculation zone.

In conclusion, a qualitatively good agreement was found between PIV and RANS CFD data in the evolution of two-dimensional, two-component velocity fields during the intake in the planes inspected. Such a result is a proof of the reasonable accuracy of the averaged numerical approach in predicting the behaviour of the radial and vertical component of the mean velocity field. These

components, in fact, are strongly affected by geometrical constraints, *i.e.* the piston and the cylinder, which decrease significantly the degrees of freedom of the flow in these two directions.

### 6.5.2. Three-dimensional velocity fields

The three-dimensional averaged velocity fields reconstructed from PIV-measured planar data were then compared to the RANS results. As discussed in 6.3.1, in PIV measurements the mean flow is characterized by a large azimuthal component, which results in the development of a strong and organized swirling motion during the second half of the stroke. Similarly, in RANS data the three-dimensional velocity fields present a swirling pattern in the horizontal planes. Such motion tends to get increasingly organized throughout the stroke. However, the magnitude of the azimuthal component predicted by RANS simulations is significantly lower than in PIV data, and the flow patterns in the lower horizontal planes appear to be smoother and more regular in the numerical results, as can be seen in Fig. 6.34.

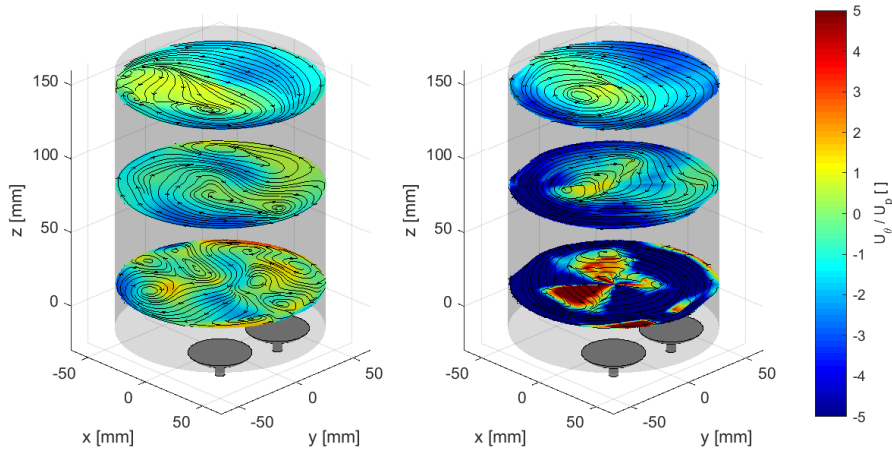


FIGURE 6.34. Comparison of three-dimensional reconstructed velocity fields from RANS data (left) and SPIV measurements (right) at the end of the stroke ( $t = 0.95$  s). In-plane velocity is represented by the streamlines, whereas the azimuthal velocity normalized by the mean piston speed is colour-coded. Three equispaced horizontal planes are shown for each field.

These differences in the azimuthal component of the three-dimensional velocity fields derive from the disparities observed in the distribution of the out-of-plane velocity component in vertical planes. As an example, Fig. 6.35 shows the out-of-plane velocity field in the  $0^\circ$  plane at the end of the stroke inspected

by means of RANS and SPIV, which employs the stereoscopic principle to measure such velocity component.

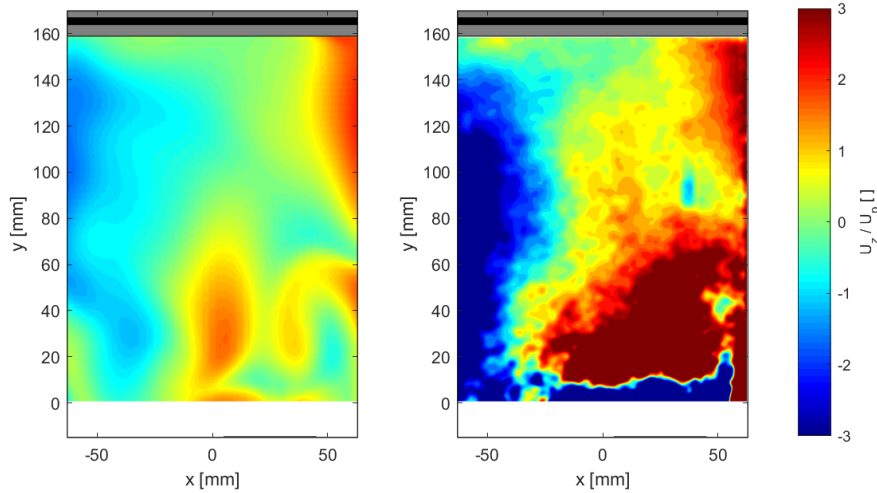


FIGURE 6.35. Comparison of the out-of-plane component from RANS data (left) and SPIV measurements (right) in the  $90^\circ$  plane at the end of the stroke ( $t = 0.95$  s). The out-of-plane velocity normalized by the mean piston speed is colour-coded.

While the overall pattern of the velocity distribution is decently predicted by the numerical simulation, big discrepancies between the two methods are present in the magnitude of the out-of-plane component, especially close to the cylinder deck. By comparing such component with the planar velocity distribution at the same time instant (right column of Fig. 6.32), it can be seen how in RANS results the out-of-plane component is generally lower than the planar velocity. In PIV measurements, instead, the out-of-plane component is the dominant one. These differences in the velocity components result in noticeable differences in mean flow within the cylinder volume. First of all, the intensity of the three-dimensional swirling motion around the cylinder axis is significantly lower in CFD results. Secondly, due to the aforementioned ratio between the azimuthal and the vertical-radial component, the three-dimensional flow pattern present different main features in the two cases. To better visualize such differences, Fig. 6.36 shows the three-dimensional streamlines at the end of the stroke in the two cases.

The prevalence of the radial-vertical motion in the RANS data results in the tumbling motion being stronger than the swirling one. The streamlines highlight in fact a developed tumble which overcomes the swirl given by the azimuthal component. In PIV data, instead, the overall flow pattern described

by the streamlines is characterized by swirl, with the vertical and radial component not influencing markedly the solid body-like rotation around the cylinder axis. The effect provoked by these components can be simplified as a slight tilting of the swirl rotation axis. Furthermore, the comparison of the streamlines underlines the already mentioned difference in the regularity and smoothness of the flow field, especially close to the valves, with the PIV-measured flow appearing irregular when compared to the RANS outcomes.

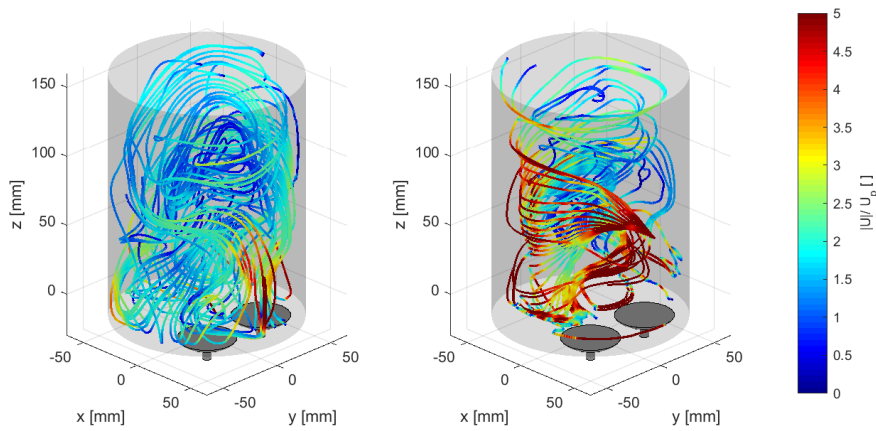


FIGURE 6.36. Three-dimensional reconstructed velocity fields at the end of the stroke ( $t = 0.95$  s) for the CFD (left) and PIV (right) data. Streamlines represent the three-component, three-dimensional velocity fields and are colour-coded by the velocity magnitude normalized by the mean piston speed.

Differently from planar data, the agreement between PIV and RANS results is poor for what concerns the three-dimensional swirling motion generated by the intake port. The RANS method seems to be significantly less accurate in predicting the rotating motion of the flow around the cylinder axis, which involves major difficulties and less geometrical constraints. This might be due to the simplifications and the limitations features in this averaged approach to the solution of the Navier-Stokes equations, which is often ineffective for simulations of rotating flows.

### 6.5.3. Swirl and tumble parameters

To quantify the differences between RANS and PIV data in the three-dimensional mean flow, it is useful to evaluate and compare the flow parameters defined in the previous chapters, such as the Swirl Number, the Tumble Number and the Planar Swirl Organization, and their evolution throughout the intake stroke.

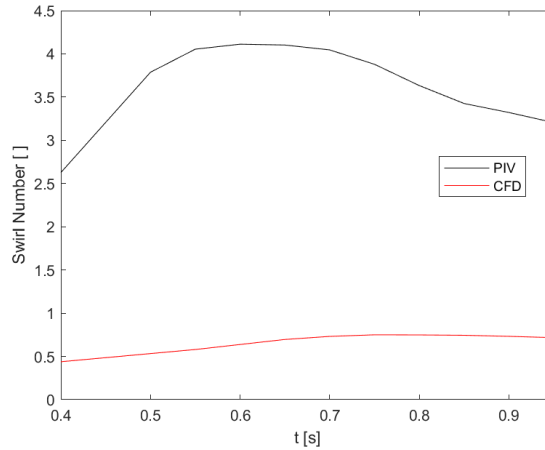


FIGURE 6.37. Evolution of the Swirl Number throughout the second part of the stroke. Note that the actual Swirl Number is negative since the flow rotates clockwise with respect to the  $z$ -axis, and thus the absolute value is taken for ease of visualization.

Fig. 6.37 shows the evolution of the Swirl Number in the two cases considered during the second half of the stroke. As expected from the overview of the three-dimensional flow, RANS CFD underestimates the azimuthal velocity, and thus the swirl intensity, in comparison with the PIV measurements. The Swirl Number at the end of the stroke, for example, is around four times higher in the velocity field measured by means of PIV.

On the other hand, RANS simulations turned out to be more accurate in predicting the organization of the planar swirl pattern along the cylinder axis. As can be seen in Fig. 6.38, the same kind of trend is present in both CFD and PIV data in the development of an organized swirling motion. Whereas at mid-intake the flow is still characterized by irregularities in the swirl pattern at each height along the cylinder axis, towards the end of the stroke the swirl motion gets more organized, especially in the higher zones of the cylinder (Fig. 6.39). However, the flow field computed by means of CFD feature significantly lower organization values close to the cylinder deck at the very end of the stroke (Fig. 6.40), as well as a smaller highly-organized zone close to the piston. These features, along with the differences in the azimuthal component, whose magnitude profile is rather constant with height in CFD data (Fig. 6.34), contribute to increase the difference in the three-dimensional swirl number at the end of the intake.

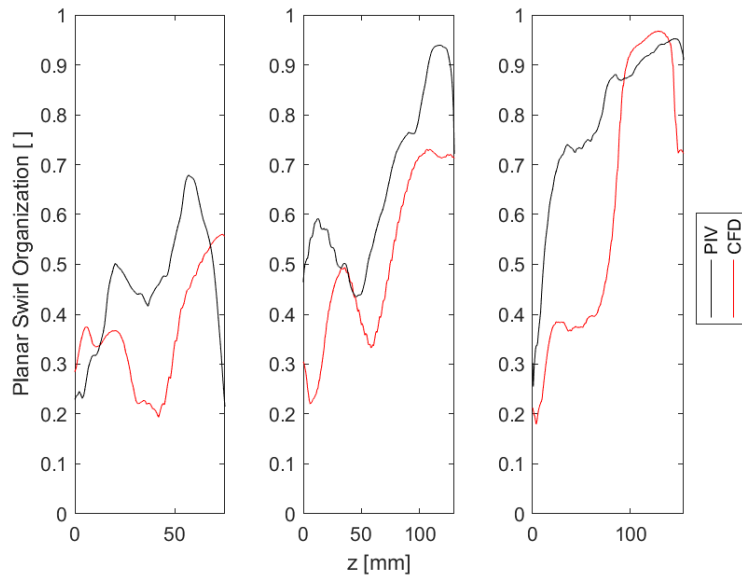


FIGURE 6.38. Planar Swirl Organization along the  $z$ -axis for the CFD and PIV velocity fields at 0.5, 0.75 and 0.95s after the beginning of the intake stroke (left-to-right).

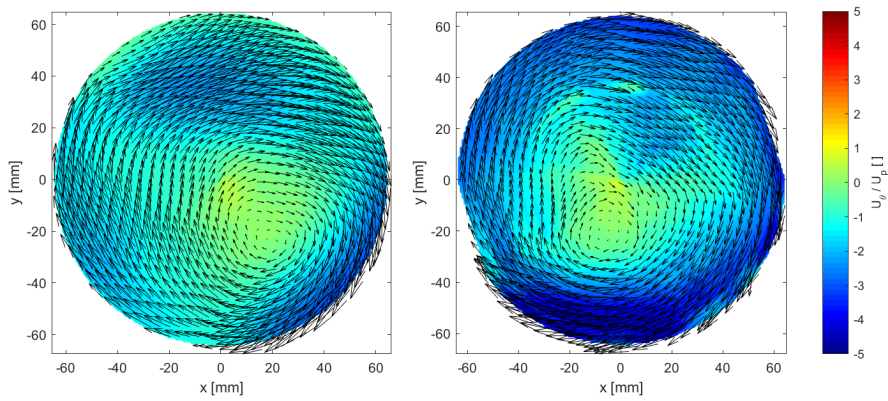


FIGURE 6.39. Swirl pattern in a horizontal plane 130 mm away from the cylinder deck at the end of the stroke ( $t = 0.95$  s). CFD data (left) present the same swirl organization and a slightly lower intensity when compared to PIV data (right).

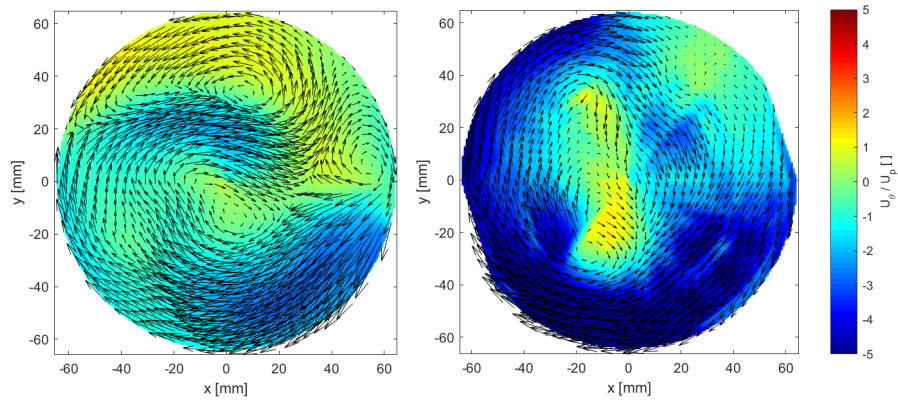


FIGURE 6.40. Swirl pattern in a horizontal plane 75 mm away from the cylinder deck at the end of the stroke ( $t = 0.95$  s). CFD data (left) present lower swirl organization and intensity when compared to PIV data (right).

Finally, a comparison of the Tumble Number is shown in Fig. 6.41. Again, the agreement between the two sets of data is poor even though the RANS velocity fields in the two vertical planes inspected in subsection 6.5.1 match well the experimental data. In fact, the Tumble Number accounts also for the profile of the azimuthal velocity along the cylinder axis, and it is thus affected by the large differences found in the distribution of such velocity component.

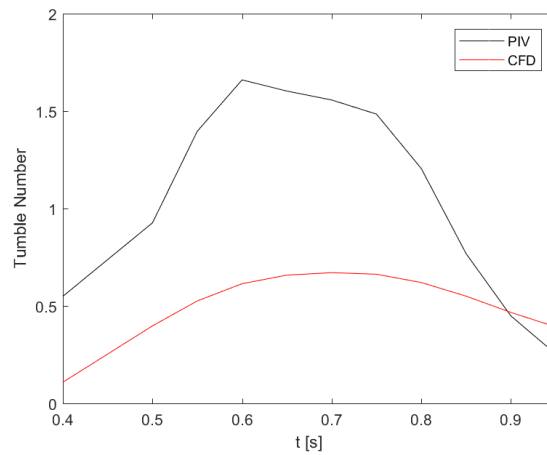


FIGURE 6.41. Evolution of the Tumble Number throughout the second part of the stroke.



## Conclusion and future work

### 7.1. Summary

An experimental database of velocity fields obtained by means of Time-Resolved Stereoscopic PIV has been inspected and analyzed to investigate the fluid dynamics of the intake flow in a water-analogue engine model of the size of a typical heavy-duty Diesel engine. The three-dimensional averaged flow has been reconstructed from two-dimensional, three-component velocity fields measured in different planes by rotating the engine setup. Two different cases, one with fixed and one with moving valves, have been evaluated to assess the performance of the inlet port and eventually a comparison with RANS CFD results has been carried out.

The main features of the intake flow, such as development of a tumbling and a strong swirling motion, have been observed and quantified. The influence of the valves motion on swirl has been proved to be negligible, whereas it affects significantly the evolution of the tumbling motion and its structure at the end of the intake. Phase-invariant POD has been proved to be a useful tool for the detection of cycle-to-cycle variations in high-energy, large-scale flow structures. A good agreement between RANS CFD simulations and PIV measurements has been found for the two-dimensional velocity fields obtained in vertical planes. Generally, the RANS method well predicted the main features of the flow, such as the structure of the intake jet, the development of recirculation bubbles and the rise of the tumbling motion. However, big differences have been found in the magnitude of the azimuthal component and therefore in the swirl intensity, especially close to the cylinder deck, where the high velocities and the chaotic flow pattern present in PIV measurement are not matched by the smooth and regular RANS-predicted velocity fields.

### 7.2. Outlook on future work

Although the approach used for this study allows for a complete three-dimensional and time-resolved inspection of the intake mean flow, future work may focus and deeply inspect some of the main aspects highlighted. As an example, horizontal plane PIV measurements could be performed in a similar setup to study the instantaneous and the averaged swirl motion generated by the inlet port at different time instants during the intake stroke. However, the design of

such a piston-cylinder setup and its integration with the PIV system would be challenging from a technical point of view.

Furthermore, it would be interesting to inspect directly the three-dimensional flow, in order to obtain instantaneous three-dimensional velocity fields. An analysis of such data could reveal interesting information about the instantaneous behaviour of large-scale structures, the development of turbulence and the generation of cyclic variations. However, the experimental methods that allow for full three-dimensional and instantaneous measurements are going through an early phase of their development, and the first works published aim to prove their reliability and the agreement with traditional PIV system.

In conclusion, a deeper inspection of the unstable behaviour of the inlet port-generated flow could be useful to understand the causes and the mechanism behind the generation of the fluctuations featured by the flow in planar data. As an example, a scenario where small perturbations in the inlet conditions are introduced on purpose to evaluate the effect on the most energetic structures of the flow might be worth investigating.



## APPENDIX A

### SPIV validation using the continuity equation

The fulfillment of the continuity equation for the SPIV data was verified in order to validate the measurements. For an incompressible flow, the continuity equation can be expressed as follows:

$$\frac{\partial u_i}{\partial x_i} = 0 \quad (\text{A.1})$$

where  $u_i$  is the velocity vector. For PIV measurements it is helpful to consider the ensemble averaged velocity fields. By applying the Reynolds decomposition and averaging Eq. A.1, the continuity equation for the averaged velocity field can be written as:

$$\frac{\partial U_i}{\partial x_i} = 0 \quad (\text{A.2})$$

where  $U_i$  is the ensemble averaged velocity vector. For our purposes it is useful to consider a cylindrical frame of reference, whose vertical axis coincides with the cylinder axis. In this new reference frame the continuity equation can be expressed as:

$$\frac{1}{r} \frac{\partial(rV_r)}{\partial r} + \frac{1}{r} \frac{\partial V_\theta}{\partial \theta} + \frac{\partial V_z}{\partial z} = 0 \quad (\text{A.3})$$

where  $V_r$ ,  $V_\theta$  and  $V_z$  are the radial, the azimuthal and the vertical component of the averaged velocity field respectively. If we express the ratio between the azimuthal term and the two remaining terms as:

$$\left( \frac{1}{r} \frac{\partial v_\theta}{\partial \theta} \right) \Bigg/ \left( \frac{1}{r} \frac{\partial(rv_r)}{\partial r} + \frac{\partial v_z}{\partial z} \right) \quad (\text{A.4})$$

an evaluation of this quantity can be used to validate the SPIV measurements, and to find out possible overestimation of the azimuthal component. Stereoscopic PIV, in fact, measures this component differently from the two planar ones, and some difficulty may arise due to the increased complexity. For the continuity equation to be fulfilled, the ratio in Eq. A.4 should be equal to -1. To compute this ratio from averaged planar SPIV data, MATLAB<sup>®</sup> was used. The first and third term from Eq. A.3 were computed from the data of a single plane using a central difference derivative scheme. To assess the second term, instead, three consecutive planes had to be taken into consideration, again employing a central difference derivative scheme.

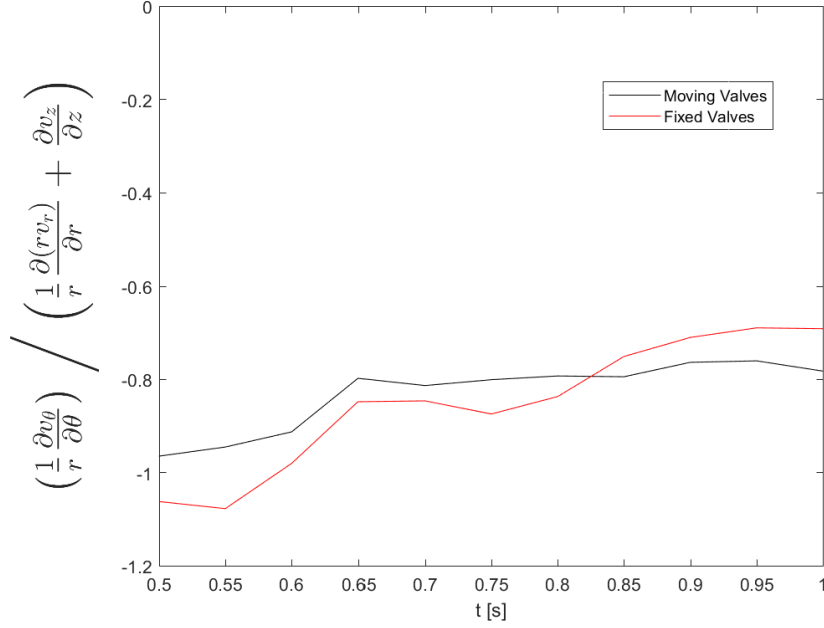


FIGURE A.1. Ratio of the azimuthal term and the two remaining terms of the averaged continuity equation, averaged over the planes measured at different time instants during the second part of the stroke. For both the moving and the fixed valves case, the  $0^\circ$  and the  $144^\circ$  plane were not considered due to the central difference scheme used to compute the azimuthal derivative.

Fig. A.1 shows the outcomes of this validation. As already mentioned, the ideal value of the consider ratio would be -1. However, experimental limitations such as measurement errors and general noise have to be taken into account when evaluating the actual value. In this sense, being most of the values in the range between -0.8 and -1.05, a good agreement with the predicted outcome is found, and this can be considered as a validation for the data measured by means of Stereoscopic PIV.



## References

- ACEA 2018 Truck industry reacts to EU proposal for first-ever CO2 standards. <http://www.acea.be/press-releases/article/truck-industry-reacts-to-eu-proposal-for-first-ever-co2-standards> [Online; accessed 24 May 2018].
- ÅGREN, C. 2009 File:Euro-IV-fig.gif. <http://www.airclim.org/sites/default/files/images/AcidNews/2009/AN1-09/Euro-IV-fig.gif> [Online; accessed 12 May 2018].
- ALGER, T., GALLANT, E., MCGEE, J. & WOOLDRIDGE, S. 2004 PIV In-Cylinder Flow Measurements of Swirl and the Effect of Combustion Chamber Design. *SAE Technical Paper Series 2004-01-1952*.
- BAKKER, A. 2006 Turbulence Models - Slides of the Applied Computational Fluid Dynamics course, Dartmouth College. <http://www.bakker.org/dartmouth06/engs150/10-rans.pdf> [Online; accessed 25 June 2018].
- BAUM, E., PETERSON, B., BÖHM, B. & DREIZLER, A. 2014 On The Validation of LES Applied to Internal Combustion Engine Flows: Part 1: Comprehensive Experimental Database. *Flow Turbul. Combust.* **92**, 269–297.
- BAUMANN, M., DI MARE, F. & JANICKA, J. 2014 On the Validation of Large Eddy Simulation Applied to Internal Combustion Engine Flows Part II: Numerical Analysis. *Flow Turbul. Combust.* **92**, 299–317.
- BÜCKER, I., KARHOFF, D. C., KLAAS, M. & SCHRÖDER, W. 2012 Stereoscopic multi-planar PIV measurements of in-cylinder tumbling flow. *Exp. Fluids* **53**, 1993–2009.
- BORÉE, J., MAUREL, S. & BAZILE, R. 2002 Disruption of a compressed vortex. *Phys. Fluids* **14**, 2543–2556.
- BORÉE, J. & MILES, P. 2014 In-cylinder flow. In *Encyclopedia of automotive engineering* (ed. John Wiley & Sons Ltd.).
- BOTTONE, F., KRONENBURG, A., GOSMAN, D. & MARQUIS, A. 2012 Large Eddy Simulation of Diesel Engine In-cylinder Flow. *Flow Turbul. Combust.* **88**, 233–253.
- CELIK, I., YANUZ, I. & SMIRNOV, A. 2001 Large eddy simulations of in-cylinder turbulence for internal combustion engines: A review. *Int. J. Engine Res.* **2**, 119–148.

- CHATTERJEE, A. 2000 An introduction to the proper orthogonal decomposition. *Curr. Sci.* **78**, 808–817.
- CHEN, H., REUSS, D. L. & SICK, V. 2012 On the use and interpretation of proper orthogonal decomposition of in-cylinder engine flows. *Meas. Sci. Technol.* .
- COSADIA, I., BORÉE, J., CHARNAY, G. & DUMONT, P. 2006 Cyclic variations of the swirling flow in a Diesel transparent engine. *Exp. Fluids* **41**, 115–134.
- COSADIA, I., BORÉE, J. & DUMONT, P. 2007 Coupling time-resolved PIV flow-fields and phase-invariant proper orthogonal decomposition for the description of the parameters space in a transparent Diesel engine. *Exp. Fluids* **43**, 357–370.
- CRONHJORT, A. 2017 Combustion in Otto and Diesel engines - Slides of the Internal Combustion Engines course, KTH.
- CTR STANFORD 2004 Simulation of Turbulent Flows. <http://web.stanford.edu/class/me469b/handouts/turbulence.pdf> [Online; accessed 25 June 2018].
- DABIRI, D. 2006 Cross-Correlation Digital Particle Image Velocimetry - A Review. In *Turbulência* (ed. Freire). Associação Brasileira de Engenharia e Ciências Mecânicas (ABCM).
- DANNEMANN, J., PIELHOP, K., KLAAS, M. & SCHRÖDER, W. 2009 Cycle-Resolved Multi-Planar Particle-Image Velocimetry Measurements of the In-Cylinder Flow of a Four-Valve Combustion Engine. In *8th International Symposium on Particle Image Velocimetry - PIV09 Melbourne, Victoria, Australia, August 25-28, 2009*.
- DEMBINSKI, H. W. R. 2013 In-cylinder Flow Characterisation of Heavy Duty Diesel Engines Using Combustion Image Velocimetry. PhD thesis, KTH Royal Institute of Technology, Stockholm, Sweden.
- DRUAULT, P., GUIBERT, P. & ALIZON, F. 2005 Use of proper orthogonal decomposition for time interpolation from PIV data - Application to the cycle-to-cycle variation analysis of in-cylinder engine flows. *Exp. Fluids* **39**, 1009–1023.
- FOGLEMAN, M., LUMLEY, J. L., REMPFER, D. & HAWORTH, D. 2004 Application of the proper orthogonal decomposition to datasets of internal combustion engine flows. *J. Turbul.* **5**, 023.
- FREUDENHAMMER, D., PETERSON, B., DING, C. P., BOEHM, B. & GRUNDMANN, S. 2014 Volumetric intake flow measurements of an IC engine using magnetic resonance velocimetry. *Exp. Fluids* **55**, 1724–18.
- FUNK, C., DAHM, W. J. A., REUSS, D. L. & SICK, V. 2002 Turbulence Properties of High and Low Swirl In-Cylinder Flows. *SAE Technical Paper Series 2002-01-2841* .
- GRAFTIEAUX, L., MICHARD, M. & GROSJEAN, N. 2001 Combining PIV, POD and vortex identification algorithms for the study of unsteady turbulent swirling flows. *Meas. Sci. Technol.* **12**, 1422–1429.
- HESS, D., TAG, S. & BRÜCKER, C. 2012 Volumetric Flow Studies in a 4-stroke Water-Analogue IC-Engine Using High-Speed Scanning-PIV. In *16th International Symposium on Applications of Laser Techniques to Fluid Mechanics Lisbon, Portugal, 09-12 July, 2012*.
- HEYWOOD, J. B. 1987 Fluid motion within the cylinder of internal combustion engines-The 1986 Freeman scholar lecture. *J. Fluids Eng.* **109** (1), 3–35.
- HEYWOOD, J. B. 1988 *Internal combustion engines fundamental*. McGraw-Hill.

- HOLMES, P., LUMLEY, J. L. & BERKOOZ, G. 1996 Proper orthogonal decomposition. In *Turbulence, Coherent Structures, Dynamical Systems and Symmetry*. Cambridge University Press.
- JAYAKUMAR, C., NARGUNDE, J., SINHA, A., HENEIN, N. A., BRYZIK, W. & SATTLER, E. 2012 Effect of Swirl and Injection Pressure on Performance and Emissions of JP-8 Fueled High Speed Single Cylinder Diesel Engine. *J. Eng. Gas Turb. Power* **134**, 022802.
- JOHANSSON, A. V. & WALLIN, S. 2017 *An introduction to turbulence*, 4th edn. KTH Royal Institute of Technology.
- JOO, S. H., CHUN, K. M., SHIN, Y. & LEE, K. C. 2003 An investigation of flame expansion speed with a strong swirl motion using high-speed visualization. *J. Eng. Gas Turb. Power* **125**, 485–493.
- KALPAKLI VESTER, A. 2015 Assessment of the in-cylinder flow of internal combustion engines. *Tech. Rep.*. KTH Royal Institute of Technology.
- KALPAKLI VESTER, A., NISHIO, Y. & ALFREDSSON, P. H. 2018 Unravelling tumble and swirl in a unique water-analogue engine model. *J. Vis.* <https://doi.org/10.1007/s12650-018-0485-3> [Accepted].
- KANG, K. Y. & REITZ, R. D. 1999 The effect of intake valve alignment on swirl generation in a DI diesel engine. *Exp. Therm. Fluid Sci.* **20**, 94–103.
- KHALIGHI, B. 1991 Study of the intake tumble motion by flow visualization and particle tracking velocimetry. *Exp. Fluids* **10**, 230–236.
- KHALIGHI, B. & HUEBLER, M. S. 1988 A Transient Water Analog of a Dual-Intake-Valve Engine for Intake Flow Visualization and Full-Field Velocity Measurements. *SAE Transactions* **97**, 877–891.
- KOEHLER, M., HESS, D., & BRÜCKER, C. 2015 Flying PIV measurements in a 4-valve IC engine water analogue to characterize the near-wall flow evolution. *Meas. Sci. Technol.* **26**, 125302.
- KOEHLER, M., HESS, D., KRATZSCH, C. & BRÜCKER, C. 2014 Flying PIV measurements in a driven IC engine flow. In *17th International Symposium on Applications of Laser Techniques to Fluid Mechanics Lisbon, Portugal, 07-10 July, 2014*.
- KOLMOGOROV, A. N. 1941 The local structure of turbulence in incompressible viscous fluid for very large Reynolds numbers. *Dokl. Akad. Nauk SSSR* **30**, 301–305.
- KUMAR, R. 2016 4 stroke diesel engine working. <https://www.youtube.com/watch?v=DACGe2WNd3Q> [Online; accessed 24 June 2018].
- LAVISION GMBH 2015 FlowMaster. DaVis 8.3 product manual.
- LUMLEY, J. L. 1967 The Structure of Inhomogeneous Turbulent Flows. In *Atmospheric Turbulence and Radio Wave Propagation*. Nauka.
- MARZOUK, Y. M. & HART, D. P. 1998 Asymmetric autocorrelation function to resolve directional ambiguity in PIV images. *Exp. Fluids* **25**, 401–408.
- MEYER, K. E., CAVAR, D. & PEDERSEN, J. M. 2007 POD as tool for comparison of PIV and LES data. In *7th International Symposium on Particle Image Velocimetry Rome: Faculty of Engineering, University “La Sapienza”*.
- MOREAU, J., FOGLEMAN, M., CHARNAY, G. & BORÉE, J. 2005 Phase Invariant

- Proper Orthogonal Decomposition for the Study of a Compressed Vortex. *J. Therm. Sci.* **14**, 108–113.
- MORSE, A. P., WHITELAW, J. H. & YIANNESKIS, M. 1979 Turbulent flow measurements by laser-Doppler anemometry in motored piston-cylinder assemblies. *J. Fluids Eng.* **101**, 208–216.
- MULLIN, T. 1989 Turbulent times for fluids. *New Sci.* **124**, 52–55.
- MURALI KRISHNA, B. & MALLIKARJUNA, J. M. 2011 Effect of Engine Speed on In-Cylinder Tumble Flows in a Motored Internal Combustion Engine - An Experimental Investigation Using Particle Image Velocimetry. *J. Appl. Fluid Mech.* **4**, 1–14.
- NATIONAL RESEARCH COUNCIL 2008 Review of the 21st century truck partnership. *Tech. Rep.*. The National Academies Press.
- VAN OVERBRÜGGEN, T., BAHL, B., DIERKSHEIDE, U., KLAAS, M. & SCHRÖDER, W. 2013a Tomographic particle-image velocimetry in an IC engine. In *10th International Symposium on Particle Image Velocimetry - PIV13 Delft, The Netherlands, July 1-3, 2013*.
- VAN OVERBRÜGGEN, T., BÜCKER, I., DANNEMANN, J., KARHOFF, D. C., KLAAS, M. & SCHRÖDER, W. 2015 Planar, Stereoscopic, and Holographic PIV-Measurements of the In-Cylinder Flow of Combustion Engines. In *Fuels From Biomass: An Interdisciplinary Approach* (ed. Springer).
- VAN OVERBRÜGGEN, T., DANNEMANN, J., KLAAS, M. & SCHRÖDER, W. 2013b Holographic particle image velocimetry measurements in a four-valve combustion engine. *Exp. Fluids* **55**, 1634.
- PAYRI, F., DESANTES, J. M. & PASTOR, J. V. 1996 LDV measurements of the flow inside the combustion chamber of a 4-valve D.I. diesel engine with axisymmetric piston-bowls. *Exp. Fluids* **22**, 118–128.
- RABAULT, J., VERNET, J. A., LINDGREN, B. & ALFREDSSON, P. H. 2016 A study using PIV of the intake flow in a diesel engine cylinder. *Int. J. Heat Fluid Flow* **62**, 56–67.
- RAFFAEL, M., WILLERT, C. & KOMPENHANS, J. 1998 *Particle Image Velocimetry: A Practical Guide*. Springer.
- REUSS, D. L. 2000 Cyclic Variability of Large-Scale Turbulent Structures in Directed and Undirected IC Engine Flows. *SAE Technical Paper Series 2000-01-0246*.
- RÉGERT, T., RAMBAUD, P. & RIETHMULLER, M. L. 2005 Investigation of the link between physics and POD modes. In *Recent Developments in Non-Intrusive Measurement Technology for Military Application on Model- and Full-Scale Vehicles*, pp. 4:1–12.
- SCHMITT, M., FROUZAKIS, C. E., TOMBOULIDES, A. G., WRIGHT, Y. M. & K., B. 2014 Direct numerical simulation of multiple cycles in a valve/piston assembly. *Phys. Fluids* **26**, 035105.
- SÖDER, M., VERNET, J., LINDGREN, B. & FUCHS, L. 2012 A coupled PIV-LES Approach to Understand Port Generated Structures. In *LES4ICE Paris, France, November 29-30, 2012*.
- SICK, V. & FAJARDO, C. M. 2009 Kinetic Energy and Dissipation Rate Spectra of High- and Low-Swirl Internal Combustion Engine Flows. *SAE Technical Paper Series 2009-01-0651*.

- SINGH, A. P., AGARWAL, A. K. & GUPTA, A. 2015 Tomographic Particle Image Velocimetry for Flow Analysis in a Single Cylinder Optical Engine. *SAE Int. J. Mater. Manuf.* **8**, 472–481.
- SIROVICH, L. 1987 Turbulence and the dynamics of coherent structures. Part I: Coherent structures. *Quart. Appl. Math.* **45**, 561–571.
- VERNET, J. 2012 Detailed study of steady in-cylinder flow and turbulence using stereo-PIV. Master’s thesis, Scania CV, Södertälje and KTH Mechanics, Stockholm, Sweden.
- VOISINE, M., THOMAS, L., BORÉE, J. & REY, P. 2011 Spatio-temporal structure and cycle to cycle variations of an in-cylinder tumbling flow. *Exp. Fluids* **50**, 1393–1407.
- WESTERWEEL, J., ELSINGA, G. . E. & ADRIAN, R. J. 2012 Particle Image Velocimetry for Complex and Turbulent Flows. *Annu. Rev. Fluid Mech.* **45**, 409–436.
- WIKIMEDIA COMMONS 2015 File:DieselCycle PV.svg — Wikimedia Commons, the free media repository. [https://commons.wikimedia.org/w/index.php?title=File:DieselCycle\\_PV.svg&oldid=162708381](https://commons.wikimedia.org/w/index.php?title=File:DieselCycle_PV.svg&oldid=162708381) [Online; accessed 22 May 2018].
- YU, R., BAI, X. S., L., H., HULTQVIST, A. & MILES, P. 2006 Numerical and Experimental Investigation of Turbulent Flows in a Diesel Engine. *SAE Technical Paper Series 2006-01-3436* .
- ZENTGRAF, F., BAUM, E., BÖHM, B., DREIZLER, A. & PETERSON, B. 2016 On the turbulent flow in piston engines: Coupling of statistical theory quantities and instantaneous turbulence. *Phys. Fluids* **28**, 045108.
- ZHA, K., BUSCH, S., MILES, P. C., MITRA, S., SENEAL, P. K. & WIJEYAKULASURIYA, S. 2015 Characterization of Flow Asymmetry During the Compression Stroke Using Swirl-Plane PIV in a Light-Duty Optical Diesel Engine with the Re-entrant Piston Bowl Geometry. *SAE Int. J. Engines* **8**, 1837–1855.



I hereby declare that I have written this thesis without any help from others and without the use of documents and aids other than those stated above. All sentences or passages quoted in this thesis from other people's work have been specifically acknowledged by clear cross-referencing to author, work and page(s). Any illustrations which are not the work of the author have been used with the explicit permission of the originator and are specifically acknowledged.

I understand that failure to specifically acknowledge all used work amounts to plagiarism and will have judicial and disciplinary consequences leading to the derecognition of the degree awarded on the basis of this thesis.

With my signature I declare the accuracy of these specifications.

---

Place, Date

---

Signature